

# Experimental and Numerical Investigation of Rotating Rayleigh Bénard Convection

*A thesis submitted in partial fulfillment  
of the requirements for the degree of  
Master of Science (by Research)*



*by*  
**Abhilash Ojha**

18105402

*under the guidance of*  
**Dr. Pranav Joshi**

*to*  
Department of Mechanical Engineering  
**Indian Institute of Technology, Kanpur**  
Uttar Pradesh, India  
November, 2021

# Certificate

---

It is certified that the work contained in this thesis entitled "**Experimental and Numerical Investigation of Rotating Rayleigh Bénard Convection**", by Mr. Abhilash Ojha (Roll No. 18105402), has been carried out under my supervision and that this work has not been submitted elsewhere for a degree.



**Dr. Pranav Joshi**

Assistant Professor

Department of Mechanical Engineering

Indian Institute of Technology Kanpur

*November, 2021*

# Declaration

---

It is certified that the work contained in this report entitled “**Experimental and Numerical Investigation of Rotating Rayleigh Bénard Convection**” has been authored by me. The work has been carried out under the supervision of **Dr. Pranav Joshi**.

To the best of my knowledge, this is an original work, both in terms of research content and narrative, and it has not been submitted anywhere else, in part or full, for a degree. In keeping with the general practice of reporting scientific observations, due acknowledgment and appropriate citations have been made wherever the work derived is based on the findings of other sources.



**Abhilash Ojha**

18105402, M.S (by Research).

Department of Mechanical Engineering

Indian Institute of Technology Kanpur

*November, 2021*

## Acknowledgments

---

This thesis is the final step of a three years journey of joy. Before closing the final step, I would like to thank the people who helped me in this journey and contributed to this thesis. Without the help of these people, this thesis would not have been possible.

First and foremost, I would like to thank my advisor Dr. Pranav Joshi who gave me the opportunity to work on this exciting project. I have been extremely fortunate to have an advisor who was always available for discussion; whenever I had questions, I could discuss them with you, and our discussions were always illuminating. I would also like to thank you for your encouragement and support during these three years. I would also like to thank Dr. Avishek Ranjan for his guidance in the numerical part of the thesis. I still remember the day when I first met you in IIT-Bombay; you guided me when I was making my decision to pursue master's at IIT-K. It was an interesting coincidence that I got the chance to work with you. I would also like to thank Prof. M.K. Verma for guiding me in the numerical part of my thesis. Your curiosity to learn new skills and apply them without fear of failure has always inspired me.

I would like to thank my labmates: Mohammad Anas, for the insightful discussion in the numerical part of this thesis. Thank you, Anas, for familiarizing me with numerical simulations and fostering my interest in learning CUDA. Thank you, Vinay Tripathi, for helping me out with the experimental setup; thanks for your company to mechanical workshops. Thank you, Bipin and Praveen for all those badminton and squash matches in the evening, you guys made work fun. Thank you, guys!. I would like to thank Sunil Saw (SAC-ISRO), Mamta Chauhan (SAC-ISRO) for helping me out with the design of the experimental setup. I would like to thank other friends and colleagues in the Northern laboratories building: Harsimran Singh, Gagandeep Singh, Lt. Col Vinay Sharma, Shashi, Manish Raj, Mayank Patel.

I would like to thank the central workshop and 4i lab people, Mr. Anil Jha, Mr. Virendra Singh, and Mr. Manoj Sharma (Senior Technician) of the fluid mechanics laboratory. Thank you all for your valuable inputs and help in designing and fabricating the rotating table facility. The fabrication of the Rayleigh Bénard cell would not have been possible without

the support of vendors, Mr. Prakash Panchal (Dhaval Electomech), Late Mr. Manoj, Mr. Ashok Bhuyan (ATIRA-Ahmedabad); thank you all for coming out of the way to help us.

Lastly, I would like to thank IITK for giving me the opportunity to pursue my master's. I didn't know beforehand that these three years would be one of the most beautiful years of my life. I got a chance to explore myself both academically, and non-academically and everything was beyond my expectation. The memories I made here will always last with me. No matter how much gratitude I pay to IIT-K (my alma mater), it will always be less.

## Synopsis

---

Buoyancy-driven flows play an important role in many natural phenomena and technological applications. Rayleigh-Bénard convection (RBC) is the representative system to study buoyancy-driven flows. In classical RBC, the flow is driven by the temperature difference between the heated bottom plate and a parallel cooled plate placed above it. The addition of rotation to RBC provides an interplay between buoyancy and rotation. Buoyancy-driven flows affected by background rotation are commonly found in geophysical and astrophysical phenomena. Rotating Rayleigh-Bénard convection (RBC) makes it possible to study these phenomena as it is mathematically well defined and experimentally accessible. Most of the surfaces encountered in nature and technological applications are inherently rough. Thus it is essential to understand the effect of surface roughness on the flow. Earlier studies on RBC have studied the effect of roughness and rotation separately. However, the combined effect of rotation and roughness has not been given much attention. The focus of the present study is to bridge this gap in our understanding by studying the effect of roughness on rotating RBC. The first part of this thesis describes the developed rotating table facility along with the RBC experimental setup. Our control and data acquisition system maintains the temperature of the bottom and top plates of the RBC cell within  $0.1^{\circ}\text{C}$ . Preliminary experiments on non-rotating RBC, with top and bottom rough walls, have been performed with water as the working fluid.

Helicity plays an important role in the generation of the magnetic field in planets, stars, etc. Spatial segregation of helicity is observed in most numerical dynamo simulations and is an important part of some proposed models on the generation of a dipolar magnetic field. Helicity in most geodynamo simulations has a distinct distribution above and below the equator – it is negative in the north and positive in the south. However, the mechanism behind the helicity segregation in these simulations remains unclear. Using direct numerical simulations of rotating Rayleigh-Bénard convection (RBC), with rotation axis perpendicular to gravity, we investigate the role of Ekman pumping as a possible mechanism behind helicity segregation in a Cartesian box. For a fixed Rayleigh number  $Ra = 10^5$  and Prandtl number

$Pr = 1$ , we consider two values of Taylor number,  $Ta = 10^5$  and  $10^6$ , and two boundary conditions – no-slip and constant stress (on the walls perpendicular to the rotation axis). We observe cyclonic flow in the bulk and helical flow driven by Ekman pumping near the boundaries normal to the rotation axis. This leads to helicity being negative (positive) near the wall with outward normal parallel (anti-parallel) to the rotation vector. The peak in the plane-averaged helicity occurs inside the Ekman layer in all simulations. The helicity magnitude is smaller for the constant stress boundary condition as compared to the no-slip boundary condition. We also observe that the buoyancy causes the high helicity regions inside Ekman boundary layer to migrate away from the rotation axis. Moreover, we also study the dominant flow structures in the flow by using modal energy analysis. We find that the mode (2,2), which represents the secondary rolls associated with Ekman pumping, contributes significantly to the total energy in planes parallel to the rotation vector.

Prior studies have focused on helicity segregation on a global scale in spherical geometry with rotation vector aligned with gravity. This is the first numerical demonstration of helicity segregation by Ekman pumping in the simple Cartesian box with gravity perpendicular to the rotation axis, that simulates the geometry of the equatorial regions. Our simulation results suggest that helicity segregation in dynamo simulations at large  $Ta$  but small  $Ra/Ra_{critical}$  arises due to Ekman pumping.

# Contents

<b>Acknowledgements</b>	<b>iv</b>
<b>List of Figures</b>	<b>xiv</b>
<b>List of Tables</b>	<b>xv</b>
<b>1 Introduction</b>	<b>1</b>
1.1 Equations of motion . . . . .	3
1.2 Coherent structures in the RBC . . . . .	4
1.3 Effect of roughness on non-rotating RBC . . . . .	6
1.4 Scaling law . . . . .	7
1.5 Boundary layer dynamics in smooth and rough RBC . . . . .	8
1.6 Rotating RBC with smooth walls . . . . .	9
1.6.1 Flow phenomenology . . . . .	9
1.6.2 Effect of flow parameters on RBC . . . . .	14
1.7 Rotating Rayleigh Bénard Convection with roughness . . . . .	16
<b>2 Experimental setup and measurements</b>	<b>18</b>
2.1 Experimental setup . . . . .	18
2.1.1 RBC cell . . . . .	18
2.1.2 Rotating table facility . . . . .	23
2.1.3 Motor assembly . . . . .	27
2.2 Data acquisition, thermometry and control system . . . . .	28

2.2.1	PID . . . . .	30
2.3	Nusselt number measurements . . . . .	31
<b>3</b>	<b>Numerical study on rotating convection with rotation vector perpendicular to gravity</b>	<b>35</b>
3.1	Introduction . . . . .	35
3.2	Simulation Details . . . . .	38
3.3	Results and Discussions . . . . .	40
3.3.1	Plane averaged helicity . . . . .	41
3.3.2	Helicity at different planes . . . . .	43
3.3.3	Modal energy analysis . . . . .	49
3.3.4	Force balance and helicity budget . . . . .	51
3.4	Discussion and Conclusions . . . . .	54
<b>4</b>	<b>Conclusions</b>	<b>57</b>
<b>A</b>	<b>CAD drawings</b>	<b>59</b>
<b>B</b>	<b>Numerical simulations</b>	<b>103</b>
B.1	Free Slip Boundary Condition . . . . .	103
B.2	Grid Independence . . . . .	103
<b>References</b>		<b>103</b>
<b>Publications</b>		<b>115</b>

# List of Figures

1.1	( <i>a,b</i> ) showing image of Jupiter's polar cyclones arranged in stable polygon pattern. (Credit: nasa.gov) . . . . .	2
1.2	Showing a propogating perturbation wave along boundary layer from experiments [1] at $Ra = 1.2 \times 10^9$ . Cold fluid is red, hotter fluid is green and waves are visible as dark lines. . . . .	4
1.3	Flow visualization of coherent structures in non-rotating RBC from experiments of [1] at $Ra = 1.2 \times 10^9$ . ( <i>a,b</i> ) Spiraling swirls gliding along top boundary. The cold fluid of boundary layer is red, warmer fluid of bulk is green and blue. ( <i>c,d</i> ) Thermal plumes emitted from boundary layer. . . . .	5
1.4	Sketch of flow near rough surface[2] in classical RBC. . . . .	6
1.5	Variation of normalized Nusselt number ( <i>Nu</i> ) [3] with rotation rate (1/Ro) for $Ra = 2.73 \times 10^8$ , $Pr = 6.86$ and $\Gamma = 1$ . Experimental data is indicated by red dots and numerical data by open square. . . . .	10
1.6	<i>Ra-Ta</i> parameter space, line L1 is loci of maximum Nusselt number and L2 divides region between non-rotating convection and rotating convection [4]. .	11
1.7	Laboratory Visualisation of Various Regimes with water as working fluid at different Ekman number in 80cm High by 20cm wide tank heated at constant heat flux [5] . . . . .	13

1.8	Shows effect of Rayleigh and Prandtl number on rotating RBC with smooth walls. (a) Shows variation of normalized Nusselt number $Nu/Nu(Ro = \infty)$ with Rossby number ( $Ro$ ) for different Prandtl number ( $Pr$ )[6]. (b) Shows variation of normalized Nusselt number $Nu/Nu(Ro = \infty)$ with Rossby number for different Rayleigh numbers[7]. . . . .	15
1.9	Schematic showing disruption and re-establishment of Ekman pumping in rotating Rayleigh Bénard flow with rough boundaries. . . . .	16
1.10	Variation of $Nu/Nu(Ro = \infty)$ wth Rossby number for different roughness. (a) Compares behaviour of R2R2 ( $k = 1.5$ ), both walls rough; R2S, one rough and one smooth walls; with smooth wall case. (b) Compares behaviour of R8R8 ( $k = 8$ ), both walls rough; R8S, one rough and one smooth walls; with smooth wall case. [8]. . . . .	17
2.1	(a) Variation of the Ekman boundary layer thickness ( $\delta_e$ ) with Rossby number ( $Ro$ ). (b) Various regimes observed in rotating Rayleigh-Bénard convection, the given cyan dots shows our planned experimental parameters. . . . .	19
2.2	(a) Schematic of the RBC cell for PIV experiment: TCP, top cover plate; CM, cooling manifold; ABT, air bleed tube connected to overhead reservoir; ASW, acrylic sidewalls; TR, tie rods; CP, copper plate; TM, NTC thermistors holes; RTD, holes for Pt100 RTD; IS, hylam insulation; PH, primary heater; SH, secondary heater; AIS, aluminium insulation. (b) The fabricated RBC cell for the planned PIV experiments. . . . .	20
2.3	(a) Copper plate encased in hylam insulation and (b) spiral grooves of the top copper plate. . . . .	21
2.4	Schematic of Top copper plate . . . . .	23
2.5	Schematic of experimental apparatus for Rotating Rayleigh Benard convection with rough plates. . . . .	24
2.6	(a) Rotating table sub-assembly, (b) Spyder assembly that supports rotating table. . . . .	25
2.7	Housing and Shaft Assembly . . . . .	26

2.8	Torque Characteristics of step-servo and servo motors . Red line indicates 600W step-servo motor and blue line indicates 600W servo motors. . . . .	27
2.9	Sensors used in the experiments. (a) threaded RTD used in the top copper plate. (b) Bead-shaped NTC thermistor. . . . .	29
2.10	R-T curve for the sensors used in our experiments. (a) RTD (Pt100), (b) NTC thermistors. . . . .	30
2.11	Flowchart of PID controller designed on LabVIEW. . . . .	31
2.12	(a) RBC cell for Nusselt number measurements and (b) non-rotating experiment setup. . . . .	32
2.13	Figure showing variation of the temperature of the top and bottom copper plates with time. . . . .	32
2.14	Nusselt vs Rayleigh number graph for non-rotating convection with both walls rough and working fluid as water. . . . .	33
3.1	(a), (b) $\phi, t$ -averaged helicity calculated using the fluctuating components of velocity and vorticity from [9]. Note that Taylor number ( $Ta$ ) for S0 and S2 are $4 \times 10^{10}$ and $4 \times 10^{14}$ , respectively. (c) Rotated image of $\phi, t$ -averaged helicity from [10] along with a Cartesian box shown in yellow near the equator, as a motivation for our simulation domain. Images are used with the permission of the authors. . . . .	38
3.2	(a) Schematic diagram of the model for our simulations, (b) Location of various planes in the domain. . . . .	39
3.3	Three-dimensional velocity vector field (colored with temperature) for RC2 showing dominance of cyclonic flow structure. . . . .	41
3.4	Variation of the constituents of helicity normalized by the maximum possible helicity $ \mathbf{u}  \boldsymbol{\omega} $ and averaged in the $yz$ -plane ( $H_r$ ) with $x$ for (a) RC1, (b) RC2, (c) RH, and (d) RCS. Horizontal dot-dashed lines represent the Ekman boundary layer thickness $\delta_E \approx 2.284\sqrt{\nu/\Omega}$ [11]. . . . .	42

3.5	Contour plots of normalized (by their rms values) $V_x$ , $\omega_x$ , and $V_x\omega_x$ (from left to right) superimposed with velocity vectors in $yz$ -plane at $x = 0.05$ for RC1 (first row), RC2 (second row), RH (third row), RCS (fourth row). . . . .	45
3.6	Contour plots of normalized (by their rms values) $V_y$ , $\omega_y$ , and $V_y\omega_y$ (from left to right) superimposed with velocity vectors in $xz$ -plane at $y = 0.5$ for RC1 (first row), RC2 (second row), RH (third row), RCS (fourth row). . . . .	46
3.7	Contour plot of normalized (by their rms value) $\omega_y$ superimposed with velocity vectors in $xz$ -plane at $y = 0.5$ for the run (a) RC2 and (b) RH. Signature of Ekman pumping is evident. Note in this figure that the vertical axis is along $x$ and horizontal along $z$ . . . . .	47
3.8	Contour plots of normalized (by their rms values) $V_z$ , $\omega_z$ , and $V_z\omega_z$ (from left to right) superimposed with velocity vectors in $xy$ -plane at $z = 0.5$ for RC1 (first row), RC2 (second row), RH (third row), RCS (fourth row). . . . .	48
3.9	Force balance between pressure gradient (including temperature) and Coriolis forces in $yz$ -plane at $x = 0.5$ (first row) and $x = 0.05$ (second row) for RC2. Vectors represent the respective force directions whereas colors represent their magnitude. Direction of rotation is into the page. . . . .	52
3.10	Force balance between pressure gradient and Coriolis forces in $yz$ -plane at $x = 0.5$ (first row) and $x = 0.05$ (second row) for RH. Vectors represent the respective force directions whereas colors represent their magnitude. Direction of rotation is into the page. . . . .	53
3.11	Variation of the helicity flux and helicity source terms averaged in $yz$ -plane ( $H_s$ ) along the rotation axis ( $x$ -direction) for (a) RC1, and (b) RC2. Note that $-\nabla \cdot \mathbf{F}_\Omega$ and $-\nabla \cdot \mathbf{F}_{p\omega}$ terms represent the helicity flux due to Coriolis force and pressure-vorticity force respectively, whereas $h_T$ and $h_\nu$ terms represent the helicity generation due to buoyancy force and viscous force respectively. Dot-dashed lines represent the Ekman boundary layer thickness. . . . .	55

B.1	Variation of the constituents of helicity normalized by maximum possible helicity $ \mathbf{u}  \boldsymbol{\omega} $ and averaged in $yz$ -plane ( $H_r$ ) with $x$ for free-slip boundary conditions on the walls perpendicular to the rotation vector. . . . .	104
B.2	Contour plots of normalized (by their rms values) $V_x$ , $\omega_x$ , and $V_x\omega_x$ in $yz$ -plane at $x = 0.05$ (first row), $V_y$ , $\omega_y$ , and $V_y\omega_y$ in $xz$ -plane at $y = 0.5$ (second row), and $V_z$ , $\omega_z$ , and $V_z\omega_z$ in $xy$ -plane at $z = 0.5$ (third row) for free-slip BCs on walls perpendicular to the rotation vector ( $x$ direction). . . . .	105
B.3	Variation of the constituents of helicity normalized by maximum possible helicity $ \mathbf{u}  \boldsymbol{\omega} $ and averaged in $yz$ -plane ( $H_r$ ) with $x$ for (a) RC1, (b) RC2, (c) RH, and (d) RCS. Continuous and dot-dashed lines represent results with $N = 128$ and $N = 256$ , respectively. . . . .	106

# List of Tables

1.1	Scaling Law in classical RBC with and without roughness ( $k$ indicates height of pyramid roughness in mm). . . . .	7
1.2	Transition boundaries for regimes I, II and III in Rotating RBC. . . . .	12
2.1	Experimental results of non-rotating Nusselt number measurements (with both rough plates). . . . .	33
3.1	Simulation details: $N$ is the number of grid points in each direction and $Pr = 1$ for all the runs. For RCS, no-slip boundary conditions are imposed at all the walls except $x = 0$ and $x = 1$ . . . . .	40
3.2	Modal energy of dominating modes in $yz$ -plane at $x = 0.5$ for RC1, RC2, RH, and RCS. . . . .	49
3.3	Modal energy of dominating modes in $xz$ -plane at $y = 0.5$ for RC1, RC2, RH, and RCS. . . . .	50
3.4	Modal energy of dominating modes in $xy$ -plane at $z = 0.5$ for RC1, RC2, RH, and RCS. . . . .	50

# Chapter 1

## Introduction

Thermally driven turbulent flow has been initially studied independently by Henri Bénard and Lord Rayleigh more than a century ago. The term [Rayleigh-Bénard Convection \(RBC\)](#) comes from their pioneering work. The [RBC](#) is used to study pattern formation and stability theory. [RBC](#) is a representative system to study unstable stratification due to temperature difference,  $\Delta$  between a heated horizontal plate and a cooled plate above it. Its conceptual beauty attracts theoretical and experimental physicists. On the one hand, it is mathematically well defined, through the Navier Stokes equation with appropriate boundary conditions. On the other hand, it is experimentally accessible.

In this thesis, we study classical [RBC](#) subjected to rotation along its vertical axis. Buoyancy-driven flows subjected to background rotation are an active agent in geophysical, astrophysical flow, and technological applications. Thermal convection is ubiquitous in nature. Large-scale flows affected by rotation in the earth's atmosphere and oceans owe their genesis to temperature-induced buoyancy. The combined effect of rotation and buoyancy lead to the formation of Hadley cells in the atmosphere. The winds generated by these are called trade winds. In addition to the earth's atmosphere, flows inside the earth's outer core (mantle convection) are driven by buoyancy and rotation.

Similar to the earth's atmosphere, zonal flows are also found in the atmosphere of other planets. The combined effect of rotation and buoyancy leads to pattern formation in planetary atmospheres. Fig. [1.1](#) shows Jupiter's polar cyclones hanging together. Due to the effect of

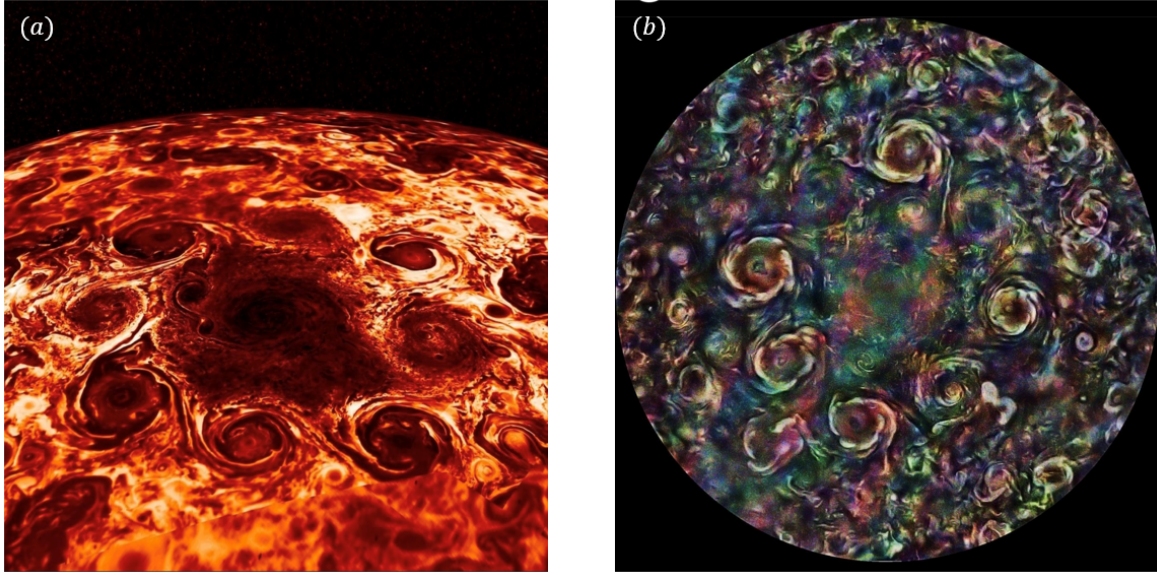


Figure 1.1: (a, b) showing image of Jupiter’s polar cyclones arranged in stable polygon pattern. (Credit: nasa.gov)

rotation, the cyclones are pushed to the polar region, where they are expected to merge and disappear. However, they remain in a stable polygon pattern. It is not clear yet whether these flows are solely driven by convection.

Because of the complexity of geophysical and astrophysical systems, the complementary approaches of experiments and numerical simulations is employed to study **RBC** in the context of these flows. In this thesis, we use a laboratory experiment to investigate the effect of roughness on rotating **RBC**. We also use numerical simulations to study rotating **RBC** to study flows with rotation perpendicular to gravity. The thesis is organized as follows: In chapter 2, we describe our experimental setup, measurement protocols. We also discuss results from our performed non-rotating experiments. In chapter 3.1, we discuss the numerical study of rotating convection with rotation vector orthogonal to gravity. In chapter 4, we conclude our results.

## 1.1 Equations of motion

The governing equation for buoyancy driven flows under boussinesq approximation in rotating frame are given by:

$$\frac{\partial \mathbf{u}}{\partial t} + (\mathbf{u} \cdot \nabla) \mathbf{u} = -\nabla P - g\beta T \hat{e}_z + \nu \nabla^2 \mathbf{u} - 2\Omega \times \mathbf{u} \quad (1.1)$$

$$\frac{\partial T}{\partial t} + (\mathbf{u} \cdot \nabla) T = \kappa \nabla^2 T \quad (1.2)$$

Here,  $\mathbf{u}$  is the velocity field,  $T$  is temperature field,  $p$  is the pressure field,  $\rho$  is the density,  $\nu$  is kinematic viscosity,  $\beta$  is the thermal expansion coefficient,  $g$  is the gravitational acceleration,  $\Omega = \Omega \hat{e}_z$  is the rotation vector, and  $\kappa$  is the thermal diffusivity. The above equations are non-dimensionalized by using free-fall velocity  $U = \sqrt{\beta g \Delta L}$  as the velocity scale,  $\Delta = T_b - T_t$  as the temperature scale, and cubic cell size  $H$  as the length scale; here,  $T_b$  and  $T_t$  are the temperature of hot(bottom) and cold(top) plates, respectively.

$$\frac{\partial \mathbf{u}'}{\partial t'} + (\mathbf{u}' \cdot \nabla') \mathbf{u}' = -\nabla' P' - T' \hat{e}_z + \left( \sqrt{\frac{Pr}{Ra}} \right) \nabla'^2 \mathbf{u}' - \left( \frac{1}{Ro} \right) \hat{e}_z \times \mathbf{u}' \quad (1.3)$$

$$\frac{\partial T'}{\partial t'} + (\mathbf{u}' \cdot \nabla') T' = \left( \frac{1}{\sqrt{Ra Pr}} \right) \nabla'^2 T' \quad (1.4)$$

Using these scales for the non-dimensionalization, we obtain three non-dimensional control parameters, namely, the Rayleigh number, Prandtl number and Rossby number

$$Ra = \frac{g\beta\Delta H^3}{\nu\kappa}, \quad Pr = \frac{\nu}{\kappa}, \quad Ro = \frac{U}{2\Omega H} \quad (1.5)$$

The Rayleigh number represents the strength of thermal forcing, Prandtl number represents the ratio of viscous and thermal boundary layer thickness and Rossby number represents ratio between buoyancy and coriolis force. Note that  $Ro$  number is an inverse rotation rate. Alternative parameters to indicate rotation rate of system are the Taylor number or Ekman number comparing viscous and coriolis forces

$$Ta = 4\Omega^2 H^4 / \nu^2, \quad Ek = \nu / \Omega H^2 \quad (1.6)$$

A convenient relationship between the different dimensionless rotation rates is  $Ro = \sqrt{Ra/(Ta Pr)}$ .

The response of the system is given by non-dimensional heat flux, i.e. the Nusselt number

$$Nu = \frac{qH}{\lambda\Delta} \quad (1.7)$$

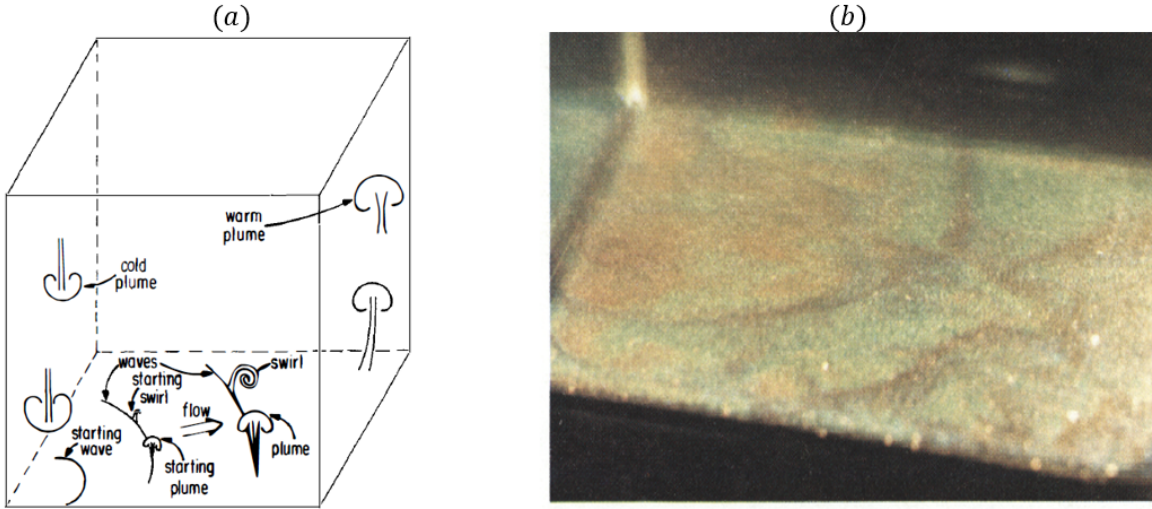


Figure 1.2: Showing a propagating perturbation wave along boundary layer from experiments [1] at  $Ra = 1.2 \times 10^9$ . Cold fluid is red, hotter fluid is green and waves are visible as dark lines.

where  $q$  is heat flux and  $\lambda$  is the thermal conductivity of fluid. There are various reasonable possibilities to choose non-dimensional velocity  $U$  and several choices have been made by different authors. A summary some work that has been done in rotating and non-rotating Rayleigh Bénard convection is given in the book by Verma [12].

## 1.2 Coherent structures in the RBC

Thermal Plumes are fragments of the thermal boundary layer, a region of high temperature gradients close to the walls, emitted randomly and continuously. They carry a fraction of the heat from the surface and move into the bulk transporting heat. The fluid in contact with the bottom heating plate rises because of a change in its density. The rising plumes hit the top boundary layer of the cell, making a splash and triggering a wave that travels along with the boundary layer [13, 14] as shown in Fig. 1.2. These waves induce secondary instabilities such as swirls (reminiscent of Kelvin Helmholtz instability), as shown in Fig. 1.2(a) and 1.3(a). These swirls travel to the opposite corner of the cell while losing their horizontal velocity. The cold plume falls from the top (reminiscent of Rayleigh Taylor instability) and morphs into a

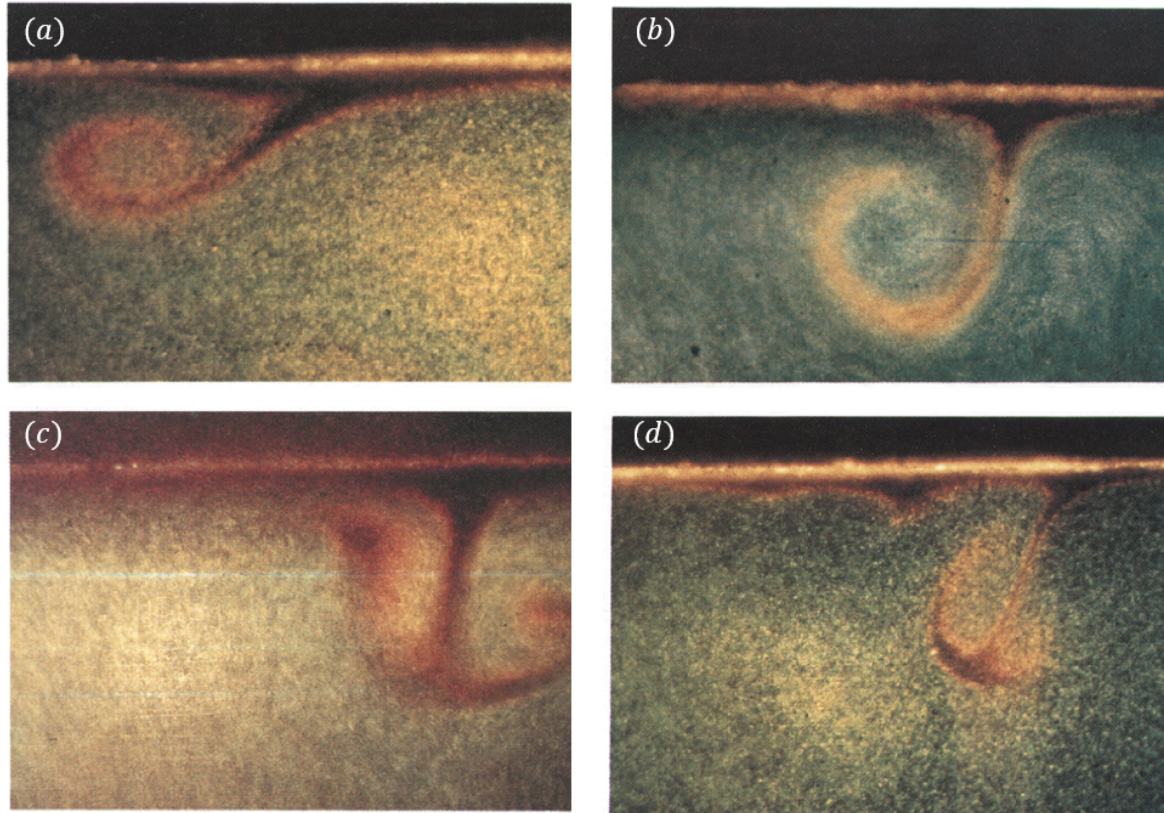


Figure 1.3: Flow visualization of coherent structures in non-rotating RBC from experiments of [1] at  $Ra = 1.2 \times 10^9$ . (a, b) Spiraling swirls gliding along top boundary. The cold fluid of boundary layer is red, warmer fluid of bulk is green and blue. (c, d) Thermal plumes emitted from boundary layer.

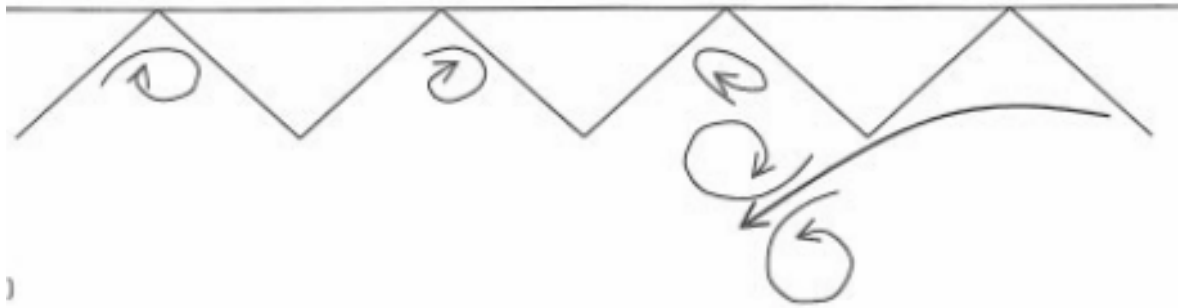


Figure 1.4: Sketch of flow near rough surface[2] in classical RBC.

mushroom shape[1, 2, 15, 16], as shown in Fig. 1.3(c) and (d). As plume (mushroom-shaped) rises, it pushes and entrains the nearby fluid, and this motion generates vortices around the plumes [16]. The plumes interact with each other via these vortices; as a result, there is a grouping and merging of plumes. This synchronization of hot/cold groups of plumes gives rise to a domain filling, self-sustaining, flywheel-like motion known as **LSC**. For non-rotating **RBC** the **LSC** exists in  $Ra$  range  $10^6$  to  $10^{12}$  [13, 17].

### 1.3 Effect of roughness on non-rotating RBC

The roughness elements perturb the flow by interacting with **LSC**. The interaction of **LSC** with roughness elements leads to the formation of secondary flow in the troughs of roughness elements [18, 19, 20]. The fluid in the trough region is nearly stagnant and does not contribute to heat transfer. However, as thermal forcing increases, the fluid in the trough region is destabilized and contributes to heat transfer [19]. For the constant heat-flux boundary condition the secondary flow in the troughs causes surface temperature inhomogeneity, as evident from experiments of Wei et al. [21] and Du and Tong [2].

The relative thickness of the thermal boundary layer ( $\delta_t$ ) with roughness height ( $k$ ) brings about a change in the way the heat is transferred in non-rotating **RBC**. The mean thickness of the thermal boundary layer ( $\delta_t$ ) is given by  $H/(2 \text{ } Nu)$ . Below a critical  $Ra$ , the thermal boundary layer is thicker than roughness. As a result the effect of roughness is not evident on heat transfer and **Nusselt number** ( $Nu$ ) for smooth surface,  $Nu_s$  is similar to **Nusselt number**

( $Nu$ ) for rough surface,  $Nu_r$ . As  $Ra$  increases, the thickness of the thermal boundary layer decreases. At  $\delta_t/k \approx 1$  [19, 22], the roughness elements start to protrude outside the thermal boundary layer and inject thermal plumes directly into the bulk flow. As a result, the heat transfer is more effective than a smooth wall case ( $Nu_r \geq Nu_s$ ).

## 1.4 Scaling law

The heat transfer in RBC is given by scaling law  $Nu = ARa^\gamma$ . Experimental study of Wei et al. [21] suggest that scaling exponent of  $\gamma = 1/3$  with smooth walls. The smooth plates are insensitive to the surface and boundary conditions of other plates of the same cell. These results also suggest that boundary layers at the top and bottom surface do not communicate. For Rayleigh numbers  $10^6 \leq Ra \leq 10^{17}$  with cryogenic helium as a working fluid, Niemela et al. [17] observed scaling exponent  $\gamma \approx 0.31$ . Chu and Goldstein [23] observed  $\gamma = 0.278$  for Rayleigh number  $2.76 \times 10^5 \leq Ra \leq 1.05 \times 10^8$  with water as working fluid. There is contentious

Table 1.1: Scaling Law in classical RBC with and without roughness ( $k$  indicates height of pyramid roughness in mm).

Scaling Law	Boundary Condition	Authors
$0.17Ra^{0.28}$	Smooth walls (SS)	Du and Tong [2]
$Ra^{0.3}$	Smooth walls (SS)	Wei et al. [21]
$\approx Ra^{0.278}$	Smooth walls (SS)	Chu and Goldstein [23]
$\approx Ra^{0.31}$	Smooth walls (SS)	Niemela et al. [17]
$0.19Ra^{0.28}$	Smooth walls (SS)	Qiu et al. [24]
$0.30Ra^{0.28}$	Rough walls	Du and Tong [2]
$Ra^{0.37}$	Rough walls	Wagner and Shishkina [19]
$0.67Ra^{0.35}$	Rough walls	Qiu et al. [24]
$\approx Ra^{0.37}$	Rough walls	Joshi et al. [8]
$\approx Ra^{0.35}$	Rough walls	Wei et al. [21]
$\approx Ra^{0.37}$	Rough walls	Stringano et al. [25]

arguemment over effect of roughness on scaling law exponent,  $\gamma$ , in non-rotating RBC. Some earlier studies (Shen et al. [22], Du and Tong [26] ) observed scaling exponent to be  $\gamma = 0.287$ , i.e, no change from smooth wall case. However, they observed heat-flux enhancement with rough walls beyond critical  $Ra$ . Villermaux [27] attributed this heat transfer enhancement to increase in surface area due to roughness elements. However, this claim has been invalidated since heat flux enhancement is not observed below critical Rayleigh number even with rough walls. Later studies ( Qiu et al. [24], Stringano et al. [25] ) observed scaling exponent  $\gamma = 0.37$ . They attribute lower  $\gamma$  scaling in earlier studies to lower thermal diffusivity of brass elements. Wei et al. [21] observed scaling exponent of  $\gamma = 0.35$  with top and bottom rough boundaries. They find that rough plates and scaling exponent are sensitive to surface conditions and BCs of opposite plates.

## 1.5 Boundary layer dynamics in smooth and rough RBC

It has long been recognized that upper and lower boundary layers play role in determining heat transfer and velocity statistics. A manifestation of this is the limitation the thickness of the thermal boundary layer imposes on the amount of heat that can be transported. In thermal convection, the thermal and viscous boundary layers are dynamically coupled to each other. The emission of thermal plumes leads to the fluctuations of thermal and viscous boundary layer thickness. This makes measurement of boundary layer thickness difficult, as measurement position will be sometimes inside and sometimes outside the boundary layers. Introducing a dynamic scaling method that expresses boundary layer quantities in a time-dependent frame that co-moves with the fluctuating boundary layer thickness alleviates the problem. The measured velocity profile, when sampled in the time-dependent frame, follows Blausius profile [28, 29]. Belmonte et al. [30] carried measurements using gas for  $Ra5 \times 10^5$  to  $10^{11}$ . They found that the  $Ra$ -dependence of thermal boundary layer thickness is close to  $Ra^{-2/7}$ . This dynamical method works not only for viscous boundary layers but also for thermal boundary layers.

The boundary layer is destabilized at the tip of roughness due to increased emission of plumes[2, 24]. While at the base of roughness boundary layer is thicker due to fluid

confinement.

## 1.6 Rotating RBC with smooth walls

As per stability analysis of Chandrasekhar [31], rotation suppresses the onset of convection by increasing critical Rayleigh number ( $Ra_{cr} = 8.75Ta^{-4/3}$ ), also called stabilizing effect of rotation. The experiments performed by Rossby [32] paradoxically reveal that after a certain critical value of rotation parameter, the heat transfer first increases with rotation. This heat-flux enhancement is attributed to Ekman pumping. Further increase in rotation results in a decrease of heat transfer as expected due to Taylor Proudmann (TP) effect. Taylor Proudman theorem: It inhibits vertical variation of velocity in inviscid regions of strongly rotating fluids. It renders flow as two-dimensional. Taylor Proudman is believed to be a higher-order function of rotation and inhibited by viscous dissipation[17, 33]. The conditions of Taylor Proudman are not strictly satisfied in rotating convection as viscous effects are present at near-wall regions. Moreover, the flow in the bulk is not steady; thus, Taylor Proudman's conditions are loosely satisfied.

### 1.6.1 Flow phenomenology

The rotation affects **Nusselt number** ( $Nu$ ), this is manifested as different regimes and flow field morphologies. Fig 1.5 shows variation of Normalized **Nusselt number** ( $Nu$ ) with rotation rate  $1/Ro$ , it shows three regimes: I, II, III which have distinct Nusselt number behaviour. The demarcations between different regimes is shown by vertical dashed lines.

- **Regime I** also called *Rotation unaffected regime* because its behavior is the same as of corresponding non-rotating case, i.e., no significant changes in Nusselt number behaviour relative to the non-rotating case. Though it has been found for small Prandtl and high Rayleigh numbers, rotation has an minor influence on Nusselt number (reason still unclear) [3, 33]. The dominant flow structure is Large Scale Circulation(LSC). Although there is not any change in Nusselt number from non-rotating convection, significant changes are occurring in the dynamics of LSC:

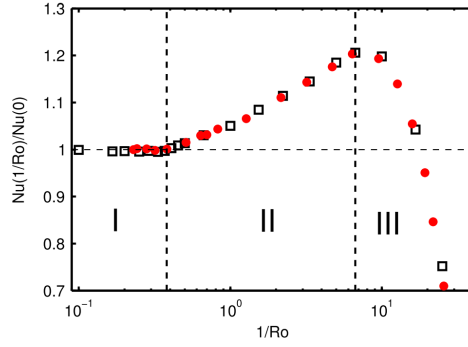


Figure 1.5: Variation of normalized Nusselt number ( $\text{Nu}$ ) [3] with rotation rate ( $1/\text{Ro}$ ) for  $\text{Ra} = 2.73 \times 10^8$ ,  $\text{Pr} = 6.86$  and  $\Gamma = 1$ . Experimental data is indicated by red dots and numerical data by open square.

- Rotation spins up the thermal plumes into vortical structures, which synchronize to give LSC. These vortical structures are more effective in carrying heat than thermal plumes encountered in non-rotating convection.
- The rotation causes LSC to describe precession against the rotating direction of the cell. This generates viscous drag at the top and bottom boundary layer, which balances Coriolis acceleration due to rotation.
- The breakdown of LSC and the start of heat transfer enhancement occurs at the Rossby number where kinetic Prandtl boundary layer thickness transitions to Ekman boundary layer [34, 35, 36].
- **Regime II** also called *Rotation affected regime*, the Nusselt number ( $\text{Nu}$ ) behaviour start to deviate from smooth wall case beyond critical rotation rate  $1/\text{Ro}_c = (0.77 \pm 0.05)\text{Pr}^{-0.42 \pm 0.04}$  [33]. Vortical columns replace the LSC as dominant flow structures for this regime. These vortical structures suck in detaching plumes and vortices from the top and bottom boundary layer, enhancing the heat transport. Figure 1.6 shows lines of constant Nusselt number ( $\text{Nu}$ ) in  $\text{Ra-Ta}$  space. For moderate rotation rates ( $10^6 \leq \text{Ta} \leq 10^8$ ) and constant Rayleigh number ( $\text{Ra}$ ) between lines L1 and L2, as we increase rotation rate ( $\text{Ta}$ ), the Nusselt number ( $\text{Nu}$ ) enhancement occurs due to Ekman pumping. The boundary layer transitions over to Ekman boundary layer,

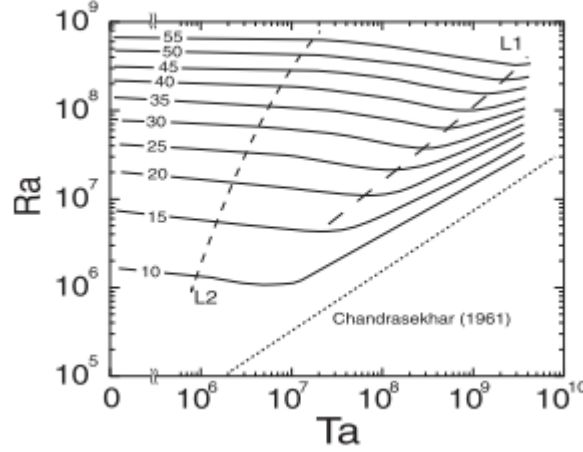


Figure 1.6:  $\text{Ra}$ - $\text{Ta}$  parameter space, line L1 is loci of maximum Nusselt number and L2 divides region between non-rotating convection and rotating convection [4].

which is analogous to the viscous boundary layer. The balance exists between pressure, Coriolis, and viscous forces inside the Ekman boundary layer. The balance is such that the velocity field forms a spiralling inward or outward flow. Mass conservation requires that converging or diverging flow should result in ascending or descending core. This transports matter from the Ekman boundary layer into bulk. The Ekman boundary layer thickness is given by  $\delta_e = 2.284\sqrt{\nu/\Omega}$  [37]. The effect of the Ekman layer is confined to the near-wall region, while in bulk, Coriolis force is balanced by pressure forces, i.e., geostrophic balance. Weiss and Ahlers [38] speculated the presence of LSC in regime II by observing the sinusoidal variation of sidewall temperatures in their experiments. However, the DNS simulations by Stevens et al. [39] attributed this sinusoidal variation to the spatial arrangement of Ekman columns.

- **Regime III** also called *geostrophic regime*, at sufficiently high rotation rates, the heat flux decreases due to the dominance of the Taylor Proudman (TP) effect over Ekman Pumping. The inability to suppress the effects of centrifugal forces make this regime difficult to access experimentally. However, experiments by Cheng et al. [5], Rajaei et al. [37] have accessed this regime. Due to such high rotation this regime is also called

*rotationally constrained regime.*

There is contentious argument over transition between regimes II (rotation affected) and regime III (rotationally constrained). Generally one would have perception that force balance between buoyancy and coriolis dictates the transition. In another words for **Rossby number** ( $Ro$ )  $\leq 1$  we transition to geostrophic regime. However, experimental measurement of Liu and Ecke [4] suggest transition to geostrophic regime occurs at Rossby ( $Ro$ ) = 0.1 or equivalently  $\delta_t \approx 2\delta_e$ . Authors King et al. [40], King and Aurnou [41], found transition is depicted by relative thickness two competing boundary layers: thermal boundary layer ( $\delta_t$ ) and Ekman boundary layer ( $\delta_e$ ). At the transition,  $\delta_t/\delta_e \approx Ra^{-1/3}/Ek^{1/2} \approx 0(1)$  or  $RaEk^{3/2} \approx 0(1)$ . In regime III, Ekman boundary layer is thinner than the thermal boundary layer ( $RaEk^{3/2} < 10$ ), the effect of the thermal boundary layer is truncated into the bulk fluid. While on increasing  $RaEk^{3/2}$  the thickness of thermal boundary layer decreases below the Ekman boundary layer and transition to rotation unaffected regime takes place. From above arguments we can infer that geostrophic regime occurs in range:  $Ra_c (\approx Ek^{-4/3}) < Ra < Ek^{-3/2}$ .

Table 1.2: Transition boundaries for regimes I, II and III in Rotating RBC.

Regime	Transition Boundary	Pr	Reference
I to II	$Ra = 0.086Ek^{-2}$	6	Joshi et al. [8]
II to III	$Ra = 1.4Ek^{-7/4}$	7	King et al. [40]
II to III	$Ra = 1.4Ek^{-3/2}$	4.5 – 11	King et al. [40]

The transition boundaries between regime I, II, and III is given in table 1.2. The geostropic regime is further divided in sub-categories:

- **Cellular regime:** They are unsteady cellular states with a high degree of vertical coherence and are observed just above the critical onset value  $Ra/Ra_c$ .
- **Convective Taylor Columns (CTC) regime:** With increasing **Rayleigh number** ( $Ra$ ), the boundary layer becomes unstable to convective motion, which results in cyclonic and anticyclonic thermal plumes that penetrate the cellular interior.

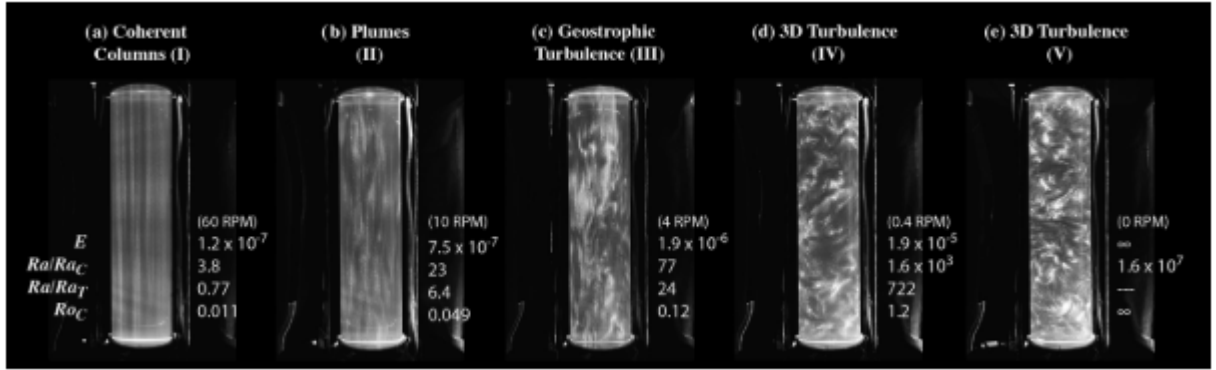


Figure 1.7: Laboratory Visualisation of Various Regimes with water as working fluid at different Ekman number in 80cm High by 20cm wide tank heated at constant heat flux [5]

The plumes remain attached to the boundary layer and synchronize with plumes emanating from the opposite boundary layer. This results in tall, roughly vertical thermally active columns known as **CTC**, as shown in Fig. 1.7(a). Width of **CTC** scales as  $Ek^{1/3}H$ [42]. These flow structures wander about horizontally, pumping warm fluid from bottom to top. The **CTC** has a very bizarre structure, vortex core are shielded by oppositely signed vorticity [37, 43]. The shielding acts like a blanket preventing vortex-vortex interaction. The shielding gets weaker as we increase the thermal forcing. The occurrence of this regime depends on Prandtl number, for low Prandtl number fluids, the thermal anomaly carried in **CTC** may be more effectively diffused, and column may not extend across layer (restricted to thermal boundary layer) [41]. Although these columns extend between top and bottom boundary layers, the heat transfer is lower (around 30%) than compared to regime II. At higher rotation rates occurring in regime III, the vertical fluctuations are suppressed, which otherwise contribute to heat transfer.

- **Plume region:** This is the transition region from **CTC** to a non-linear, less viscous regime, as shown in Fig. 1.7(b). The **CTC** begins to lose their vertical coherence (synchronization) as well as a shield which results in vortex-vortex interaction and lateral heat loss.
- **Geostrophic turbulence regime:** At higher rotation rates and small viscosity

(higher Rayleigh numbers), the plumes are confined entirely inside the thermal boundary layer [43]. This leads to less viscous well mixed interior generated by vortex-vortex interactions, as shown in Fig. 1.7(c). The pressure gradient balances the Coriolis force. For  $Pr < 1$  with free slip conditions, DNS and asymptotically reduced studies observe inverse cascade of energy from small scale to large scale vortices. But with no-slip boundary conditions at such high rotations ( $Ro \approx 0.04$ ), the inverse cascade is absent due to injection of small scale vortices by diminishing Ekman boundary layers [44]. These small scales hinder the formation of large-scale structures. The heat transfer with no-slip boundary condition is higher than free slip due to the absence of large-scale vortices and the presence of Ekman pumping. This regime is difficult to approach experimentally because centrifugal forces start to come in at such high rotation rates.

### 1.6.2 Effect of flow parameters on RBC

The Rayleigh Bénard flow is rich flow, and flow physics is sensitive to parameters like aspect ratio, Rayleigh number ( $Ra$ ), and Prandtl number ( $Pr$ ). For efficient heat transport, Ekman pumping should draw fluid from the thermal boundary layer. Thus, the relative thickness of boundary layers, controlled by Prandtl number ( $Pr$ ), affects Ekman pumping efficiency. For the non-rotating case, the crossover between the thermal and viscous boundary layer occurs at  $Pr = 1$ , i.e., the kinetic viscous boundary layer is thicker than the thermal boundary layer for  $Pr > 1$  and vice-versa. With rotation applied, the kinetic viscous boundary layer transitions to the Ekman boundary layer, which scales as  $Ro^{-1/2}$ . Fig. 1.8 shows variation of normalized Nusselt number ( $Nu$ ) with rotation rate ( $Ro$ ). It is evident from the Fig. 1.8 (a), as the Prandtl number ( $Pr$ ) increases, the transition to regime III or maxima of normalized Nusselt number is delayed to a higher rotation rate (lower  $Ro$ ). The plausible reason is the crossover between Ekman and thermal boundary layer occurring at a higher rotation rate for high Prandtl number.

*For too low Prandtl number ( $Pr < 0.7$ ), the Ekman boundary layer is nested within the thermal boundary layer. And the hot fluid enters vortices, but high thermal diffusivity facilitates enhanced horizontal heat transport from columns. As a result, Ekman columns*

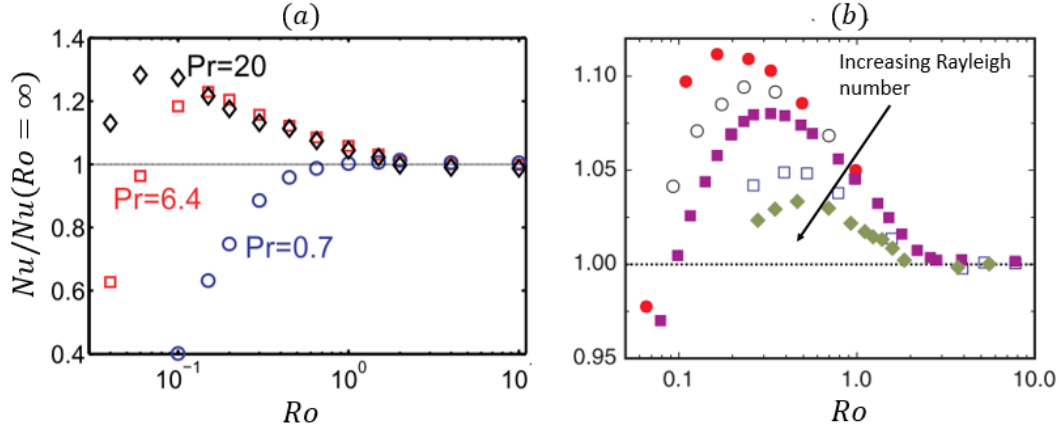


Figure 1.8: Shows effect of Rayleigh and Prandtl number on rotating RBC with smooth walls. (a) Shows variation of normalized Nusselt number  $Nu/Nu(Ro = \infty)$  with Rossby number ( $Ro$ ) for different Prandtl number ( $Pr$ )[6]. (b) Shows variation of normalized Nusselt number  $Nu/Nu(Ro = \infty)$  with Rossby number for different Rayleigh numbers[7].

are shorter and broader, which makes Ekman pumping inefficient. At low Prandtl number ( $Pr$ ), TP effects dominates suppressing vertical velocity fluctuations at lower rotation rates [6, 7]. This dominance of TP effect is manifested by reduced maxima of  $Nu(\Omega)/Nu(\Omega = 0)$  and narrower heat enhancement range in Fig. 1.8 (a) for decreasing  $Pr$

*While if Prandtl number is too high, the thermal boundary layer is nested within the Ekman boundary layer. And the Ekman pumping, which draws the fluid from the bulk of boundary layer rather than near-wall [8] never reaches thermal boundary layer, thus limiting the effect of Ekman pumping.*

*Effect of Rayleigh number,* TP effect becomes stronger at higher Rayleigh number [7, 33], which is manifested by diminishing Nusselt number enhancement, as seen in Fig. 1.8 (b). At very high Rayleigh numbers ( $Ro \geq 10^{13}$ ), viscous forces are suppressed. TP effect becomes strong enough to eliminate any heat-flux enhancement, i.e., regime III starts as soon as  $1/Ro$  exceeds zero [45].

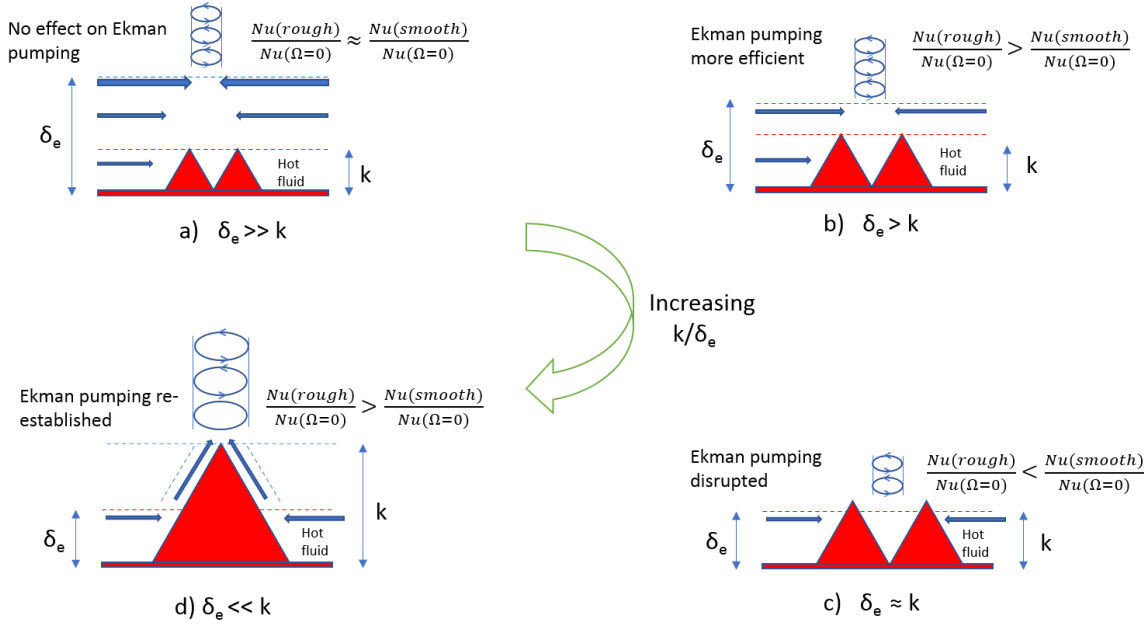


Figure 1.9: Schematic showing disruption and re-establishment of Ekman pumping in rotating Rayleigh Bénard flow with rough boundaries.

## 1.7 Rotating Rayleigh Bénard Convection with roughness

In literature effect of roughness and rotation has been studied separately, combined effect of rotation and roughness has not been given much attention. Joshi et al. [8] were the first to report the effect of roughness on rotating Rayleigh-Bénard convection. The relative thicknesses of boundary layers (thermal and Ekman) relative to roughness govern the heat transfer. As long as roughness is buried inside the Ekman boundary layer ( $\delta_e \gg k$ ), its effect is not evident. As the rotation rate increases, the ratio  $k/\delta_e$  increases, as shown in Fig. 1.9. When  $k/\delta_e$  becomes high enough that roughness elements get exposed to strong radial inflow of boundary layer fluid into the Ekman vortices. At Rayleigh number ( $Ra$ ) where  $\delta_t \approx k$ , the radial flow over roughness elements is likely to generate more thermal structures/fluctuation from perturbed thermal boundary layer and enforcing the Ekman pumping as shown in Fig. 1.9(b). Fig. 1.10(a), from measurements of Joshi et al. [8], shows the maxima of normalized Nusselt number ( $Nu$ ) curve shifted to higher rotation rate or lower  $Ro$ , i.e., transition to regime III is delayed. This is expected since rough surfaces increase turbulence; thus higher

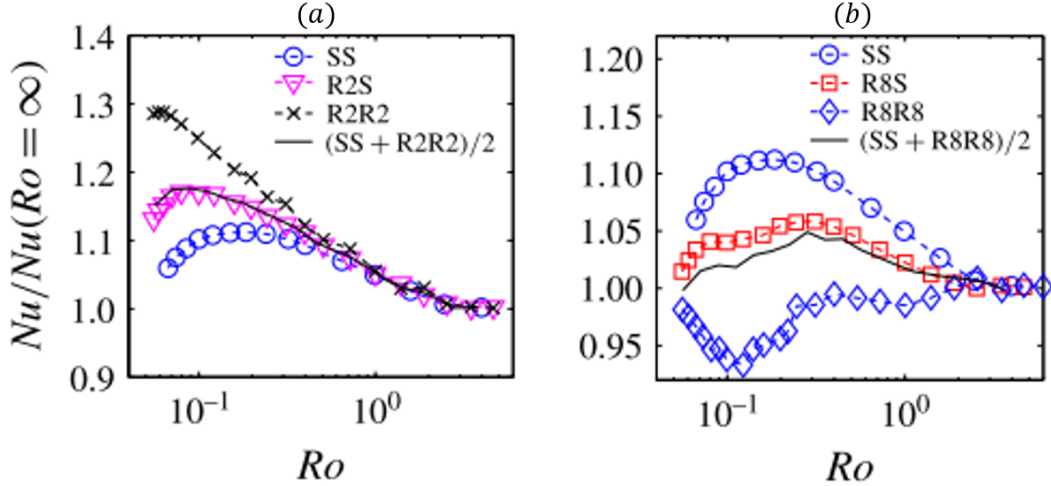


Figure 1.10: Variation of  $Nu/Nu(Ro = \infty)$  with Rossby number for different roughness. (a) Compares behaviour of R2R2 ( $k=1.5$ ), both walls rough; R2S, one rough and one smooth walls; with smooth wall case. (b) Compares behaviour of R8R8 ( $k=8$ ), both walls rough; R8S, one rough and one smooth walls; with smooth wall case. [8].

rotation rate is required to dampen them.

The qualitative and quantitative behavior changes from smooth wall case where  $\delta_e \approx k$ , as shown in Fig. 1.10(b) and 1.9(c). Here, roughness elements strongly perturb the Ekman boundary layer, and this may lead to disruption of the Ekman pumping mechanism. Thus there is no heat flux enhancement when  $\delta_e \approx k$ . On decreasing Rossby number, rotation further dampens turbulence— as a result, the normalized Nusselt number starts to decrease, as shown for R8R8 in Fig. 1.10(b). However, when  $\delta_e \ll k$  the Nusselt number ( $Nu$ ) starts to increase. It may be possible that at these high rotation rates, the Ekman boundary layer is so thin that it follows sloping boundaries of roughness, as shown in Fig. 1.9 (d). This may re-establishes the Ekman pumping, and heat transfer starts to increase with the increase in rotation as shown in Fig. 1.10 (b).

We designed our experiment to observe the disruption and re-establishment of Ekman pumping. According to Joshi et al. [8],  $\delta_e \approx k/4$  is sufficient for the re-establishment of Ekman pumping.

# Chapter 2

## Experimental setup and measurements

In this chapter we describe the experimental setup along with the measurement methods used for the Nusselt number measurements. The experimental setup is designed to investigate the effect of roughness and rotation on natural convection. We also describe the modifications required for [PIV](#) measurements.

### 2.1 Experimental setup

The experimental setup consists of a rotating table and a Rayleigh Bénard convection ([RBC](#)) cell. Our main diagnostics for the experiments are Nusselt number measurements and particle image velocimetry ([PIV](#)). Both diagnostics use the same [RBC](#) cell, with slight modifications. In sections that follow we describe our setup along with their sub-components.

#### 2.1.1 RBC cell

The convection cell is designed to investigate the effect of roughness and rotation on natural convection. The experimental results of Joshi et al. [8] indicates Ekman boundary layer is strongly perturbed by roughness elements , when  $\delta_e \approx k$ , leading to suppression of Ekman pumping. However, Ekman pumping is re-established at rotation rates when the Ekman

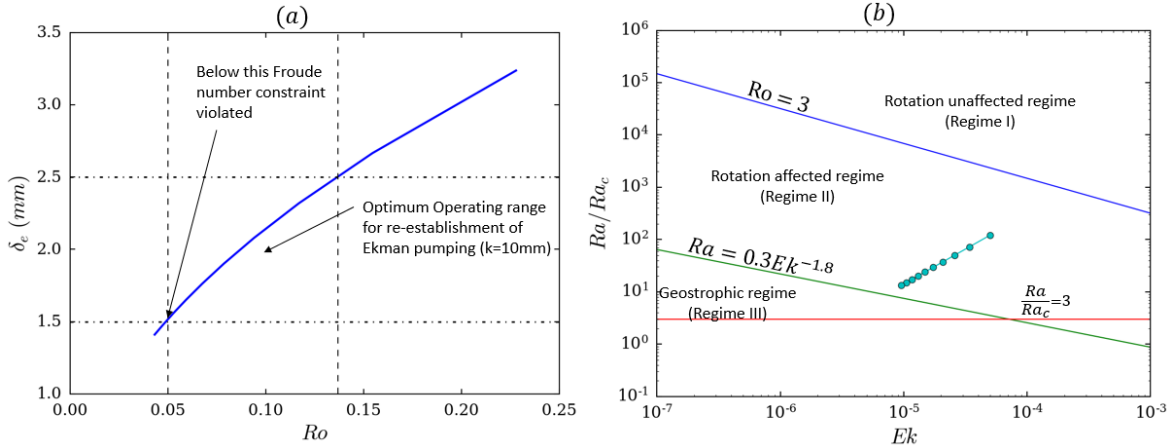


Figure 2.1: (a) Variation of the Ekman boundary layer thickness ( $\delta_e$ ) with Rossby number ( $Ro$ ). (b) Various regimes observed in rotating Rayleigh-Bénard convection, the given cyan dots shows our planned experimental parameters.

boundary layer attains thickness  $\delta_e = k/4$ . Keeping these in mind, we choose pyramid-shaped roughness with height ( $k$ ) = 10 mm. The variation of the Ekman boundary layer thickness with Rossby number (inverse of rotation rate) is shown in Fig. 2.1 (a). The highest rotation rate (lowest  $Ro$ ) is constrained by the Froude number ( $Fr \leq 0.1$ ), to minimize centrifugal effects. The Froude number constraint and the criteria for the re-establishment of Ekman pumping define our operating range of rotation rates, i.e.,  $0.05 \leq Ro \leq 0.135$ . The same Rossby number range is superimposed on Fig. 2.1 (b), it shows the various regimes observed in the  $Ra/Ra_c - Ek$  space [45]. Our operating range is confined within regime II and very near to the geostrophic regime.

The convection cell used for PIV experiments is shown in Fig. 2.2. A top copper plate replaces the cooling manifold for Nusselt number measurements. RBC cell consists of three main parts: (i) Heated plate assembly at the bottom, (ii) Top copper plate/cooling manifold, and (iii) square acrylic chamber between bottom and top copper plates.

The *bottom plate assembly*, as shown in Fig. 2.2(b) and Fig. 2.3(a), consists of a rough copper plate encased with hylam insulation. Copper serves as a heat reservoir as well as means to perturb the flow with pyramid-shaped roughness that has been machined directly on a forged copper block. The dimensions of the bottom copper plate are 240mm×240mm×50mm. Tri-

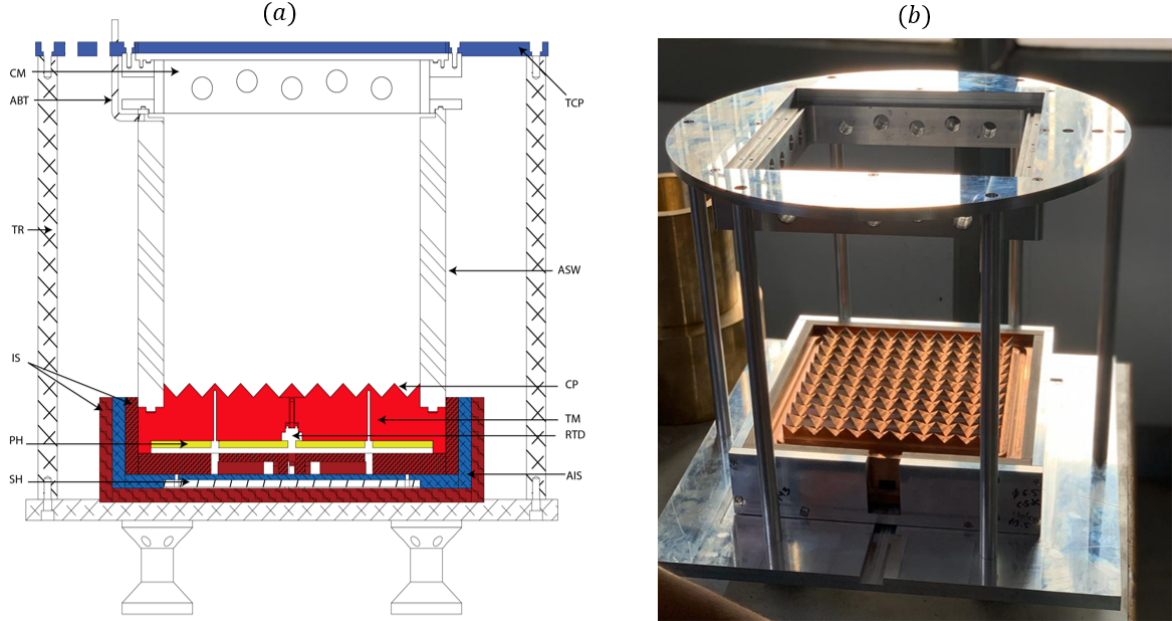


Figure 2.2: (a) Schematic of the **RBC** cell for PIV experiment: TCP, top cover plate; CM, cooling manifold; ABT, air bleed tube connected to overhead reservoir; ASW, acrylic side-walls; TR, tie rods; CP, copper plate; TM, NTC thermistors holes; RTD, holes for Pt100 RTD; IS, hylam insulation; PH, primary heater; SH, secondary heater; AIS, aluminium insulation. (b) The fabricated **RBC** cell for the planned **PIV** experiments.

angular grooves with vertex angle  $90^\circ$  have been machined directly on surface of these plates. The spacing of grooves is such that they form square lattice of pyramids roughness on the surface over area of  $200 \times 200 \text{ mm}^2$ . The pyramid roughness have roughness height of 10 mm and square base of side 20 mm. Surrounding the roughness elements area, a section is provided that has an o-ring groove machined on it. On the bottom side of the copper plate, a 9mm deep square recess is provided that seats the primary heater. There are eight thermistors holes drilled into copper block from bottom side. Four of these thermistor holes penetrate into the pyramid upto depth 5 mm beneath pyramid tips. The rest four holes are 3mm underneath valleys. A central hole to mount the **RTD** is machined to 3mm below the pyramid base. In order to minimize heat loss from the bottom copper plate, we surround it with hylam insulation, which has a sidewall thickness of 10 mm and a base thickness of 15 mm. It is a cotton-based composite impregnated with epoxy resin which acts as the matrix

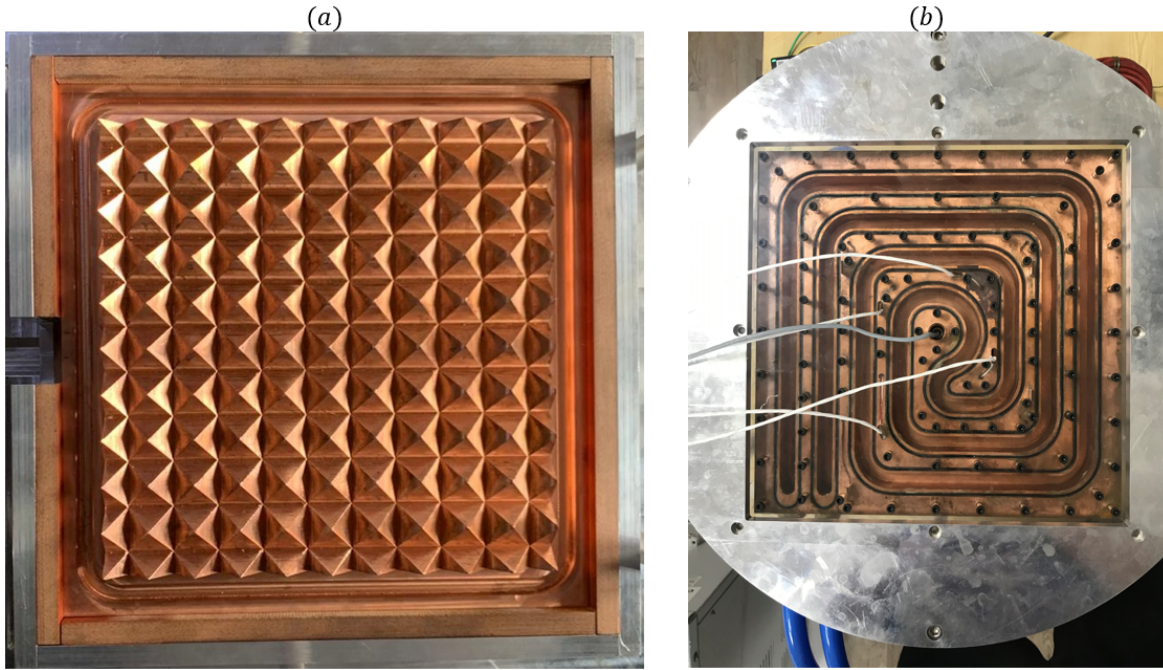


Figure 2.3: (a) Copper plate encased in hylam insulation and (b) spiral grooves of the top copper plate.

of the composite. Its composition makes it a good electrical and thermal insulator ( $\lambda = 0.23 \text{ W}/(\text{m K})$ ) with sufficient compressive strength.

To further minimize heat loss from the bottom copper plate, we use an aluminum casing having dimensions  $260\text{mm} \times 260\text{mm} \times 65\text{mm}$  to surround inner hylam insulation and copper block. At the base of the aluminum casing, 3 mm deep recess has been machined to mount the secondary heater. It is controlled by a secondary power supply operating in a feedback loop. The feedback loop maintains the temperature of the aluminum casing same as copper plate, which minimizes heat loss from copper. Rather than being fabricated from a single aluminium block, it has a base and sidewalls held together by countersunk screws. This makes the assembly flexible and allows us to accommodate machining errors that are unknown beforehand. An additional layer of hylam insulation is used, machined similar to the aluminium casing; it cascades aluminium casing, inner hylam insulation, and copper block. Its main function is to minimize heat loss from the aluminum casing, which facilitates the use of a low wattage power supply for the secondary heater.

*Square acrylic chamber* forms the side-walls of the RBC cell, see Fig. 2.2(a). The square cell precludes distortion of light in PIV experiments, which otherwise would be present in a cylindrical one. The acrylic side-walls obviate the need for insulating them, as acrylic is a good insulator. However, we use thermocol to insulate sidewalls for Nusselt number measurements. The acrylic side-walls are 20 mm thick, and they form hollow square chamber with internal dimensions 200mm×200mm. Onto the top of the acrylic chamber, the cooling manifold/top copper plate is seated depending on the variant of the experiment. The acrylic square cell sits on an o-ring groove machined in the bottom copper plate as shown in Fig. 2.2 (a). The top of the acrylic sidewalls has a step, 8mm wide and 6mm deep, running along the inner periphery. This provision locates the cooling manifold over the acrylic chamber.

*Cooling Manifold:* The cooling manifold, used in the PIV variant of the experiment, is mounted on top of the acrylic chamber. It is a machined aluminium box with an inside cavity of size 220mm×220mm. The inside cavity corners of cooling manifold have been rounded to avoid fluid accumulation at corners. At the base of the cooling manifold, there is a 3 mm protrusion onto which sapphire is glued and rests inside the step on top of the acrylic chamber. The sapphire with dimensions 212mm×212mm×2mm, acts as an interface between working fluid and the cooling water flowing through the manifold. There are five input/output channels machined in a zig-zag pattern on each face of the manifold. These channels are being used in such a combination to get maximum mixing in the chamber. The chamber is closed at the top by a 5 mm acrylic sheet, while at the bottom, it conducts heat through the sapphire sheet. An duplex four wire RTD-(Pt100) sensors monitors and controls the water temperature inside the cooling manifold. One sensor is connected to cDAQ chassis NI-9189, and the other is connected to the PID controller of the recirculating chiller unit.

*Top copper plate* The top copper plate is similar to the bottom copper plate except that it has spiral grooves machined on the opposite side of roughness, see Figs. 2.3 (b) and 2.4. The spiral grooves allow the flow of cooling water from the chiller. The grooves have rounded corners to minimize head loss. The depth of grooves is such that they reach 5mm beneath roughness valleys, as shown in Fig. 2.4. This ensures uniform temperature within the plate and a shorter response time to attain desired temperatures. The spiral grooves along their periphery have o-ring grooves, as shown in Figs. 2.3 (b) and 2.4. An acrylic plate of 15 mm

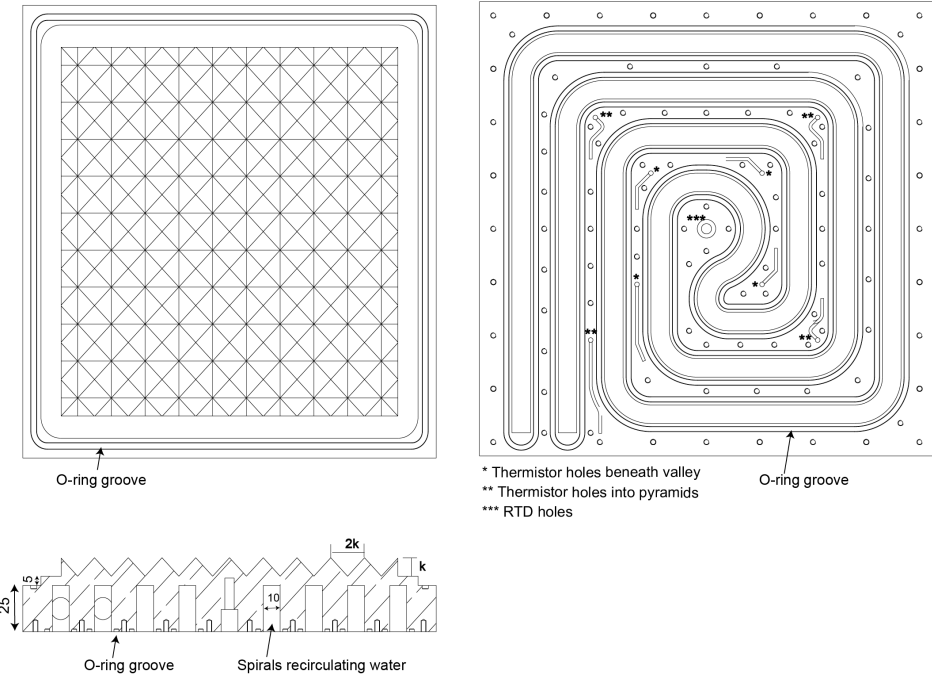


Figure 2.4: Schematic of Top copper plate

thickness sits over the o-ring groove and is attached to the top copper plate using screws, making the sub-assembly leak-proof. The top aluminum cover is placed over this acrylic plate, and the whole assembly is locked by six tie rods.

### 2.1.2 Rotating table facility

The Rotating table assembly consists of a rotating table, rotary mechanism, and structural support members. Fig. 2.5 shows a schematic of the rotating table. The structural support members are the bottom datum plate, and the four mild steel pillars over which the platform is mounted and fixed with bolts. The platform has a central hole with a recess to locate the housing. The pillars and non-rotating table are machined to have sufficient flatness. We now describe each sub-assembly:

*Rotating table* is a platform over which the RBC cell and other accessories are mounted. The table is 800 mm in diameter and 10 mm in thickness, see Fig. 2.6a. It is supported by spyder assembly, shown in Fig. 2.6b. The spyder assembly consists of a central hub with cutouts for wires and fluid pipes. Four tongs are welded to the central hub of spyder assembly, onto

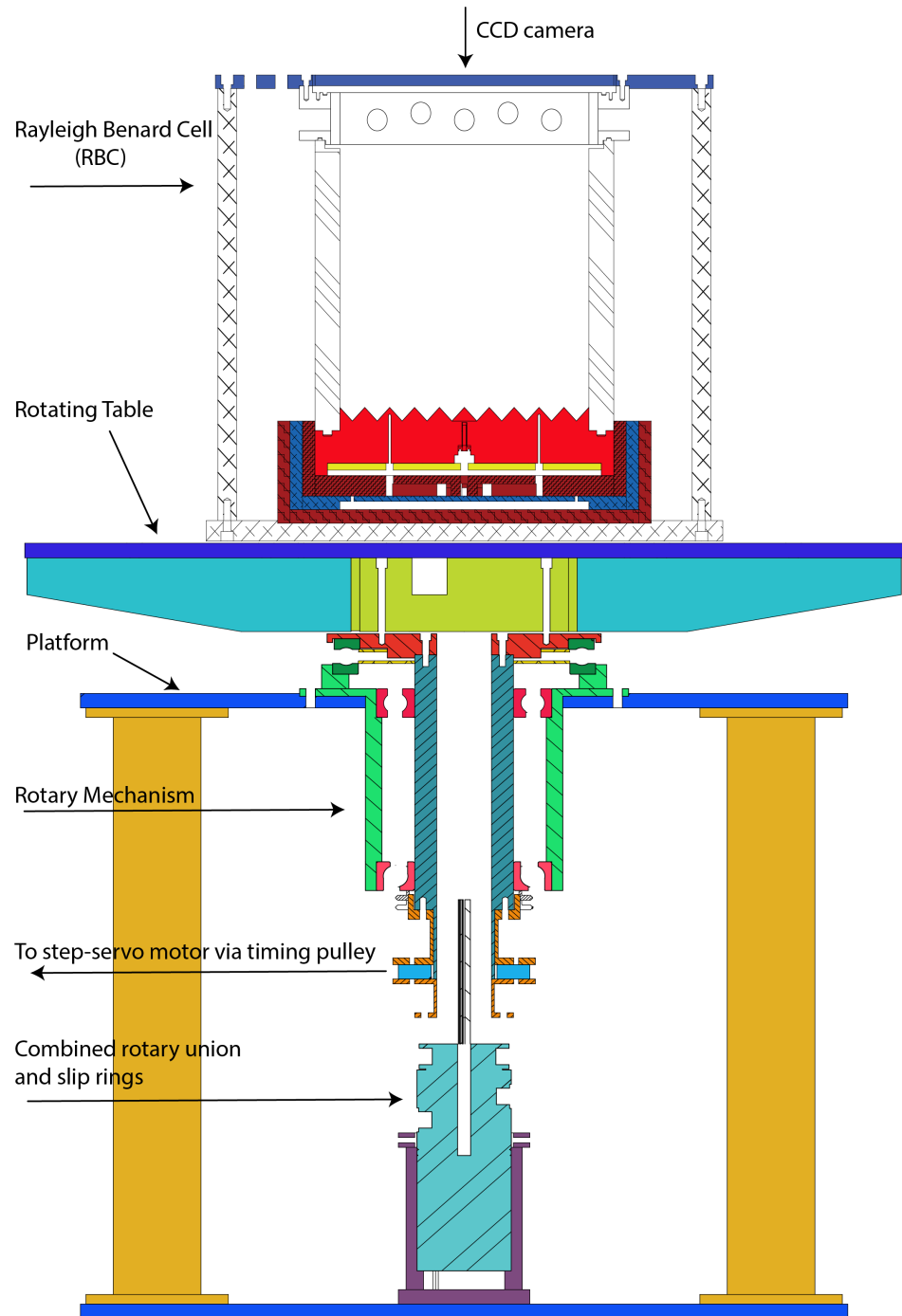


Figure 2.5: Schematic of experimental apparatus for Rotating Rayleigh Benard convection with rough plates.

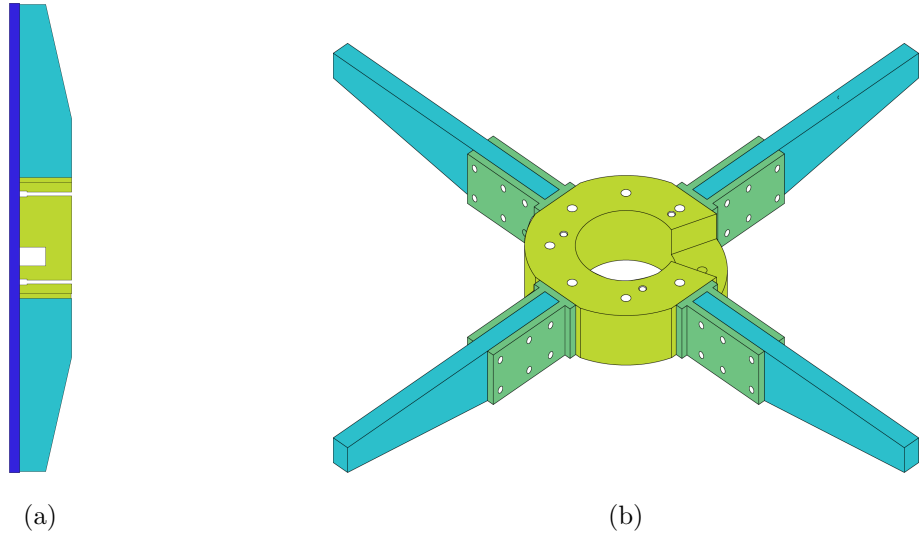


Figure 2.6: (a) Rotating table sub-assembly, (b) Spyder assembly that supports rotating table.

which four ribs are attached with bolts. The ribs prevent the rotating table from bending against compressive loads of mounted RBC cell and auxillaries.

*Housing* is a stationery member which houses four rotating components: three bearings and a shaft. Recesses are machined into which outer races of three bearings are mounted: Deep Groove Ball Bearing (ZKL-6218), Angular Contact Ball Bearing (ZKL-7218) and Thrust Ball Bearing (ZKL-51138). The deep groove ball bearing can take radial loads; to some extent, they can sustain axial loads also. The angular contact bearing can sustain both radial and axial loads. This combination of two ball bearings, as shown in Fig. 2.7, supports the shaft radially to minimize its tilting due to belt tension. We use a pair of locknuts to secure the bearings and prevent the loosening of components due to vibration and rotation. The locknuts are internally threaded, meshing with external threads on pulley mount, and pushing against the angular contact bearing to apply pre-tension to the shaft. This pre-tensioning pulls the intermediate plate against the thrust bearing and ensures that there is no axial play in the assembly. The housing prevents any misalignment between bearings, shaft, and rotating table by holding them all concentric.

The *Shaft* has been constructed in a hollow cylindrical fashion. Hollow shafts are better

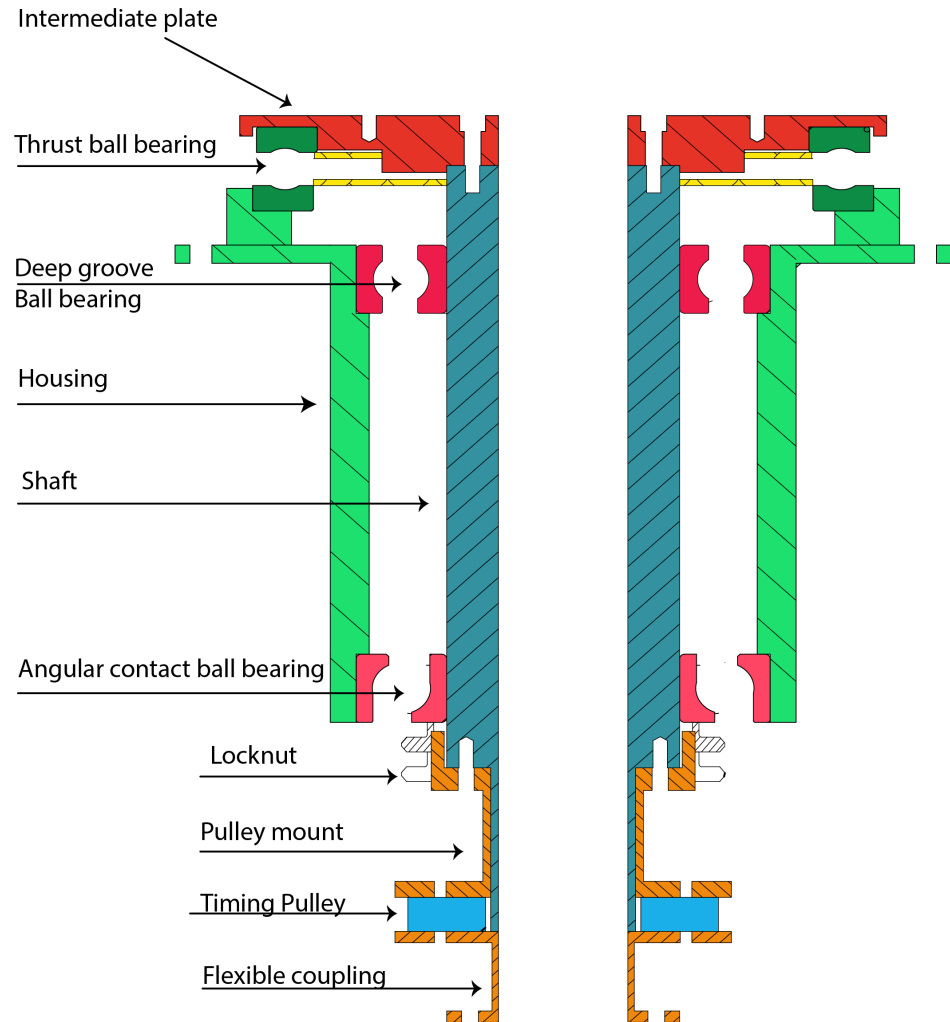


Figure 2.7: Housing and Shaft Assembly

than solid shafts in terms of power transmission for the same weight. Apart from power transmission, the hollow shaft facilitates the transfer of cooling fluid and electric wires coming out of the rotary union and slip rings. The shaft has an interference fit (H7) with all three bearing's inner races. The shaft is made of mild steel with an outer diameter of 90 mm over a length of 260mm, and is then stepped down to a diameter of 56 mm over a length of 72 mm. This stepping provides a footing over which the pulley mount is attached by six M6 bolts.

The *Pulley mount* is a power transmission member mounted on the shaft. At one end, it has a cup-like feature that is threaded on the outer surface and goes over the shaft. As mentioned

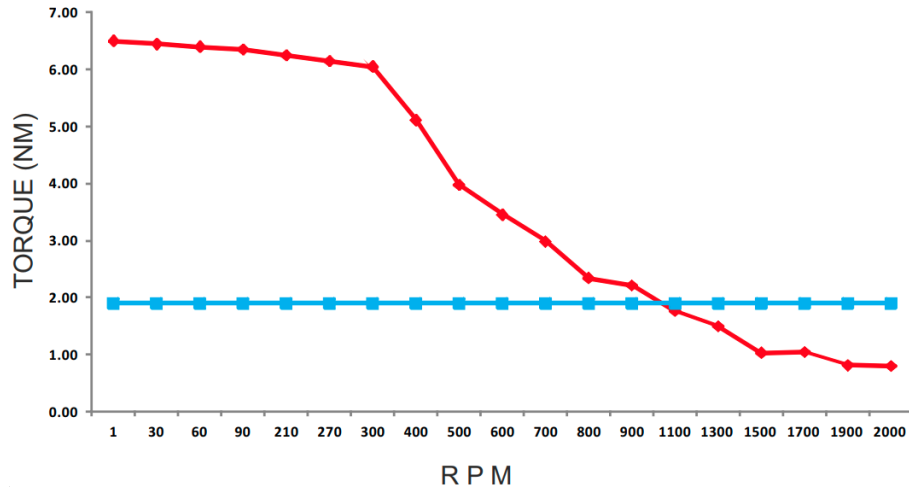


Figure 2.8: Torque Characteristics of step-servo and servo motors . Red line indicates 600W step-servo motor and blue line indicates 600W servo motors.

earlier, two locknut mesh with these threads. The other end of the pulley mount has a flange to which the pulley is connected, as shown in Fig. 2.7.

*Combined rotary union and slip-ring* (or swivel joint) is a mechanism used to transfer fluid (under pressure or vacuum) from a stationary inlet to a rotating outlet or vice-versa. We have used a combined rotary union + slip ring provided by SENRINGS -(3002012-17-52454-1) to overcome space constraints. It has two water circuits (one for inlet and the other for outlet), four 10A wires, ten 5A wires, four 2A wires, and 1GBPS Ethernet. It can handle pressures up to 1MPA. The body is of stainless steel and can handle water or other corrosive media.

*Coupling* has the same construction as the pulley mount, with the only difference being that instead of having a cup-like feature, it has a flange at both ends. It acts as a flexible coupling between the rotating assembly and the rotary union, i.e., drives slip ring in synchronization with rotating assembly.

### 2.1.3 Motor assembly

The rotating table is driven by electric step-servo motor [46]. A stepper motor operates using electrical pulses; one pulse corresponds to rotation of  $1.8^\circ$ . At higher rotation rates, a large number of pulses per second are fed to the motor, of which some may be missed by the

motor. The step-servo motor alleviates this problem by employing an active feedback (optical encoders) mechanism, which allows precise position control of the motor and compensates for the lost pulses. The torques provided by these motors are higher than the corresponding servo-motors, as shown in Fig. 2.8. For our operating range ( $< 100\text{RPM}$ ) step-servo motors are better than servo motors. However, servo-motors are better than step-servo motors for higher rotation rates ( $> 1000\text{RPM}$ ). The motor drives the timing pulley (positive drive) mounted on the shaft. The ratio between the radius of driving to driven timing pulley is 1:4. Due to this gear ratio the torque on the driven pulley amplifies four-folds. The timing belt used is HTD 5M (pitch is 5 mm, and the centre to centre distance between the pulleys is 300 mm). To control the torque precisely and have a jitter-free operation, we drive the motor at 128 micro-steps per step. The motor and the driving pulley are mounted on rails fixed to the bottom datum plate, that facilitates maintaining appropriate belt tension.

## 2.2 Data acquistion, thermometry and control system

The data acquisition system consists of NI-cDAQ 9189 chassis, an 8-channel **RTD** temperature module (NI-9216), and two 4-channel universal input modules (NI-9219). For temperature measurement, we use Resistance Temperature Detectors (**RTD**) and **NTC** Thermistors. **RTDs** are temperature sensors in which the resistance depends on the temperature; when the temperature changes, the sensor resistance changes. So by measuring the sensor resistance, **RTD** can be used to measure the temperature. **RTDs** are commonly made from Platinum, which has a linear temperature-resistance relationship. The most commonly used **RTD** is Pt100, made of platinum and having a resistance of  $100 \Omega$  at  $0^\circ\text{C}$ . All the **RTD** sensors used in this study need external excitation and have 4-wires, i.e., separate circuits for voltage and current measurement by the module, which helps in lead wire compensation. The Pt100 sensor used in our experiments has two configurations, namely, simplex and duplex. In the simplex configuration, only one Pt100 sensor is used inside the probe casing, while for duplex, we use two Pt100 sensors in the same probe casing. The duplex **RTD** allows us to use one of the Pt100 sensors in the **PID** control system and the other to record the resistances. We have a simplex **RTD** mounted inside the bottom copper plate and duplex **RTD** used on the

top copper plate, Fig. 2.9(a), and in the cooling manifold.

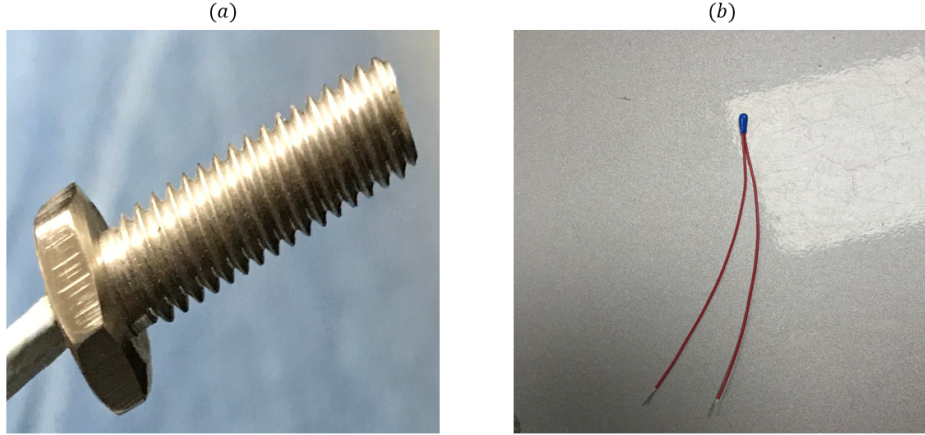


Figure 2.9: Sensors used in the experiments. (a) threaded RTD used in the top copper plate. (b) Bead-shaped NTC thermistor.

Negative temperature coefficient (NTC) thermistors (TK95F232VN-Amphenol) with a resistance of 2250 Ohms at 25°C have been used in the present experiments to measure temperature fluctuations. The universal input NI-9219 module can measure resistance up to 10000  $\Omega$ , which puts a constraint on the minimum temperature that can be measured. These NTC thermistors have a bead-shaped head with a diameter of 2.4mm, see Fig. 2.9(b). On both the copper plates, we have holes of diameter 2.5 mm to accommodate the thermistors. Each plate has two sets of holes for the thermistors, out of which one set is beneath the valleys, and the other is beneath the pyramid peaks. The two sets of holes allow us to measure the temperature in the groove region as well as of inside pyramid roughness.

For calibration of these sensors, we use a standard calibrated RTD (calibration certificate provided by the vendor). We dipped all sensors (RTD + thermistor) along with the standard sensor into a chiller bath, maintaining a constant temperature. We then record resistances of these sensors at various temperatures and fit the following equation for RTD,

$$R = R_0 + AT + BT^2 \quad [47] \quad (2.1)$$

where  $R$  is resistance in ohms ( $\Omega$ ) and  $T$  is in  $^{\circ}\text{C}$  for our RTD mounted on top copper plate we have  $R_0 = 100.02$ ,  $A = 3.92 \times 10^{-1}$ ,  $B = -3.73 \times 10^{-5}$ . The fitted curve to data is shown in Fig. 2.10(a). For thermistors we fit the following equation,

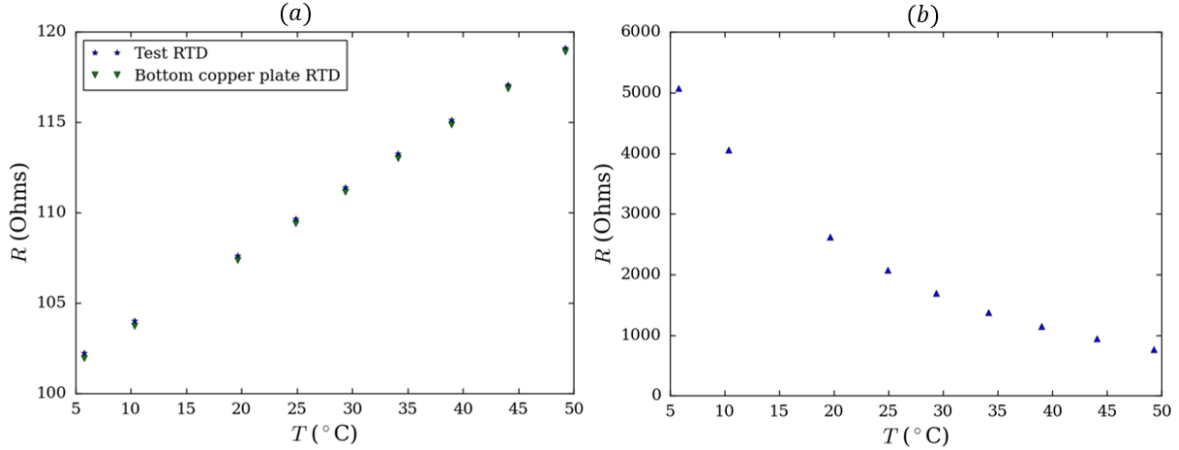


Figure 2.10: R-T curve for the sensors used in our experiments. (a) RTD (Pt100), (b) NTC thermistors.

$$1/T = A + B \ln R + C(\ln R)^2 + D(\ln R)^3 \quad [47] \quad (2.2)$$

the fitted values for our 4-wire thermistor are:  $A = 6.69 \times 10^{-3}$ ,  $B = 1.86 \times 10^{-3}$ ,  $C = 2.77 \times 10^{-4}$ ,  $D = -1.17 \times 10^{-5}$ . The fitted curve to data is shown in Fig 2.10(b).

### 2.2.1 PID

To maintain the temperature of the rough plate(bottom) constant, we employ a Proportional, Integral, and Derivative (PID) controller designed using LabVIEW. It is a control loop employing feedback and is widely used in industry. Fig. 2.11 shows a schematic of the PID controller. We have used PID VI available in LabVIEW library, in conjunction with a VI designed to control our power supply using SCPI commands. The LabVIEW program acquires resistance data through DAQ modules (RTD + thermistors) and, using calibration constants, converts them to the corresponding temperatures. For maintaining the bottom plate temperature constant, the LabVIEW code computes the average temperature of the bottom copper plate. This acts as a process variable for the LabVIEW code. The PID VI compares the setpoint(SP or the desired temperature) with the process variable (PV). Based on the difference between SP and PV, i.e., error(e), the PID provides an output voltage which is fed to the DC programmable power supply (Scientific-DCX160M10) that provides

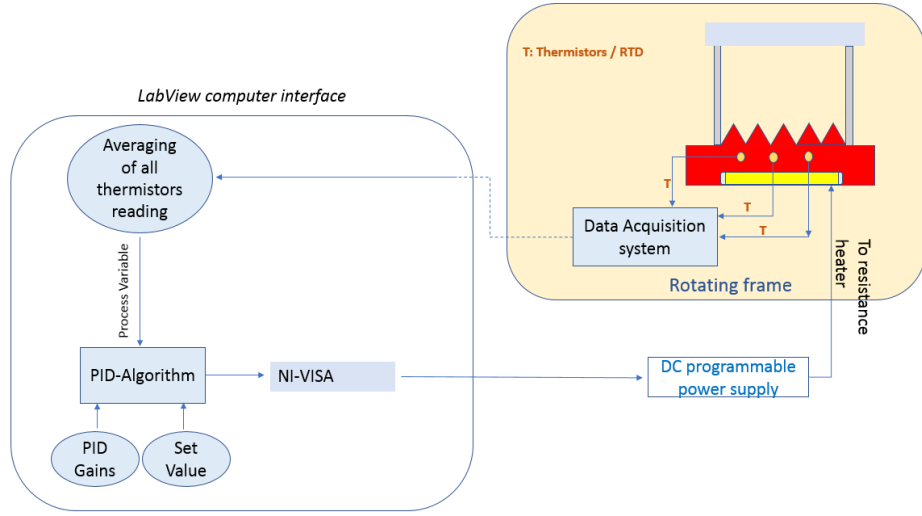


Figure 2.11: Flowchart of PID controller designed on LabVIEW.

appropriate voltage across the resistance heater.

$$u(t) = K_c \left( e + \frac{1}{T_i} \int_0^t e dt + T_d \frac{de}{dt} \right) \quad (2.3)$$

The general equation of PID algorithm is shown in Eqn. 2.3 [47, 48, 49]. The *proportional term* ( $K_c e$ ) is proportional to the instantaneous error ( $e$ ). Setting the proportional constant ( $K_c$ ) too high can result in an oscillating system. The second term  $\frac{1}{T_i} \int_0^t e dt$  is the integral term. It gives output based on the accumulated error. Lastly the derivative term  $T_d \frac{de}{dt}$  acts on the rate of change of the instantaneous error. The derivative term prevents overshooting in the system. The accuracy with which the controller maintains the desired temperature depends on the PID constants.

## 2.3 Nusselt number measurements

To characterize the convective motion, we measure the heat-flux in the rough RBC cell. The measurement was made on square RBC cell ( $\Gamma \approx 1$ ) with both top/bottom boundaries being rough. The working experimental setup is shown in Fig 2.12. The heat transport in the cell is characterized by Nusselt number ( $Nu$ ), defined as  $Nu = qH/\lambda\Delta$ , where  $q$  is the time averaged heat flux supplied to the bottom plate,  $H$  is the height of the cell,  $\Delta$  is the difference between the top plate temperature ( $T_t$ ) and the bottom plate temperature ( $T_b$ ) and  $\lambda$  is the

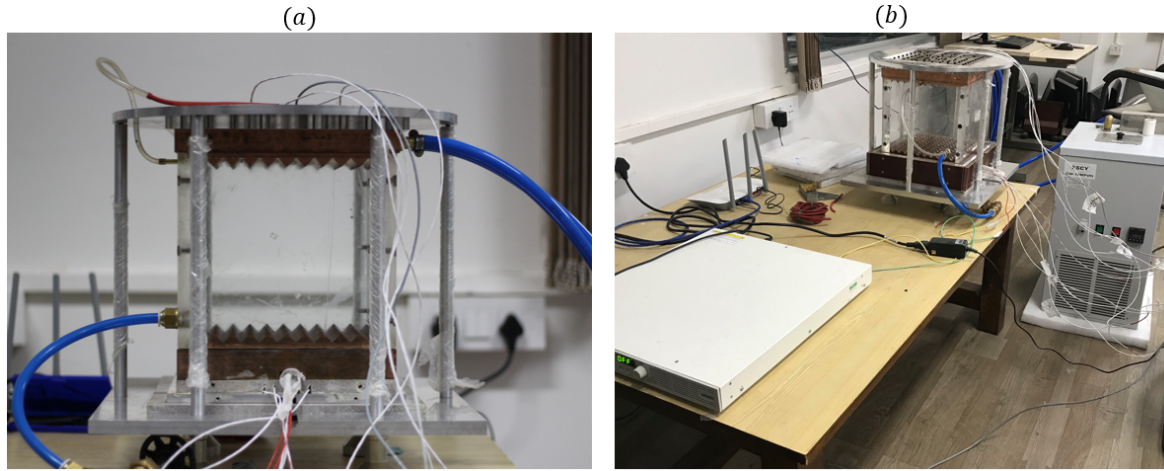


Figure 2.12: (a) RBC cell for Nusselt number measurements and (b) non-rotating experiment setup.

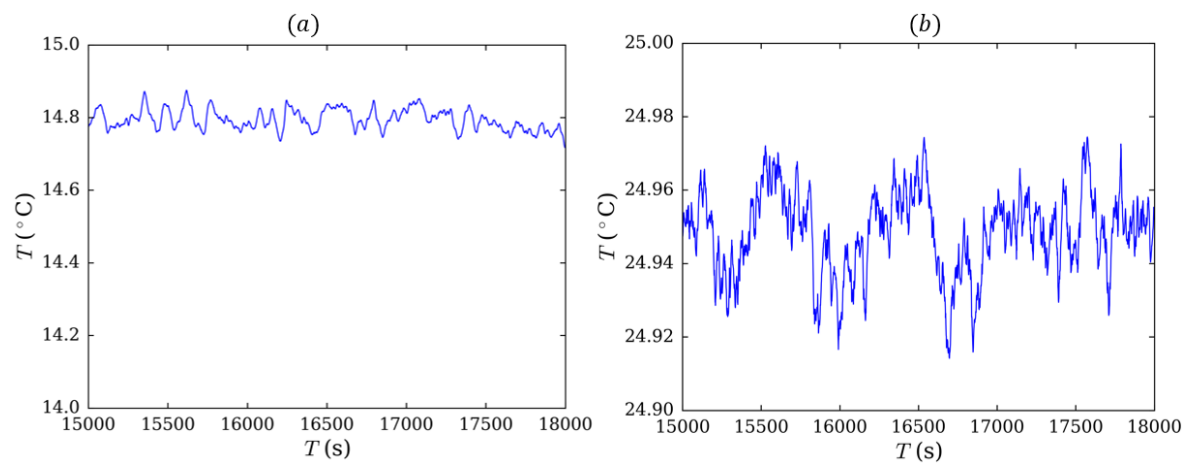


Figure 2.13: Figure showing variation of the temperature of the top and bottom copper plates with time.

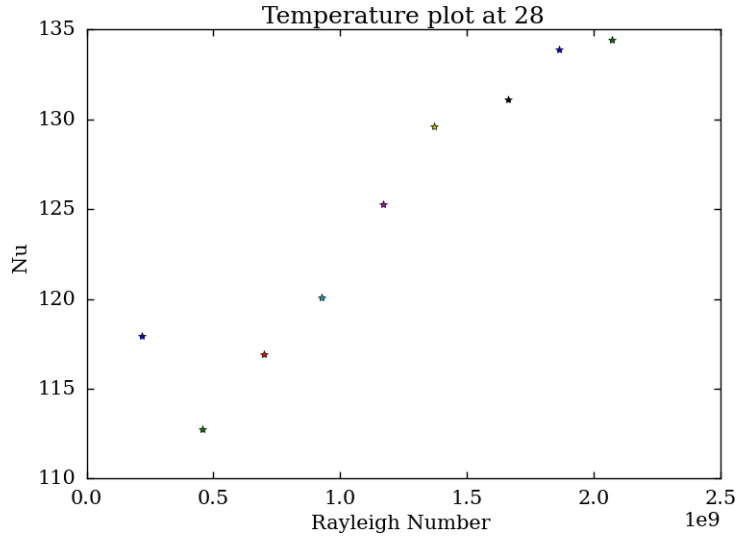


Figure 2.14: Nusselt vs Rayleigh number graph for non-rotating convection with both walls rough and working fluid as water.

Table 2.1: Experimental results of non-rotating Nusselt number measurements (with both rough plates).

Nu	$Ra$	$\Delta T$ (°C)	$\delta_t$ (mm)	$q$ (W/m <sup>2</sup> )
117.9	$2.16 \times 10^8$	1.91	0.84	678.5
112.7	$4.54 \times 10^8$	4.02	0.88	1363.0
116.9	$6.99 \times 10^8$	6.20	0.85	2175.0
120.0	$9.24 \times 10^8$	8.19	0.83	2951.7
125.2	$1.16 \times 10^9$	10.35	0.79	3892.5
129.6	$1.36 \times 10^9$	12.13	0.77	4716.9
131.0	$1.66 \times 10^9$	14.71	0.76	5787.7
133.9	$1.86 \times 10^9$	16.51	0.746	6635.3
134.4	$2.07 \times 10^9$	18.33	0.743	7395.9

thermal conductivity of the fluid. The bottom and top copper plate temperatures are varied for each dataset while keeping the mean temperature  $((T_b + T_t)/2)$  of the cell fixed at 20°C. All fluid properties in the calculations are considered at this mean temperature. Resistances of thermistors/RTD resistances are recorded every second(sampling rate 1 Hz). For any given data point, measurements over the first 6 hrs were discarded to avoid transients, while those recorded over the next six hours were averaged to calculate heat flux ( $q$ ),  $T_b$ , and  $T_t$ . The temperature-time series for the top and bottom copper plate are shown in Fig. 2.13. Our experimental data is shown in the Fig 2.14 and Table 2.1. It follows from Table 2.1 that with increasing Rayleigh number, the boundary layer thickness ( $\delta_t$ ) decreases. As the ratio  $k/\delta_t$  increases the Nusselt number also increases due to enhanced plume emissions into the bulk .This establishes our experimental protocol and will allow us to make further measurements. To calculate scaling exponent we need more experimental data points, which could not be performed because of COVID-19 pandemic situation.

## Chapter 3

# Numerical study on rotating convection with rotation vector perpendicular to gravity

### 3.1 Introduction

Helicity plays an important role in the generation of the magnetic field in planets, stars, and other celestial objects [12, 50, 51, 52, 53]. Helicity, or helicity density [54], is defined as  $h = \mathbf{u} \cdot \boldsymbol{\omega}$ , where  $\mathbf{u}$  is velocity and  $\boldsymbol{\omega} = \nabla \times \mathbf{u}$  is vorticity. The Earth's core is a complex system where several forces interact – buoyancy force due to thermal and compositional gradients, Lorentz force due to the magnetic field, and Coriolis force due to the rapid rotation. The presence of helicity in the flow leads to a "lift and twist" mechanism of field generation, also called the  $\alpha$ -effect [50, 55]. The  $\alpha^2$ -dynamo model, in which the  $\alpha$ -effect acts twice, predicts Earth-like dipolar magnetic field, but it relies on the sign of helicity being negative in the north and positive in the south [56, 57]. Indeed, this segregation of helicity outside the tangent cylinder is a robust feature of most dynamo simulations [9, 10, 56, 58, 59, 60]; for instance

---

<sup>0</sup>This chapter is adopted from Abhilash Ojha, Mohammad Anas, Avishek Ranjan, Pranav Joshi, and Mahendra K. Verma, "Helicity segregation by Ekman pumping in rotating flows with gravity orthogonal to rotation", under review.

see Fig. 3.1, which contains helicity plots generated by [9, 10]. However, the mechanisms of helicity generation and segregation in these dynamo simulations remain unclear and debated.

Possible mechanisms of helicity generation in dynamos were first proposed by Busse [61, 62], who suggested three sources: (a) spatial variations in the Lorentz forces, (b)  $\beta$  effect due to the curvature of the spherical shell, and (c) Ekman pumping near the boundaries. Though the Lorentz force may lead to local intensification or reduction in helicity [59, 60], it is unlikely to create the observed segregation since the same is observed in non-magnetic rotating convection simulations as well [10, 56, 63]. Similarly, the  $\beta$  effect [58, 64, 65, 66] can also lead to additional negative helicity in the north and positive helicity in the south due to the conservation of angular momentum, but is unlikely to cause it. Ekman pumping arises from mass conservation and an imbalance between the pressure forces and Coriolis forces near boundaries with non-zero wall shear stress. This can lead to the generation as well as segregation of negative (positive) helicity in the north (south) of the equator. However, in the Earth's core, where  $Ta \sim 10^{27}$  [67], Ekman pumping is considered to be relatively unimportant [68] ( $Ta$  is the Taylor number – the square of the ratio of Coriolis force to the viscous force). However, most simulations are still far from the core parameter regime and are too viscous, with the closest ones at  $Ta \sim 10^{14}$  [9]. In simulations with lower values of  $Ta$ , it is a matter of debate whether the helicity indeed arises due to Ekman pumping or not. For instance, in spherical magnetoconvection simulations performed at  $Ta = 4.4 \times 10^7$  and  $Ra = 3.1 \times 10^5$ , Olson et al. [56] did observe helicity segregation, but noted that Ekman pumping was unlikely to be important as the peak  $|h|$  was far from the boundaries. Here,  $Ra$  denotes the Rayleigh number that represents the strength of buoyancy forces over viscous and thermal diffusion. In yet another simulation at  $Ta = 4 \times 10^8$  and  $Ra = 7.5 \times 10^6$  from the same study, the helicity signs were observed to be reversed in the Ekman layer, while remaining unchanged in the bulk. They also hinted at the possible role of buoyancy in helicity generation and segregation. Recently, it was shown that the helicity source due to buoyancy was indeed positively correlated with the helicity itself in moderately-forced dynamo simulations [10]. The authors speculated on the possible role of inertial waves [69, 70] and their interplay with buoyancy forces.

Schaeffer et al. [9] reported dynamo simulations performed at some of the extreme parame-

ter regimes that are computationally feasible with modern computing resources. Azimuthally-averaged and time-averaged helicity plots for two of their numerical dynamos are shown in Fig. 3.1(a): S2 ( $Ta = 4 \times 10^{14}$ ,  $Ra = 2.5 \times 10^{12}$ ) and, (b): S0 ( $Ta = 4 \times 10^{10}$ ,  $Ra = 6.3 \times 10^9$ ). In both the cases, there is a clear segregation of helicity, but the locations of the peak  $|h|$  are different. For S2, the peak  $|h|$  is in the interior (or far from boundaries) whereas for S0, the peak is closer to the boundaries. Schaeffer et al. [9] suggest that helicity in S0 comes most likely from Ekman pumping at the boundaries, whereas in S2 the primary source is different. However, the peak  $|h|$  closer to the Ekman boundary layer observed in S0 may be contrasted with the helicity distribution in the Case 1 simulation considered by Olson et al. [56] which has 100 times lower  $Ta$ . The ratio  $Ra/Ta$ , however, for the run S2 of Schaeffer et al. [9] and for Case 1 in Olson et al. [56] is approximately the same ( $\sim 0.006 - 0.007$ ). Recall that for both these simulations, the peak  $|h|$  lies in the interior, unlike S0 for which  $Ra/Ta \sim 0.16$ . This indicates that perhaps it is the relative strengths of the buoyancy and the Coriolis forces that dictate the helicity distribution. Also, it remains unclear if helicity generation by Ekman pumping can be influenced by the presence of buoyancy force. This is harder to predict for the regions near the equator where gravity and rotation vector are orthogonal. The role of boundary conditions also remains unclear, since the same sign of helicity is observed even for the free-slip boundary condition for which Ekman pumping is absent [58, 64, 71, 72]. Moreover, some researchers (for e.g., Olson et al. [56], [59]) observed the helicity magnitudes to be reduced when they adopted free-slip boundary condition.

In this study, we investigate the helicity generation and segregation due to Ekman pumping. We choose a configuration inspired by the equatorial regions of the core – a Cartesian box with rotation axis perpendicular to gravity. This non-classical configuration has not been studied in detail, but has been of interest lately [69, 70, 73, 74]. Moreover, helicity segregation due to the secondary flows predicted by Busse [62] and Olson et al. [56] has not been investigated and demonstrated, to our knowledge. Our simulation domain, the Cartesian box is shown in Fig. 3.2(a) for which gravity points along  $-z$  and rotation along  $-x$ ; this may be qualitatively compared with a square shown by yellow dashed lines in Fig. 3.1(c). We also examine the effect of boundary conditions using both no-slip and constant stress (with non-zero velocity) boundary conditions on the walls normal to the rotation axis ( $yz$ -planes).

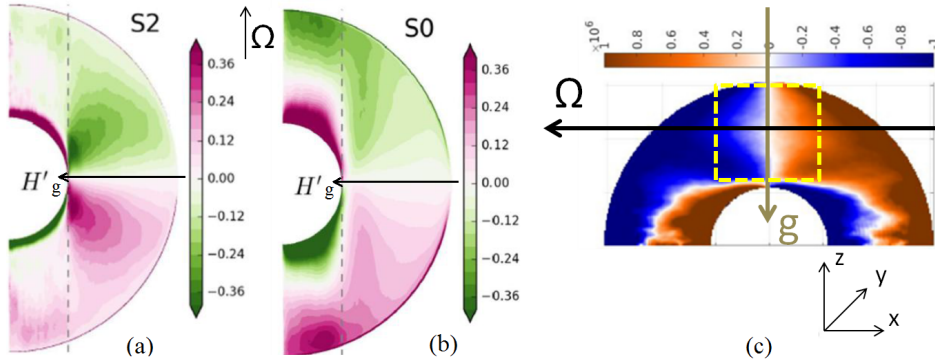


Figure 3.1: (a), (b)  $\phi, t$ -averaged helicity calculated using the fluctuating components of velocity and vorticity from [9]. Note that Taylor number ( $Ta$ ) for S0 and S2 are  $4 \times 10^{10}$  and  $4 \times 10^{14}$ , respectively. (c) Rotated image of  $\phi, t$ -averaged helicity from [10] along with a Cartesian box shown in yellow near the equator, as a motivation for our simulation domain. Images are used with the permission of the authors.

We also conduct modal analysis to quantify the importance of secondary flows with respect to the bulk flow, and present the force balance inside and outside the Ekman layers.

## 3.2 Simulation Details

We use the finite difference code, SARAS [75, 76], which solves the incompressible Navier-Stokes equations on a staggered grid and uses a multigrid solver for the pressure Poisson equation. We have validated SARAS for Rayleigh-Bénard Convection (RBC) against the results of Wagner and Shishkina [77] for  $Pr = 0.786$ . Moreover, SARAS has also proven to be robust in simulating RBC for a wide range of  $Ra$ , and  $Pr$  [78]. We use SARAS to simulate a Cartesian box of unit length along each direction, i.e.,  $L_x = L_y = L_z = 1$ . Figure 3.2 shows a schematic diagram of the problem. Note that the rotation vector is along  $-\hat{\mathbf{e}}_x$ , normal to the gravity, which acts along  $-\hat{\mathbf{e}}_z$ ; here,  $\hat{\mathbf{e}}_x$  and  $\hat{\mathbf{e}}_z$  are unit vectors along  $x$  and  $z$  directions respectively. We solve the following equations for rotating Rayleigh-Bénard Convection under the Boussinesq approximation [12]:

$$\frac{\partial \mathbf{u}}{\partial t} + (\mathbf{u} \cdot \nabla) \mathbf{u} = -\nabla P + \left( \sqrt{\frac{Pr}{Ra}} \right) \nabla^2 \mathbf{u} + T \hat{\mathbf{e}}_z + \left( \sqrt{\frac{Ta Pr}{Ra}} \right) \hat{\mathbf{e}}_x \times \mathbf{u}, \quad (3.1)$$

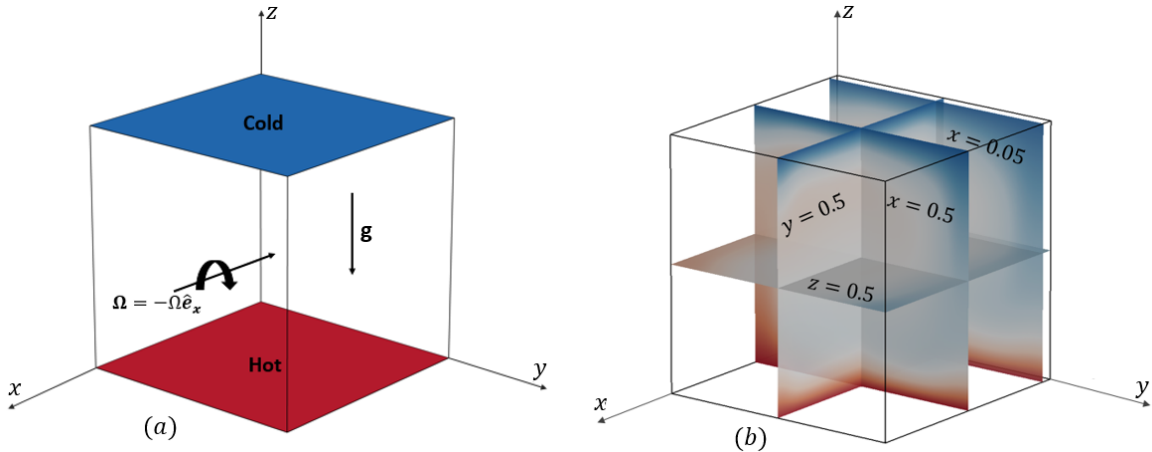


Figure 3.2: (a) Schematic diagram of the model for our simulations, (b) Location of various planes in the domain.

$$\frac{\partial T}{\partial t} + (\mathbf{u} \cdot \nabla) T = \frac{1}{\sqrt{(RaPr)}} \nabla^2 T, \quad (3.2)$$

$$\nabla \cdot \mathbf{u} = 0. \quad (3.3)$$

Here,  $\mathbf{u}$  is the velocity field,  $T$  is the temperature field, and  $P$  is the pressure field. The above equations have been non-dimensionalized using the free-fall velocity,  $U = \sqrt{\beta g \Delta T L}$ , as the velocity scale,  $\Delta = T_h - T_c$  as the temperature scale, and size of the domain  $L$  (in each direction) as the length scale; here,  $T_h$  and  $T_c$  are the temperatures of the hot and cold plates respectively. The non-dimensionalized parameters are Rayleigh number  $Ra = g \beta \Delta T L^3 / \nu \kappa$ , Prandtl number  $Pr = \nu / \kappa$ , and Taylor number  $Ta = 4\Omega^2 L^4 / \nu^2$ . Here,  $\nu$  is the kinematic viscosity,  $\beta$  is the thermal expansion coefficient,  $g$  is gravitational acceleration,  $\mathbf{\Omega} = -\Omega \hat{\mathbf{e}}_x$  is the angular velocity, and  $\kappa$  is the thermal diffusivity of the fluid.

We perform four simulations, denoted as RH (rotating hydrodynamics with no-slip boundary condition), RC1 and RC2 (rotating convection with no-slip boundary condition), and RCS (rotating convection with constant stress boundary condition). All simulations are performed at a fixed Rayleigh number  $Ra = 10^5$  (except RH), and Prandtl number  $Pr = 1$ . For RC1 and RC2,  $Ta = 10^5$  and  $10^6$ , respectively (see Table 3.1). Rossby number is defined as  $Ro = \sqrt{Ra/(TaPr)}$  (for RH,  $Ro = V_{rms}/2\Omega L$ , where  $V_{rms}$  is the room-mean square velocity). These parameters were chosen so that  $Ro$  is comparable to those in the spherical

Table 3.1: Simulation details:  $N$  is the number of grid points in each direction and  $Pr = 1$  for all the runs. For RCS, no-slip boundary conditions are imposed at all the walls except  $x = 0$  and  $x = 1$ .

Runs	$N$	$Ra$	$Ta$	$Ro$	Boundary Conditions
RC1	128	$10^5$	$10^5$	1.0	no-slip at all walls
RC2	128	$10^5$	$10^6$	0.316	no-slip at all walls
RH	128	—	$10^6$	0.077	no-slip at all walls
RCS	128	$10^5$	$10^6$	0.316	constant stress at $x = 0$ and 1

dynamo simulations discussed earlier ( $Ro$  for the simulation S0 in [9] is 0.4). The parameters for the simulation RH are similar to those for RC2, except that we switch off the buoyancy force for RH. Moreover, we employ dead state ( $\mathbf{u} = 0$  and linear variation in  $T$  along the direction of gravity) as the initial condition for all the simulations except RH, in which we use the steady-state velocity field of RC2 as the initial condition. We start the simulation RH at  $t = 490$  and wait till the signature of buoyancy in the velocity field almost fades away at  $t = 496$ . We use the velocity field at  $t = 496$  of RH for our analysis. For RCS, we again use the same parameters as in RC2, except that we employ constant shear stress at the boundaries normal to the rotation axis (i.e., at  $x = 0, 1$ ). The value of the non-dimensional shear stress is set to +3 at  $x = 0$  (where  $\partial V_y / \partial x = 3$  and  $\partial V_z / \partial x = 0$ ), and -3 at  $x = 1$  (where  $\partial V_y / \partial x = -3$ ,  $\partial V_z / \partial x = 0$ ). These values are inspired by the dimensionless shear stress values in the geodynamo simulation S1 of Ranjan et al. [10].

### 3.3 Results and Discussions

We now present and analyze the results obtained from our simulations. We report the results for laminar, steady-state flow, i.e., when the field variables are not varying with time (except for RH, which is a decaying rotating flow). We also ensured that our results are independent of grid size by running the same cases at a higher resolution of  $N = 256$  (see Fig. B.3 in Appendix B.2).

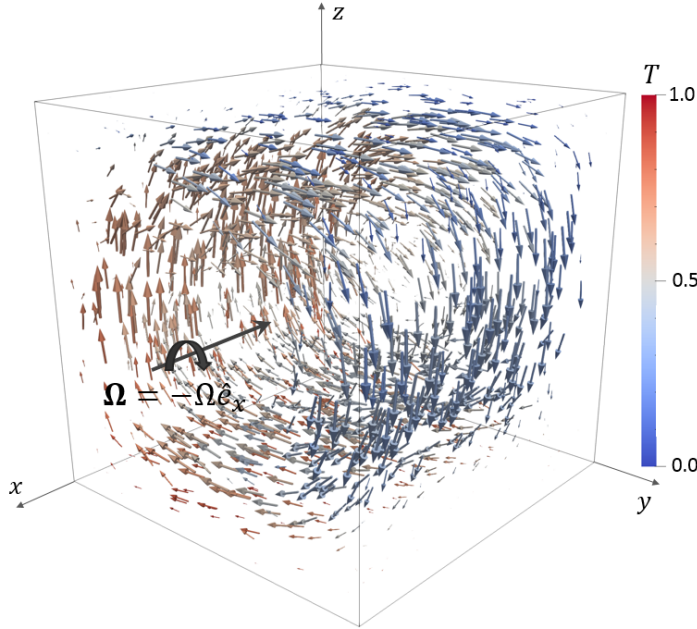


Figure 3.3: Three-dimensional velocity vector field (colored with temperature) for RC2 showing dominance of cyclonic flow structure.

Figure 3.3 shows the three-dimensional velocity vectors colored with temperature values for the run RC2. Here we observe a distinct cyclonic flow structure, which is typical in all our simulations. We notice the hot fluid rising and the cold fluid sinking in such a way that it forms a cyclonic structure of length scale comparable to the domain size. Such a dominant cyclonic flow has also been observed in earlier studies [64, 65].

### 3.3.1 Plane averaged helicity

To identify the components of velocity and vorticity responsible for helicity generation and segregation, we analyze the three constituents of helicity,  $V_x \omega_x$ ,  $V_y \omega_y$ , and  $V_z \omega_z$ . Figure 3.4 shows the variation of these helicity constituents and the total helicity ( $\mathbf{u} \cdot \boldsymbol{\omega}$ ) along the  $x$ -axis for all the four simulations. Note that these constituents and the total helicity are normalized by the maximum possible helicity  $|\mathbf{u}| |\boldsymbol{\omega}|$  at each point in the domain, and then averaged in the  $yz$ -plane. We observe a clear segregation of helicity in the flow – negative near the wall with outward normal parallel to the rotation vector (near  $x = 0$ ), and positive near the wall with outward normal anti-parallel to the rotation vector (near  $x = 1$ ). This corresponds to a

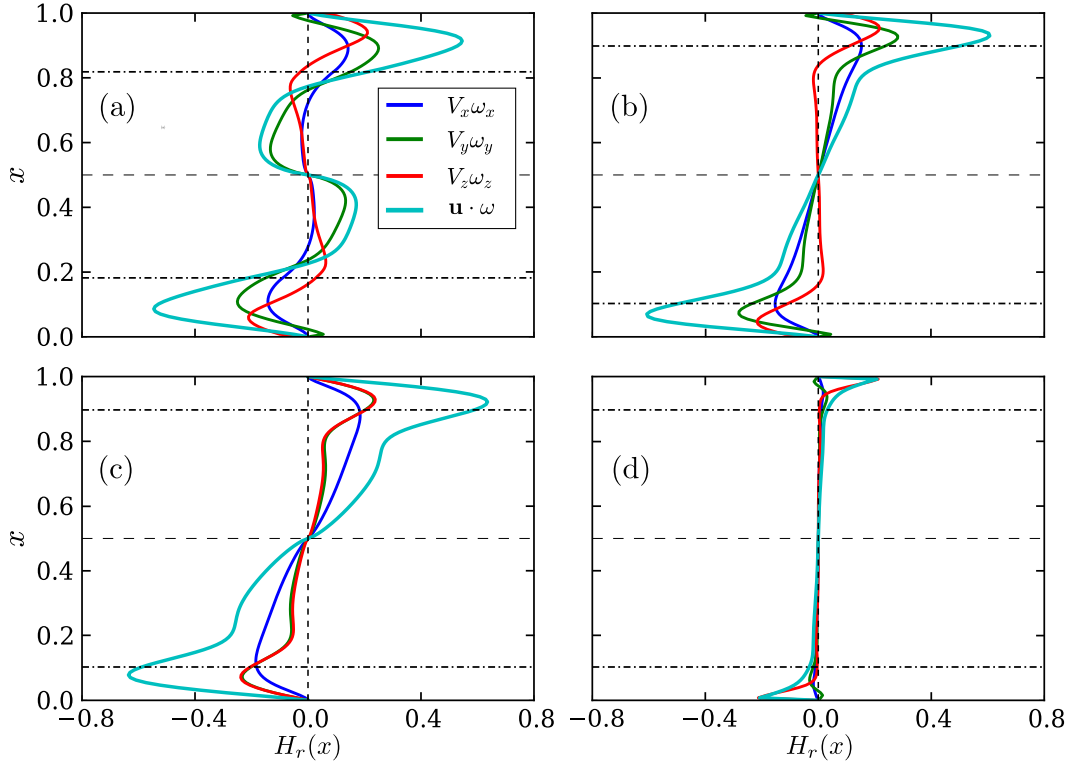


Figure 3.4: Variation of the constituents of helicity normalized by the maximum possible helicity  $|\mathbf{u}||\boldsymbol{\omega}|$  and averaged in the  $yz$ -plane ( $H_r$ ) with  $x$  for (a) RC1, (b) RC2, (c) RH, and (d) RCS. Horizontal dot-dashed lines represent the Ekman boundary layer thickness  $\delta_E \approx 2.284\sqrt{\nu/\Omega}$  [11].

negative (positive) helicity in the north (south), as seen in the spherical dynamo simulations results shown in Fig. 3.1. Note that all the constituents of helicity are contributing to the helicity segregation in the flow. Moreover, the helicity peak lies inside the Ekman boundary layer (the approximate Ekman layer thickness is indicated in the figure). This observation points towards helicity generation inside the Ekman layer.

It is interesting to observe that for RC1 and RC2 the peaks of  $V_x \omega_x$  and  $V_y \omega_y$  are farther from the boundaries as compared to those of  $V_z \omega_z$ . RC1 exhibits an interesting distribution of helicity outside the Ekman layer – the average helicity is opposite to that near the walls. Note that the Coriolis force is weaker in RC1 (at  $Ro = 1$ ) as compared to RC2 ( $Ro \approx 0.3$ ). As expected from the Taylor-Proudman theorem, stronger rotation leads to smaller flow

variations along the rotation axis. This indicates that with stronger rotation (larger  $Ta$ , smaller  $Ro$ ), variations in helicity also diminish along the rotation axis. We can also infer that the buoyancy force gives rise to an asymmetry between  $V_y\omega_y$  and  $V_z\omega_z$ . Since buoyancy is absent in RH,  $V_y\omega_y$  and  $V_z\omega_z$  overlap each other. It is not surprising that the effect of buoyancy is observed mainly on  $V_z\omega_z$ , since gravity points along  $-z$ , but its effect on the helicity in the bulk is notable (compare Fig. 3.4 (b) with (c)). We also observe the expected helicity segregation in RCS, where a constant stress is applied at the walls with wall-normal parallel to the rotation axis, but the helicity is mostly concentrated close to the boundary and also the peak magnitudes are very small.

### 3.3.2 Helicity at different planes

We now use the plots of velocity and vorticity fields on different planes to further examine and explain the cause of helicity segregation. For the convenience of the readers, the locations of these planes are shown in Fig. 3.2(b). Figure 3.5 shows the contour plots of  $V_x$ ,  $\omega_x$ , and  $V_x\omega_x$ , normalized by  $V_{rms}$ ,  $\omega_{rms}$ , and  $V_{rms}\omega_{rms}$  respectively, on the  $yz$ -plane at  $x = 0.05$  (inside the Ekman layer).  $V_{rms}$  and  $\omega_{rms}$  are the root-mean square ( $rms$ ) values of the velocity and vorticity fields, respectively. The color plots are superimposed with velocity vectors denoted by arrows. Recall that the rotation vector (along  $-\hat{\mathbf{e}}_x$ ) points into the plane. For RC1, RC2 and RH, we see that  $V_x$  is positive in the centre of the plane, showing that fluid near the boundary is moving towards the bulk due to Ekman pumping (see the first column of Fig. 3.5). Accordingly,  $V_x$  near the side walls is negative due to the flow continuity. We also observe a dominant cyclonic flow structure, clearly visible in the region with negative  $\omega_x$ , outside the viscous boundary layers formed over the walls parallel to the rotation axis, for all the runs (see the second column of Fig. 3.5). The positive values of  $\omega_x$  (anticyclonic flow) observed close to the boundaries (perpendicular to the  $y$  and  $z$  axes) are due to the shear within the hydrodynamic boundary layer.  $V_x$  is directed into the domain at the walls perpendicular to the rotation axis (positive near  $x = 0$  and negative near  $x = 1$  walls), whereas  $\omega_x$  points along  $-x$  all along the rotation axis due to the cyclonic flow. As a result, we obtain negative helicity at  $x = 0.05$  (see third column of Fig. 3.5), and positive helicity at  $x = 0.95$  (not shown here). For the case RH, both the velocity and vorticity magnitudes

peak at the centre and flow is perfectly symmetric, unlike that in RC1 and RC2 where  $V_x$  and  $\omega_x$  peak away from the centre, and so the regions of high helicity in RC1 and RC2 are also shifted away from the rotation axis.

Figure 3.6 shows similar quantities as in Fig. 3.5, plotted in the plane parallel to the rotation axis and gravity, i.e. the  $xz$ -plane, at  $y = 0.5$ . The vector plots in the runs RC1, RC2, and RH exhibit secondary rolls which are a clear signature of Ekman pumping (we use secondary flow structures and secondary rolls interchangeably in this paper). A zoomed view of the pair of secondary rolls is shown in the subsequent figure, Fig. 3.7. These rolls, present in the outer part of the Ekman boundary layer, pump the fluid away from the Ekman boundary layer towards the bulk. However, we notice a subtle difference between the rolls of RC2 and RH. In RH, the fluid pumped from the Ekman boundary layer into the bulk is mostly concentrated close to the rotation axis, whereas, for RC2, it is more widely distributed. The secondary rolls also generate vorticity of opposite sign near the boundary (see the second column of Fig. 3.6). The cyclonic flow and Ekman pumping provide  $V_y$  and  $\omega_y$ , respectively, in such a way that their product exhibits negative (positive) helicity near  $x = 0$  ( $x = 1$ ) wall (see the third column). Again, the regions of high  $V_y\omega_y$  in RC1 and RC2 are located farther from the rotation axis. Due to the effect of buoyancy (note that gravity acts along  $-z$ ), RC1 shows a region of weak  $\omega_y$  of opposite sign outside the Ekman layer and close to the thermal walls. This explains the opposite helicity in the bulk regions of the flow for RC1 seen in Figs. 3.4 and 3.6.

Figure 3.8 shows contour plots in the  $xy$ -plane at  $z = 0.5$ , parallel to the rotation axis, perpendicular to gravity. Once again, we notice the signature of Ekman pumping as expected, though it is not as distinct as in Figs. 3.5 and 3.6 for RC1 and RC2. We speculate that this is due to the effect of buoyancy force. Recall that buoyancy also causes asymmetry between  $V_y\omega_y$  and  $V_z\omega_z$  (see Fig. 3.4(b)). In the absence of buoyancy force for the run RH, the symmetry is established;  $V_y\omega_y$  and  $V_z\omega_z$  overlap each other, and the plots at  $y = 0.5$  and  $z = 0.5$  planes become similar (see Fig. 3.4(c), and third row of Fig. 3.6 and Fig. 3.8). Similar to Fig. 3.6, here the cyclonic flow and Ekman pumping provide  $V_z$  and  $\omega_z$  respectively, in such a way that their product exhibits negative (positive) helicity near  $x = 0$  ( $x = 1$ ) wall.

In both Figs. 3.6 and 3.8, the sign of the vorticity components can also be understood

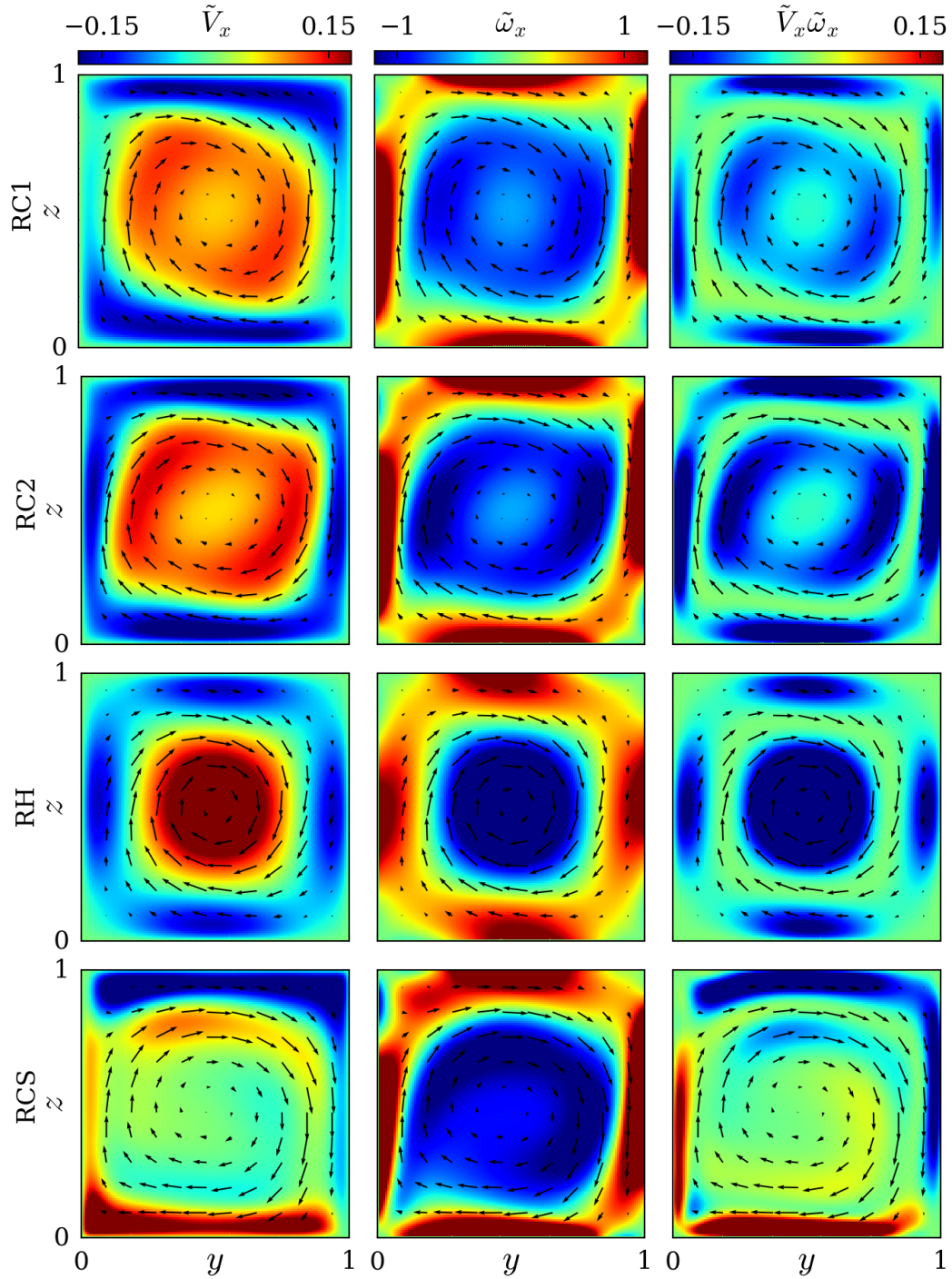


Figure 3.5: Contour plots of normalized (by their rms values)  $V_x$ ,  $\omega_x$ , and  $V_x\omega_x$  (from left to right) superimposed with velocity vectors in  $yz$ -plane at  $x = 0.05$  for RC1 (first row), RC2 (second row), RH (third row), RCS (fourth row).

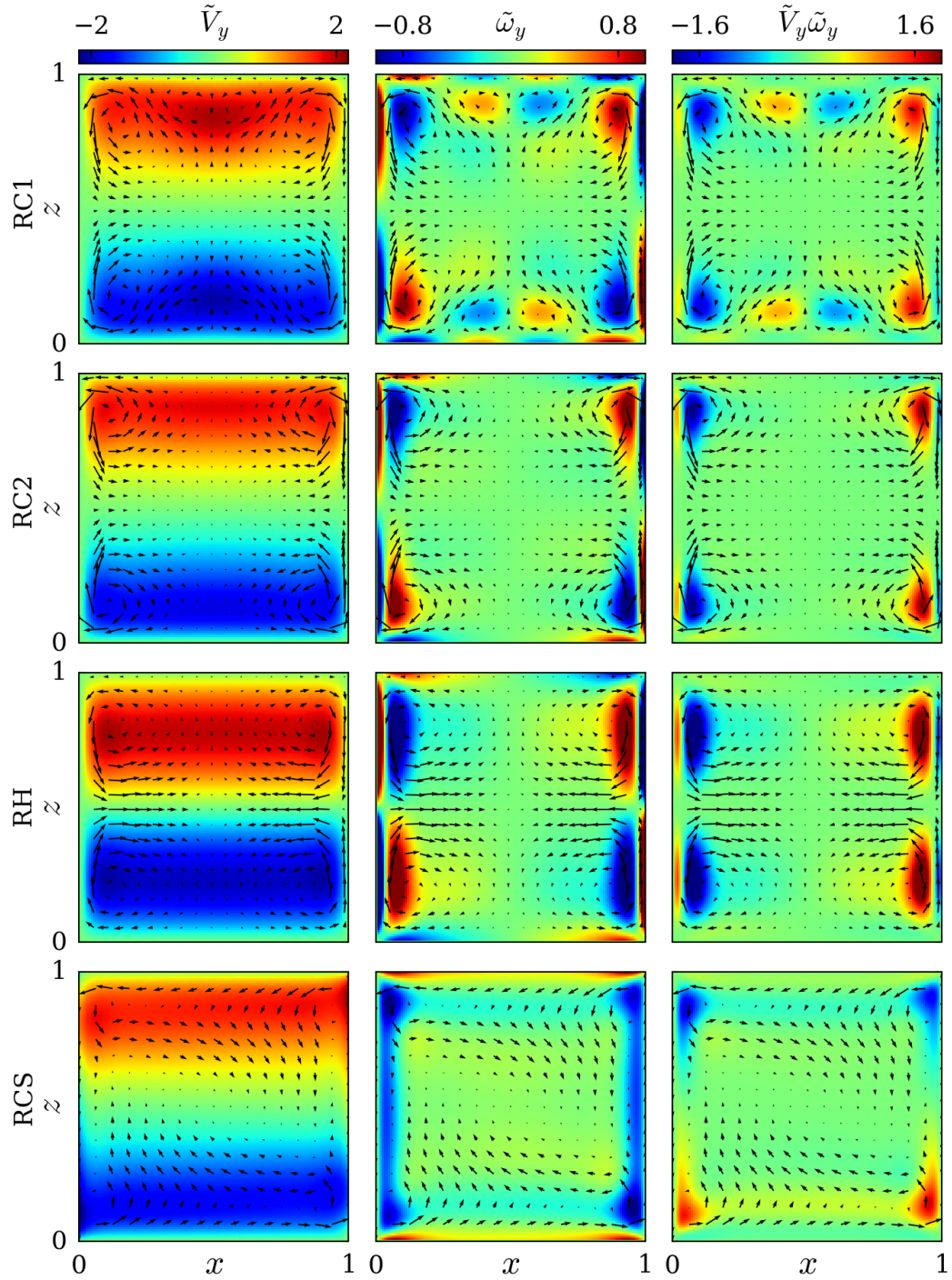


Figure 3.6: Contour plots of normalized (by their rms values)  $V_y$ ,  $\omega_y$ , and  $V_y\omega_y$  (from left to right) superimposed with velocity vectors in  $xz$ -plane at  $y = 0.5$  for RC1 (first row), RC2 (second row), RH (third row), RCS (fourth row).

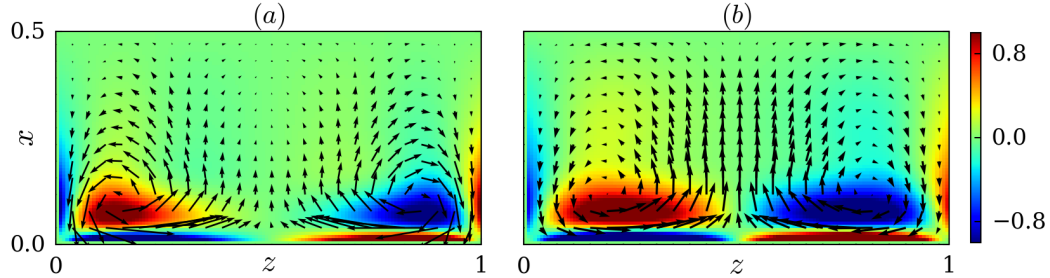


Figure 3.7: Contour plot of normalized (by their rms value)  $\omega_y$  superimposed with velocity vectors in  $xz$ -plane at  $y = 0.5$  for the run (a) RC2 and (b) RH. Signature of Ekman pumping is evident. Note in this figure that the vertical axis is along  $x$  and horizontal along  $z$ .

by considering the velocity gradients along  $x$  and invoking the Taylor-Proudman theorem ( $\partial \mathbf{u} / \partial x \approx 0$ ). That is, we can consider  $\partial V_z / \partial x$  (inferred from the first column of Fig. 3.8) to understand the distribution of  $\omega_y$  (second column of Fig. 3.6). Similarly,  $\partial V_y / \partial x$  (inferred from the first column of Fig. 3.6) can be considered for  $\omega_z$  (second column of Fig. 3.8). As the rotation becomes stronger, as is the case for RC2, both these gradients become smaller and so do the vorticity components in the interior, thus leading to the same sign of helicity in the entire one-half of the box. Thus, we remark that the combined effect of Ekman pumping and the cyclonic flow is responsible for the helicity segregation in our simulations. For the anti-cyclones, which rotate opposite to the global rotation, the direction of Ekman pumping is reversed – the flow is towards the wall, also called Ekman suction [79]. Therefore, the same signs of helicity can be expected in anti-cyclones as well. In all the three figures, Figs. 3.5, 3.6 and 3.8, the plots for RCS are markedly different from those for RC1, RC2 and RH. For example, compare  $V_x$  in Fig. 3.5 and  $\omega_y, \omega_z$  in Figs. 3.6 and 3.8. This indicates the importance of the boundary conditions and the presence of shear in different directions. To further reinforce this point, we also performed a simulation at the same parameters as in RC2, but with free-slip boundary conditions on the walls at  $x = 0$  and  $x = 1$ . The helicity plots for this simulation (included in Appendix B.1) show no helicity generation near the boundaries, as expected. In RCS, the constant stress applied at the boundaries disrupts the secondary flows due to Ekman pumping (see Figs. 3.6 and 3.8), and as a result, the helicity values for RCS are reduced.

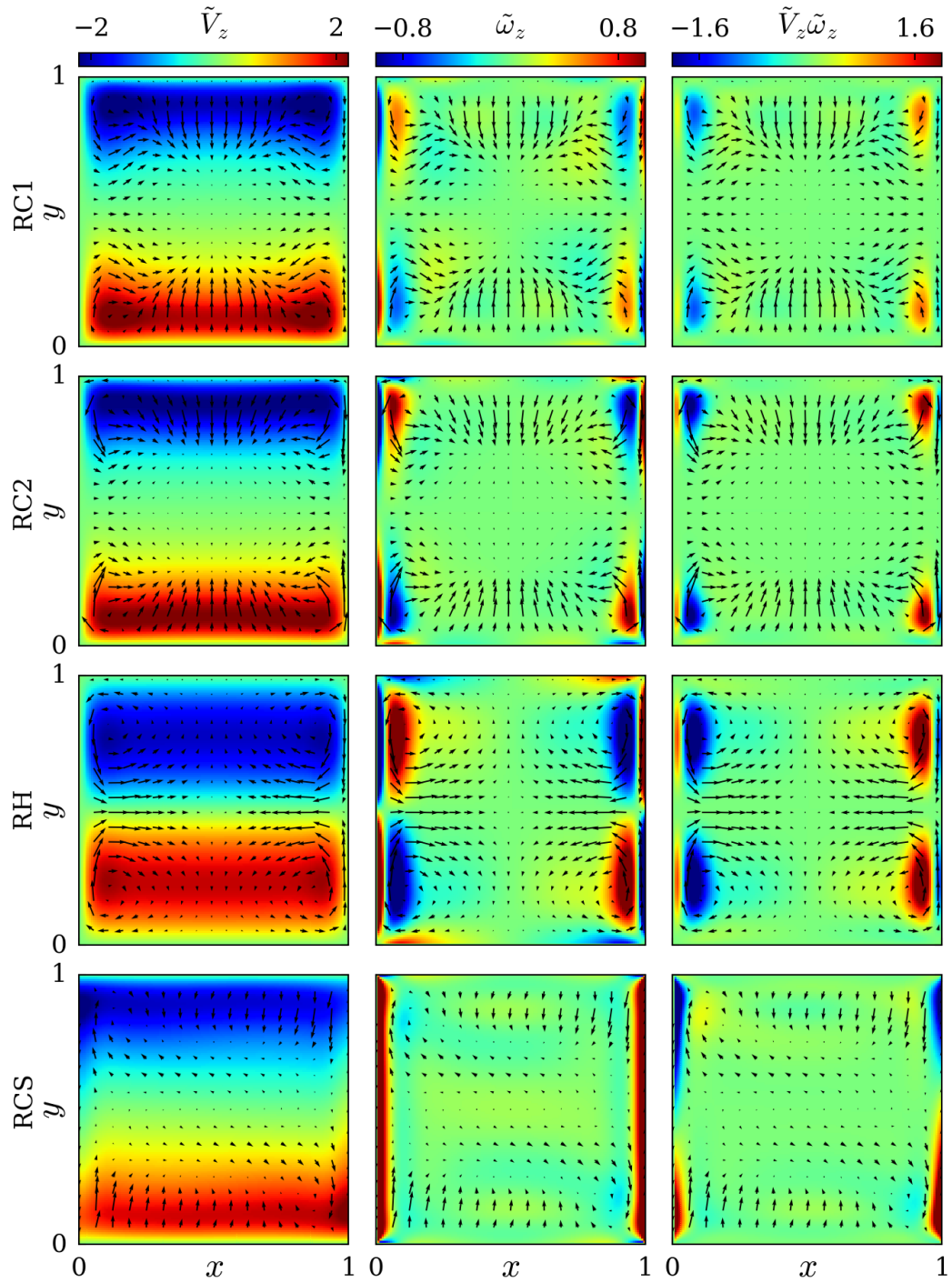


Figure 3.8: Contour plots of normalized (by their rms values)  $V_z$ ,  $\omega_z$ , and  $V_z\omega_z$  (from left to right) superimposed with velocity vectors in  $xy$ -plane at  $z = 0.5$  for RC1 (first row), RC2 (second row), RH (third row), RCS (fourth row).

Table 3.2: Modal energy of dominating modes in  $yz$ -plane at  $x = 0.5$  for RC1, RC2, RH, and RCS.

Modes	RC1 Energy %	RC2 Energy %	RH Energy %	RCS Energy %
(1, 1)	81.7	85.4	73.0	86.6
(1, 3)	5.00	1.50	10.9	2.70
(1, 5)	3.74	2.21	1.05	2.26
(3, 1)	0.01	0.11	10.8	0.51
(5, 1)	0.88	1.81	1.02	1.38

### 3.3.3 Modal energy analysis

In the previous sections, we showed that two flow structures dominate the flow – cyclones and secondary flows due to Ekman pumping. Now, in order to quantify their importance in the segregation of helicity, we analyze the energy contained in these flow structures using modal energy analysis. We expand the velocity fields in three planes  $x = 0.5$ ,  $y = 0.5$ , and  $z = 0.5$  using sine and cosine series. In the  $yz$ -plane at  $x = 0.5$ , the velocity field  $V_y$  and  $V_z$  are expanded as [80, 81]

$$V_y = \sum_{mn} \hat{C}_{mn} \sin(m\pi y) \cos(n\pi z), \quad V_z = \sum_{mn} \hat{D}_{mn} \cos(m\pi y) \sin(n\pi z), \quad (3.4)$$

where,  $\hat{C}_{mn}$  and  $\hat{D}_{mn}$  are the amplitudes of the velocity modes  $(m, n)$ . Similar expansion is used for the velocity fields in the other two planes. We compute the amplitudes  $\hat{C}_{mn}$  and  $\hat{D}_{mn}$  of the velocity modes  $(m, n)$  using the orthogonal properties of the given functions, and then obtain the percentage energy of that particular mode in that plane.

Tables 3.2, 3.3, and 3.4 show the percentage energy of the dominant structures in the flow at  $x = 0.5$ ,  $y = 0.5$ , and  $z = 0.5$  planes, respectively. In the  $yz$ -plane at  $x = 0.5$ , we clearly see that the  $(1, 1)$  mode, which represents the cyclonic flow structures, dominates for RC1 (81.7%), RC2 (85.4%), RH (73.0%) and RCS (86.6%). For the velocity field in the  $xz$ -plane at  $y = 0.5$ , we see that the  $(2, 2)$  mode, which represents the secondary rolls due to Ekman pumping, contributes a significant amount of energy in the simulations RC1 (39.3%), RC2 (22.8%) and RH (53.7%). The modes representing the cyclonic flow (i.e.,  $(1, 1)$ ) and Ekman

Table 3.3: Modal energy of dominating modes in  $xz$ -plane at  $y = 0.5$  for RC1, RC2, RH, and RCS.

Modes	RC1 Energy %	RC2 Energy %	RH Energy %	RCS Energy %
(0, 2)	0.59	1.49	0.58	15.1
(1, 3)	0.00	0.00	0.00	15.9
(2, 2)	39.3	22.8	53.7	0.11
(2, 4)	0.09	11.2	0.01	0.33
(3, 1)	0.00	0.00	0.00	14.5
(4, 2)	25.3	23.9	17.2	0.01
(4, 4)	17.5	6.30	0.04	0.09
(5, 1)	0.00	0.00	0.00	11.9
(6, 2)	1.72	11.4	7.23	0.06

Table 3.4: Modal energy of dominating modes in  $xy$ -plane at  $z = 0.5$  for RC1, RC2, RH, and RCS.

Modes	RC1 Energy %	RC2 Energy %	RH Energy %	RCS Energy %
(0, 2)	14.8	17.0	0.01	2.78
(0, 4)	21.2	30.2	0.05	23.6
(1, 3)	0.00	0.00	0.00	12.1
(2, 0)	27.5	12.3	10.4	0.05
(2, 2)	6.45	0.32	51.2	1.00
(2, 4)	5.54	2.99	0.01	0.17
(4, 0)	3.34	1.40	1.48	0.00
(4, 2)	4.75	7.18	18.8	0.23
(6, 2)	7.75	6.22	7.95	0.03

pumping (i.e., (2, 2)) together are responsible for the helicity generation and segregation in the flow, as discussed earlier. This is a novel result that has not been reported in the literature to the best of our knowledge. Note that in the  $xy$ -plane at  $z = 0.5$ , the mode (2, 2) does not contribute a significant amount of energy in the flow (for the case RC1 and RC2), most likely due to the presence of the buoyancy force. It is evident that in the run RH, the modal energy of the (2, 2) mode contributes significantly ( $> 50\%$ ) to the total energy in both  $xy$ - and  $xz$ -planes. In fact, the energy values of the (2, 2) mode in  $xz$ - and  $xy$ -planes for the run RH are not very different.

### 3.3.4 Force balance and helicity budget

We now analyze the force balance (for RC2 and RH) and the helicity budget (for RC1 and RC2) both inside and outside the Ekman layer. Figures 3.9 and 3.10 show the plots of the pressure gradient (including buoyancy force for RC2), Coriolis force, and viscous force at two  $yz$ -planes for RC2 and RH, respectively. The  $yz$ -plane in the first row (at  $x = 0.5$ ) is far from the Ekman layer, and that in the second row (at  $x = 0.05$ ) is inside the Ekman boundary layer. Vectors represent the respective force field directions, and the color represents the force magnitude. Note that the direction of the pressure gradient is towards the axis of rotation both inside and outside the Ekman layer, as would be expected for a cyclonic flow. Outside the Ekman layer (first row), it is evident that the pressure gradient (together with the buoyancy force for RC2) is balanced mainly by the Coriolis force, while the viscous force is comparatively negligible. This is the geostrophic balance modified by the presence of buoyancy, given by the following equation.

$$-\nabla P + T\hat{\mathbf{e}}_z + (1/Ro)\hat{\mathbf{e}}_x \times \mathbf{u} \approx 0. \quad (3.5)$$

However, inside the Ekman layer (second rows in Figs. 3.9 and 3.10), we see that the viscous force is significant and contributes to the force balance. As expected, the nature of the viscous force is such that it opposes the bulk cyclonic flow and the radially inward flow associated with Ekman pumping. The spiral nature of the flow inside the Ekman layer is clearly evident at this location, unlike that at  $x = 0.5$ . In this case, the pressure gradient (together with the buoyancy force for RC2) is balanced by both the Coriolis and viscous

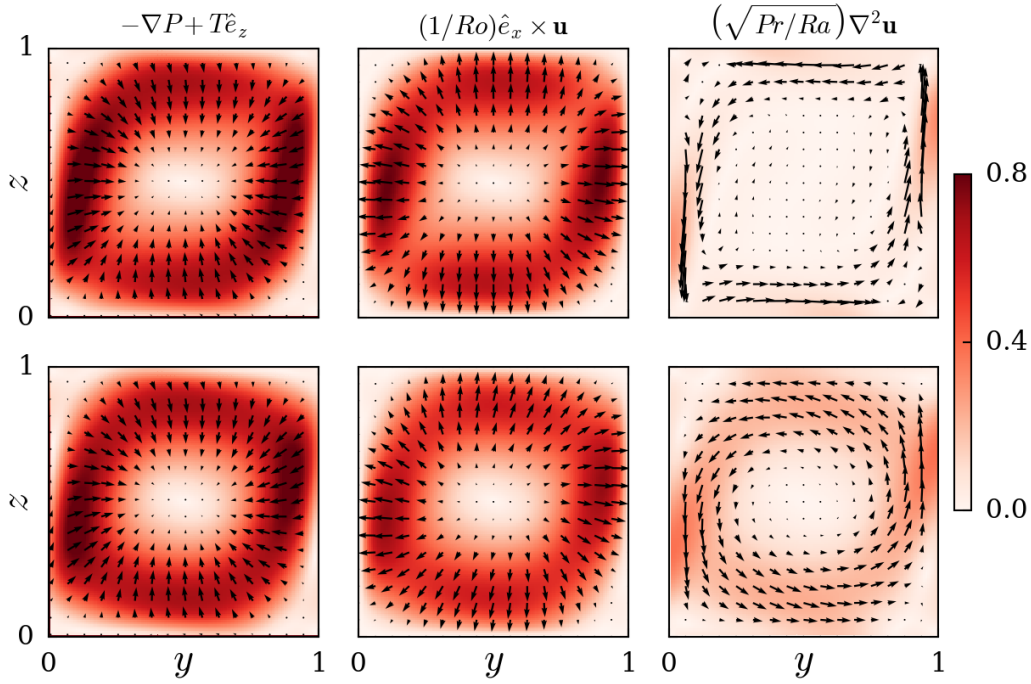


Figure 3.9: Force balance between pressure gradient (including temperature) and Coriolis forces in  $yz$ -plane at  $x = 0.5$  (first row) and  $x = 0.05$  (second row) for RC2. Vectors represent the respective force directions whereas colors represent their magnitude. Direction of rotation is into the page.

forces. This is the force balance inside the Ekman boundary layer for rotating flows, given by the following equation:

$$-\nabla P + T\hat{\mathbf{e}}_z + (1/Ro)\hat{\mathbf{e}}_x \times \mathbf{u} + \left(\sqrt{\frac{Pr}{Ra}}\right) \nabla^2 \mathbf{u} = 0. \quad (3.6)$$

By contrasting the force balance between RC2 and RH (Figs. 3.9 and 3.10), we note that in the presence of buoyancy, an asymmetry in the force distribution in the  $yz$ -plane is introduced, since the fluid has an additional forcing along the  $z$ -direction. As the heated/cooled fluid is convected by the cyclone, it tends to rise and fall close to the sidewalls normal to the  $y$ -axis. Thus the buoyancy force makes the cyclonic flow stronger in regions closer to and along the walls normal to the  $y$ -axis (Figs. 3.5, 3.9). This is seen in the form of stronger cyclonic velocities parallel to the  $z$ -axis and slightly weaker velocities parallel to the  $y$ -axis for the case RC2. The concentrated circular cyclone of the case RH (Figs. 3.5, 3.10) takes an annular

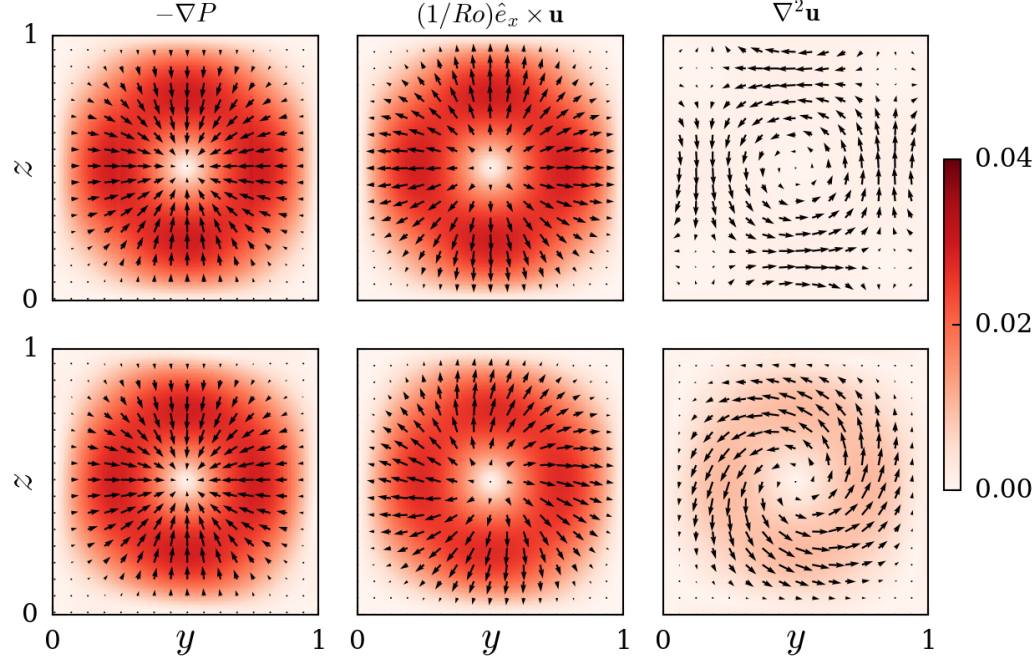


Figure 3.10: Force balance between pressure gradient and Coriolis forces in  $yz$ -plane at  $x = 0.5$  (first row) and  $x = 0.05$  (second row) for RH. Vectors represent the respective force directions whereas colors represent their magnitude. Direction of rotation is into the page.

form in the presence of buoyancy with a "near-dead" flow region at the center. Accordingly, the regions of large radial pressure gradients and high Coriolis forces (and consequently, the regions of significant Ekman pumping) also migrate away from the axis of rotation (Fig. 3.9).

We also analyze the various sources of helicity generation using the following helicity budget equation which can be derived by obtaining  $\boldsymbol{\omega} \cdot \partial \mathbf{u} / \partial t + \mathbf{u} \cdot \partial \boldsymbol{\omega} / \partial t$  [10],

$$\frac{\partial h}{\partial t} = -\nabla \cdot \mathbf{F} + h_T + h_\nu, \quad (3.7)$$

where we have ignored the advection term for small Rossby number. Here,

$$\mathbf{F} = \frac{1}{Ro} \mathbf{u}^2 \hat{\mathbf{e}}_x + \frac{1}{Ro} \mathbf{u} \times \hat{\mathbf{e}}_x \cdot \nabla \mathbf{a} + p \boldsymbol{\omega},$$

$$h_T = \boldsymbol{\omega} \cdot T \hat{\mathbf{e}}_z + \mathbf{u} \cdot (\nabla T \times \hat{\mathbf{e}}_z),$$

$$h_\nu = \sqrt{\frac{Pr}{Ra}} (\boldsymbol{\omega} \cdot \nabla^2 \mathbf{u} + \mathbf{u} \cdot \nabla^2 \boldsymbol{\omega}).$$

$\mathbf{F}$  represents the flux of helicity, and  $h_T$  and  $h_\nu$  are the sources of helicity due to buoyancy and viscous forces, respectively. The vector  $\mathbf{a}$  in the expression for  $\mathbf{F}$  is a solenoidal vector potential for  $\mathbf{u}$  ( $\mathbf{u} = \nabla \times \mathbf{a}$ ,  $\nabla \cdot \mathbf{a} = 0$ ). We denote the helicity fluxes due to Coriolis and pressure-vorticity forces as  $\mathbf{F}_\Omega = (1/Ro)\mathbf{u}^2\hat{\mathbf{e}}_x$  and  $\mathbf{F}_{p\omega} = p\boldsymbol{\omega}$ , respectively. For a geostrophic flow, the contribution of the second term in  $\mathbf{F}$  towards helicity segregation is expected to be negligible [10] and, therefore, we ignore it in this analysis.

In Fig. 3.11, we plot the variation of  $-\nabla \cdot \mathbf{F}_\Omega$ ,  $-\nabla \cdot \mathbf{F}_{p\omega}$ ,  $h_T$ , and  $h_\nu$  (averaged in the  $yz$ -plane) along the rotation axis. We note that there is a significant helicity flux both from the pressure-vorticity term ( $-\nabla \cdot \mathbf{F}_{p\omega}$ ) and from the Coriolis term ( $-\nabla \cdot \mathbf{F}_\Omega$ ). This generation and transport are similar to the mechanism proposed by Deusebio and Lindborg [82] where the pressure-vorticity flux leads to the generation of helicity, analogous to the generation of kinetic energy by pressure work. Buoyancy also contributes to helicity segregation, but its contribution is lower than that of Coriolis and pressure-vorticity forces in our simulations. Note that the sign of helicity segregation due to the viscous force is opposite to that of Coriolis and buoyancy forces, in agreement with the observations in the dynamo simulations of Ranjan et al. [10]. Another interesting observation, in particular for the case RC2, is that the helicity flux due to pressure-vorticity force ( $\mathbf{F}_{p\omega}$ ) is approximately balanced by the helicity due to the viscous force ( $h_\nu$ ).

### 3.4 Discussion and Conclusions

In this work, we numerically investigated the role of Ekman pumping in the segregation of kinetic helicity. Our domain of interest is a Cartesian box with the rotation axis perpendicular to gravity, inspired by the equatorial regions in the Earth's core. We performed simulations at fixed Rayleigh and Prandtl numbers for two values of the Taylor number,  $Ta = 10^5$  and  $10^6$ , and two boundary conditions – no-slip and fixed stress on the walls normal to the rotation axis (see Table 3.1). At large  $Ta$  (strong rotation), our results show that the normalized helicity is negative in the regions closer to  $x = 0$ , and positive in the regions closer to  $x = 1$  (recall that  $x = 0$  and  $x = 1$  correspond to the vertical walls normal to the rotation axis). In spherical dynamo simulations, such as those shown in Figure 3.1, these half-volumes correspond to

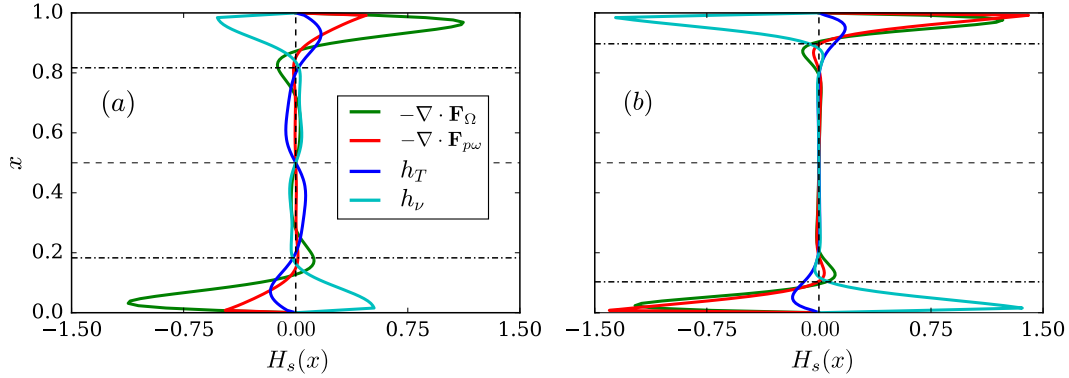


Figure 3.11: Variation of the helicity flux and helicity source terms averaged in  $yz$ -plane ( $H_s$ ) along the rotation axis ( $x$ -direction) for (a) RC1, and (b) RC2. Note that  $-\nabla \cdot \mathbf{F}_\Omega$  and  $-\nabla \cdot \mathbf{F}_{p\omega}$  terms represent the helicity flux due to Coriolis force and pressure-vorticity force respectively, whereas  $h_T$  and  $h_v$  terms represent the helicity generation due to buoyancy force and viscous force respectively. Dot-dashed lines represent the Ekman boundary layer thickness.

the north and south of the equator, respectively. Moreover, we found that the peak helicity magnitude occurs inside the Ekman layers indicating that the helicity is generated here and transported to the bulk regions. Analysis of the helicity budget shows that the Coriolis and the pressure-vorticity fluxes contribute to the observed segregation of helicity.

We also analyzed the three constituents of helicity,  $V_x\omega_x$ ,  $V_y\omega_y$ , and  $V_z\omega_z$ , to investigate the cause of helicity segregation. By observing the distributions of these constituents at different planes in the domain, we concluded that Ekman pumping and cyclonic structures are together responsible for this helicity segregation. We found that near the Ekman boundary layer,  $V_x$ ,  $\omega_y$ , and  $\omega_z$  are generated by Ekman pumping, whereas the cyclonic flow drives  $V_y$ ,  $V_z$ , and  $\omega_x$  (recall that the rotation vector is along  $-x$ ). The coupled effect of these two phenomena leads to the observed helicity segregation. The helicity magnitudes were found to be smaller for the constant stress simulations and localized very close to the wall, as compared to the no-slip simulations. With an increase in  $Ta$ , the velocity gradients parallel to the rotation axis decrease, as expected from the Taylor-Proudman theorem. Therefore, with an increase in  $Ta$  and for lower values of  $Ra/Ta$ , the average helicity in the bulk regions

of the box (in the same half) has the same sign as the helicity in the Ekman layers. Our results suggest that helicity in the dynamo simulations at large  $Ta$  but small  $Ra/Ra_{critical}$  arises due to Ekman pumping. We also presented a modal energy analysis to quantify the relative energies of the dominant structures in the flow and found that the secondary rolls (represented by the mode  $(2, 2)$ ) generated by Ekman pumping to be an important flow feature. This is the first numerical demonstration of helicity segregation by Ekman pumping in a simple box geometry and is in agreement with the predictions by Busse [62] and Olson et al. [56].

The role of buoyancy in helicity generation and segregation is an important topic of great interest to geophysical and astrophysical community. For instance, in the context of solar dynamos, Duarte et al. [83] reported helicity inversion due to buoyancy gradients. In a recent letter, Agoua et al. [84] found spontaneous helicity generation and also reversal in sign due to buoyancy effects in quasi two-dimensional (anisotropic) turbulence. In this work, we observed that buoyancy plays an important role in the migration of the secondary rolls associated with the Ekman pumping (and so the helicity concentration) away from the rotation axis. In the future, we plan to vary the Rayleigh number to investigate in detail the effect of buoyancy force. We will also investigate other configurations where gravity and rotation are inclined at different angles to each other, as well as the case where a mean magnetic field is present.

# Chapter 4

## Conclusions

The main goal of this thesis is to investigate the effect of roughness on Rayleigh-Bénard Convection (RBC) with and without rotation. In Chapter 1, we discussed prior studies on Rayleigh-Bénard Convection (RBC) with and without rotation. In Chapter 2, we discussed our experimental setup in detail. The main diagnostics for the experiments are Nusselt number and optical (PIV) measurements. We designed our experimental setup keeping in view the above diagnostics. We performed Nusselt number measurements on a non-rotating Rayleigh Bénard experimental setup. Our experiment spans Rayleigh number ( $Ra$ ) range  $2.16 \times 10^8 \leq Ra \leq 2.07 \times 10^9$ . With the increase in Rayleigh number ( $Ra$ ), the boundary layer thickness decreases, and roughness elements protrude into the bulk flow. The thermal plumes emitted from tips of roughness enhance heat transfer strongly. To maintain the constant temperature of the bottom copper plate, we use our PID code designed on LabVIEW. The code maintains temperature within the range  $0.1^\circ\text{C}$ . This establishes our experimental protocol and will allow us to make further measurements on rotating setup in future experiments. We also plan to attain a higher Rayleigh number, in future experiments, by employing a bigger height RBC cell ( $Ra \propto H^3$ ) or using a working fluid with a higher ratio of thermal expansion coefficient to thermal and viscous diffusivity ( $Ra \propto \beta/(\nu\kappa)$ ).

In the second part of the thesis, we performed numerical simulation on rotating convection with a rotation axis orthogonal to gravity. These flows are important in the context of low latitude convection. We observed segregation of helicity, and its distribution along the

rotation axis is similar to what other authors have observed numerically. We study the role of Ekman pumping in helicity segregation. In the future, we plan to vary the Rayleigh number to investigate the effect of buoyancy force and extend our analysis to the case rotation parallel to gravity.

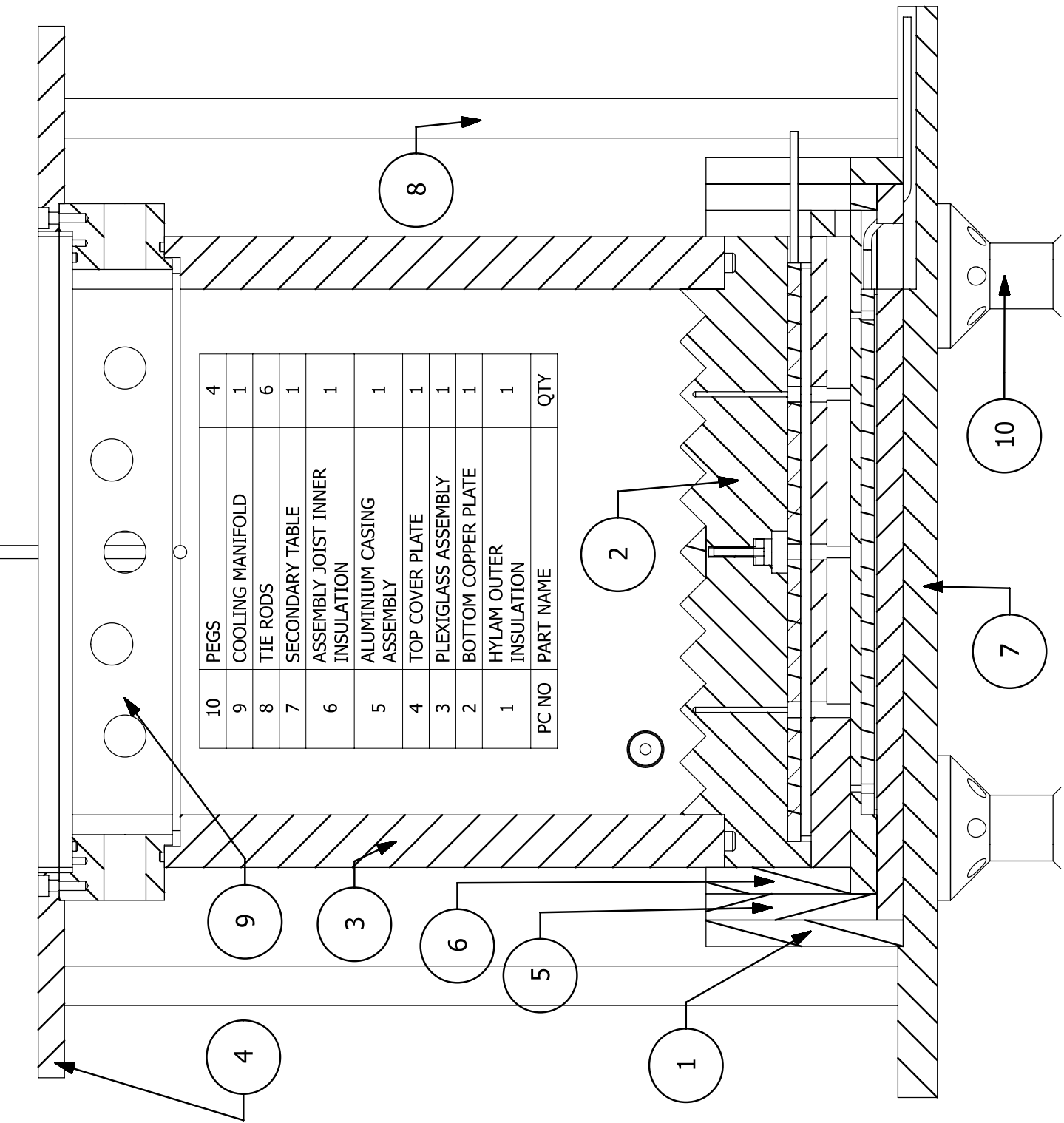
## **Appendix A**

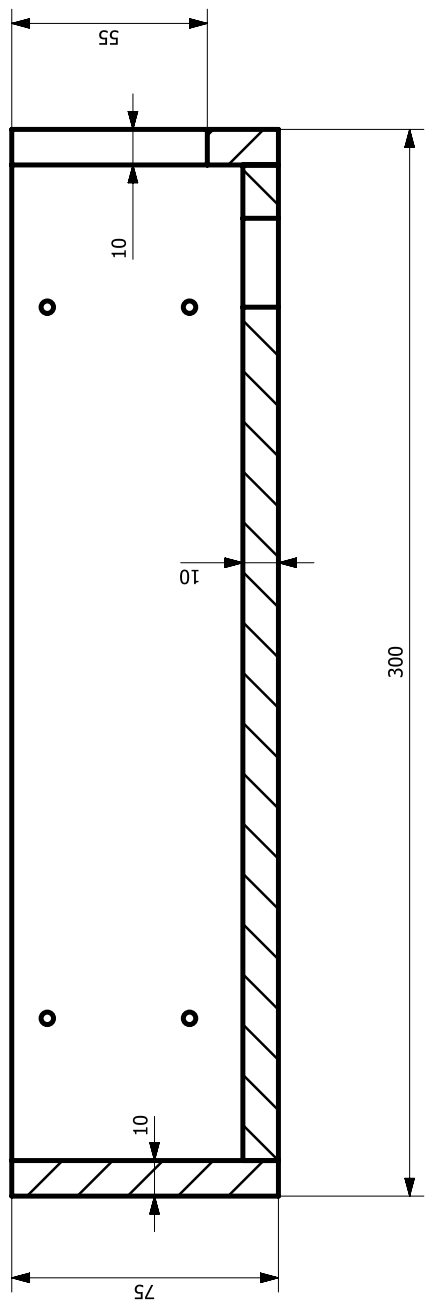
### **CAD drawings**

DWG:JPR-RRBC-Cell-0

SECTION B-B

B B



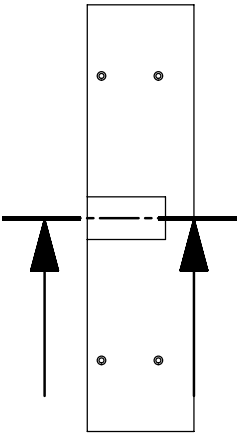
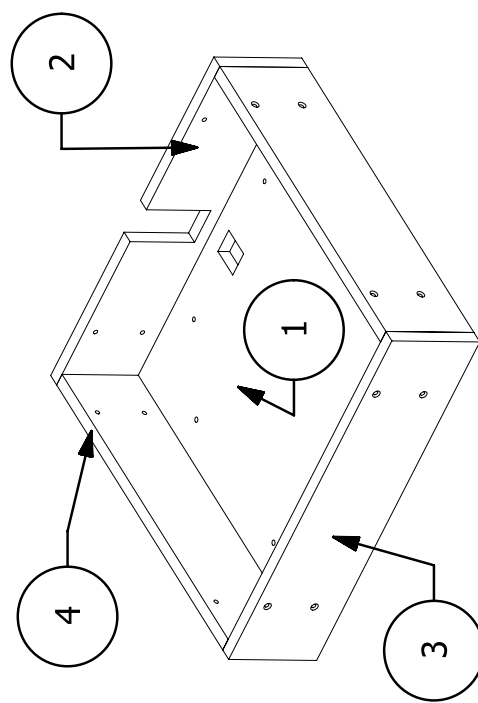


Hylam Outer Insulation      Quantity:1

DWG No: JPR-RRBC-Cell-1-0

Sub-Assembly Parts	DWG No.
Base Outer Insulation	JPR-RRBC-Cell-1-1
Hylam Insulation1	JPR-RRBC-Cell-1-2
Hylam Insulation2	JPR-RRBC-Cell-1-3
Side Short Outer Insulation	JPR-RRBC-Cell-1-4

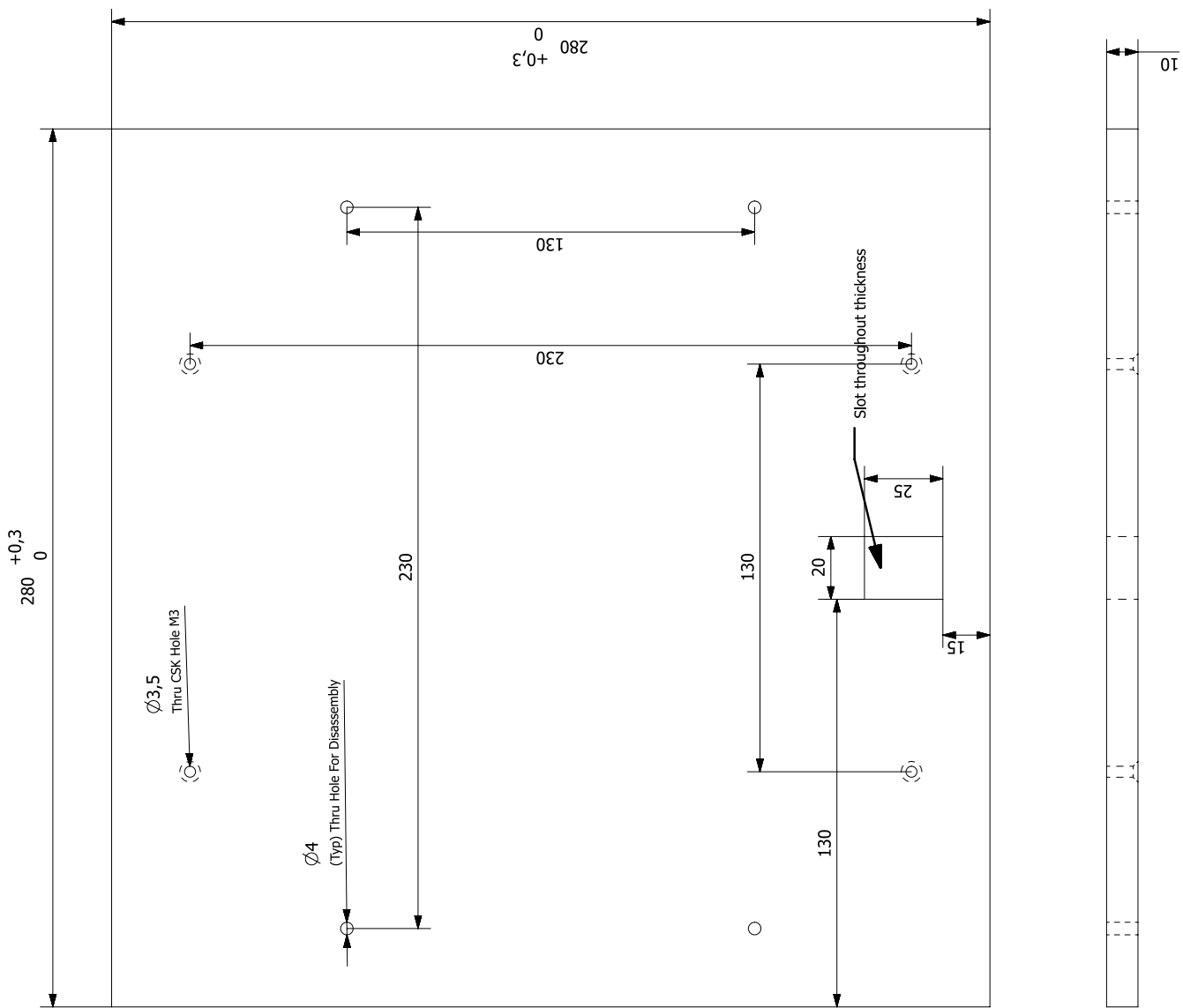
PC NO	PART NAME	QTY
4	SIDE SHORT OUTER HYLAM	2
3	LONG WALL OUTER HYLAM INSULATION 2	1
2	LONG WALL OUTER HYLAM INSULATION 1	1
1	BASE OUTER INSULATION	1

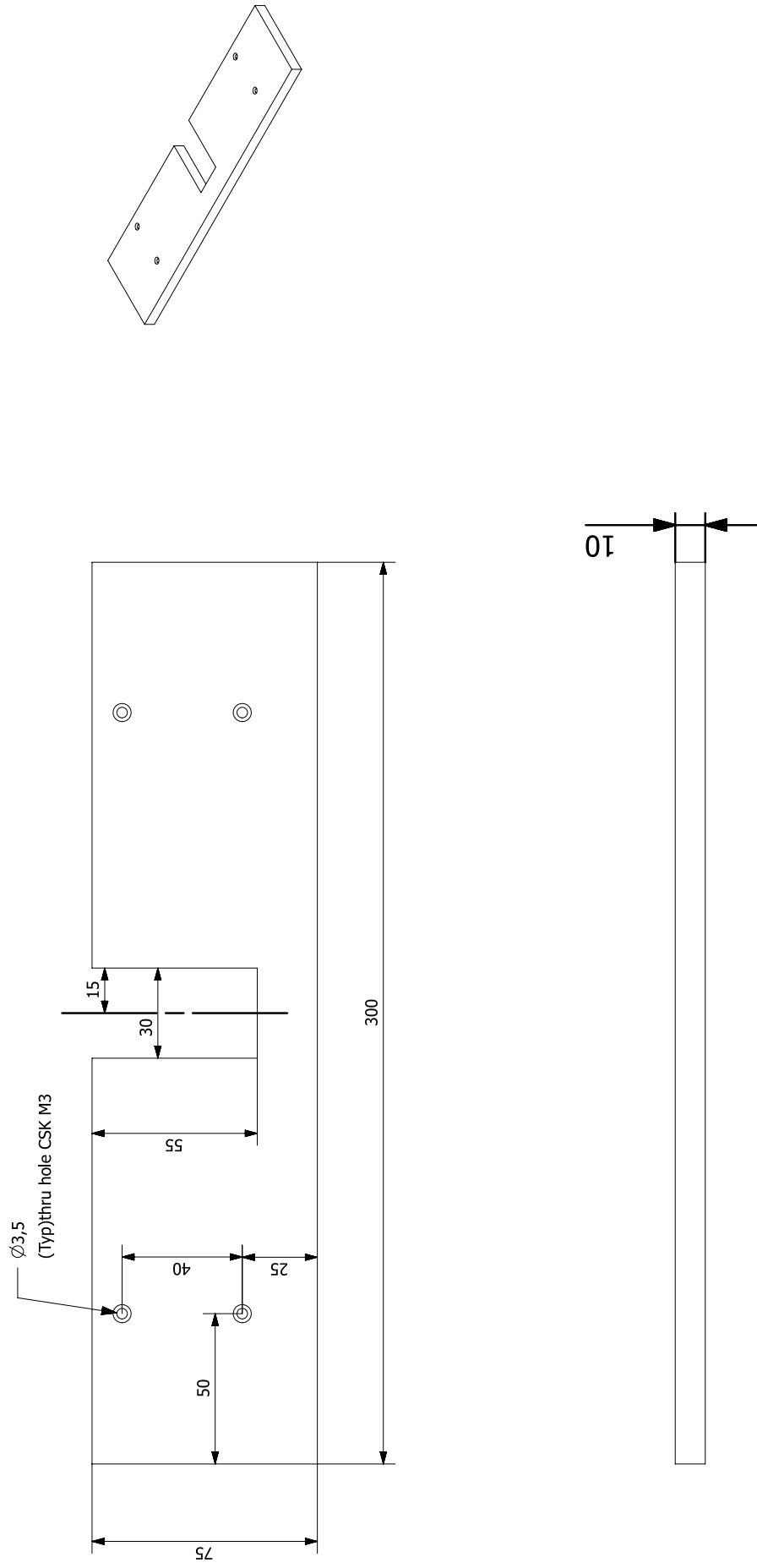


Outer Hylam Insulation (Base)

DWG No: JPR-RRBC-Cell-1-1

Quantity:1



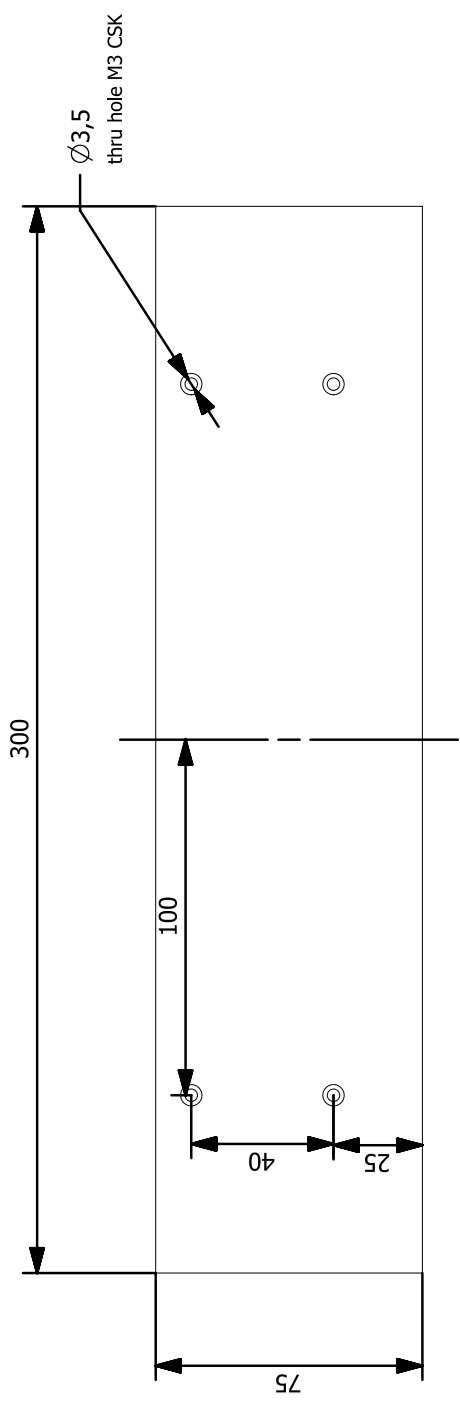
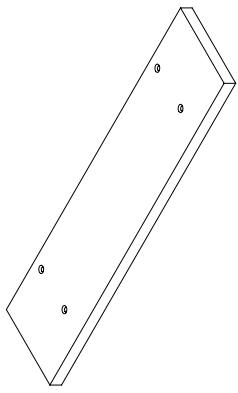


Outer Hylam Insulation (Side wall , Wire outlet Side)

DWG No: JPR-RRBC-Cell-1-2

Quantity 1

All Dimension in mm

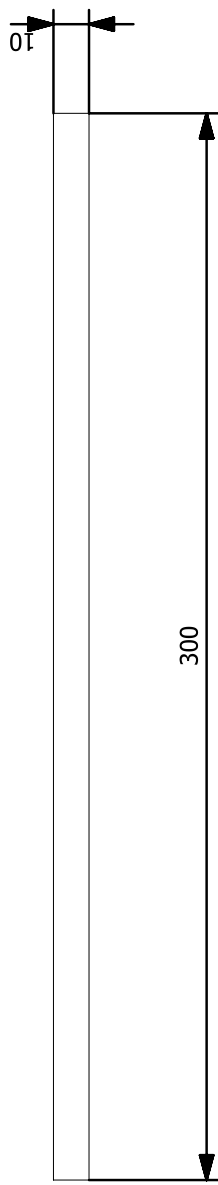


Outer Hylam Insulation (Side wall , long )

DWG No: JPR-RRBC-Cell-1-3

Quantity:1

All Dimension in mm

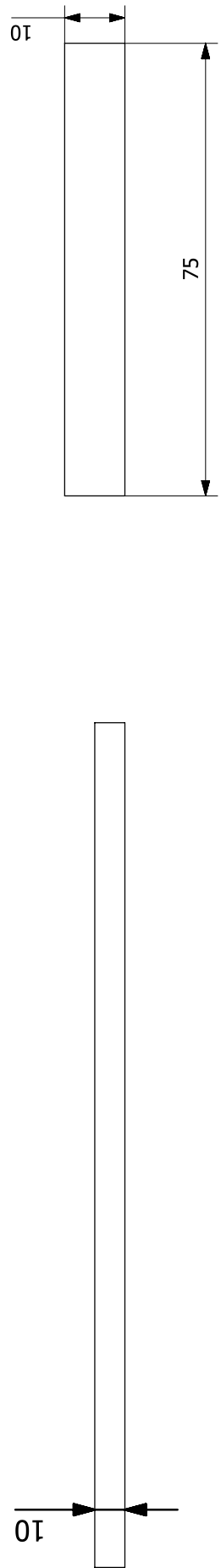
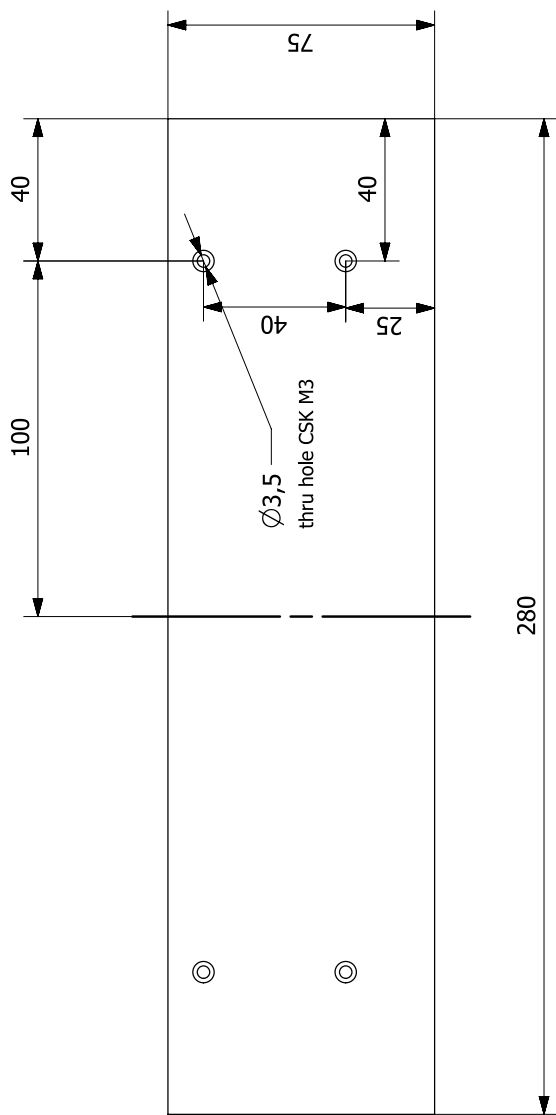


Outer Hylam Insulation (Side Short)

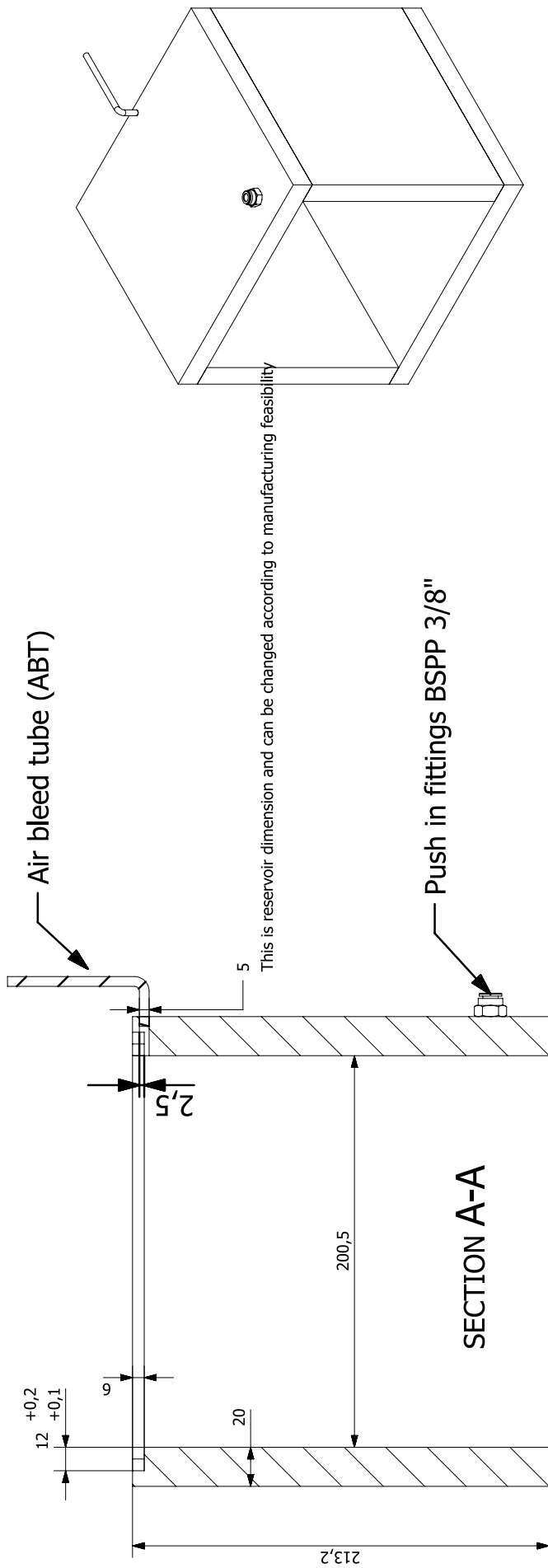
DWG No: JPR-RRBC-Cell-1-4

Quantity:2

All Dimension in mm

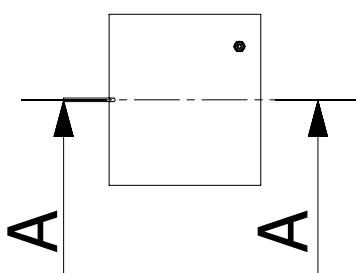


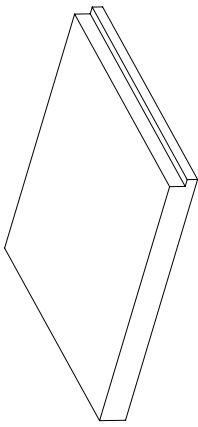




Tolerance are included in base dimension.  
Plexiglass Assembly RRBC Cell  
Quantity: 1  
DWG No: JPR-RRBC-Cell-3-0

PC NO	PART NAME	QTY
5	SMC_35	1
4	RESERVOIR	1
1	PLEXIGLASS 240	1
3	PLEXIGLASS 240	1
2	INLET	1
1	PLEXIGLASS 200	2





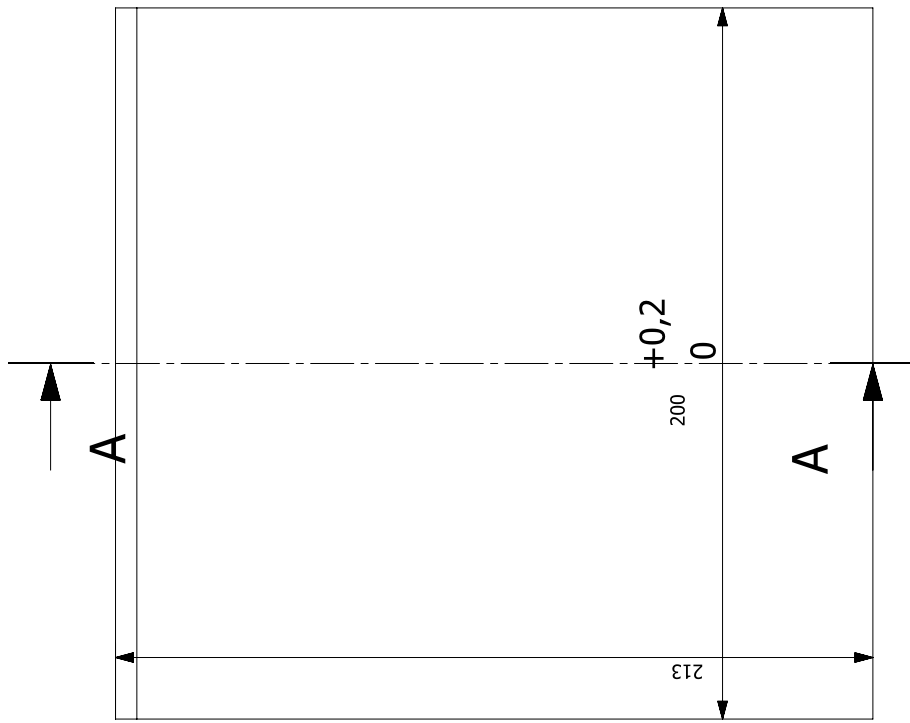
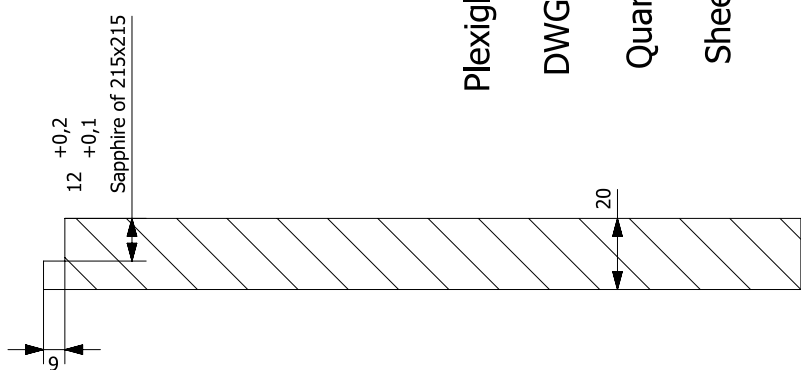
Plexiglass Assembly RRBC Cell Short Wall

DWG No: JPR-RRBC-3-1

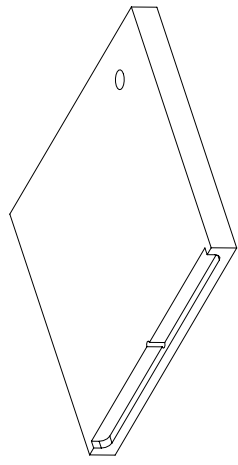
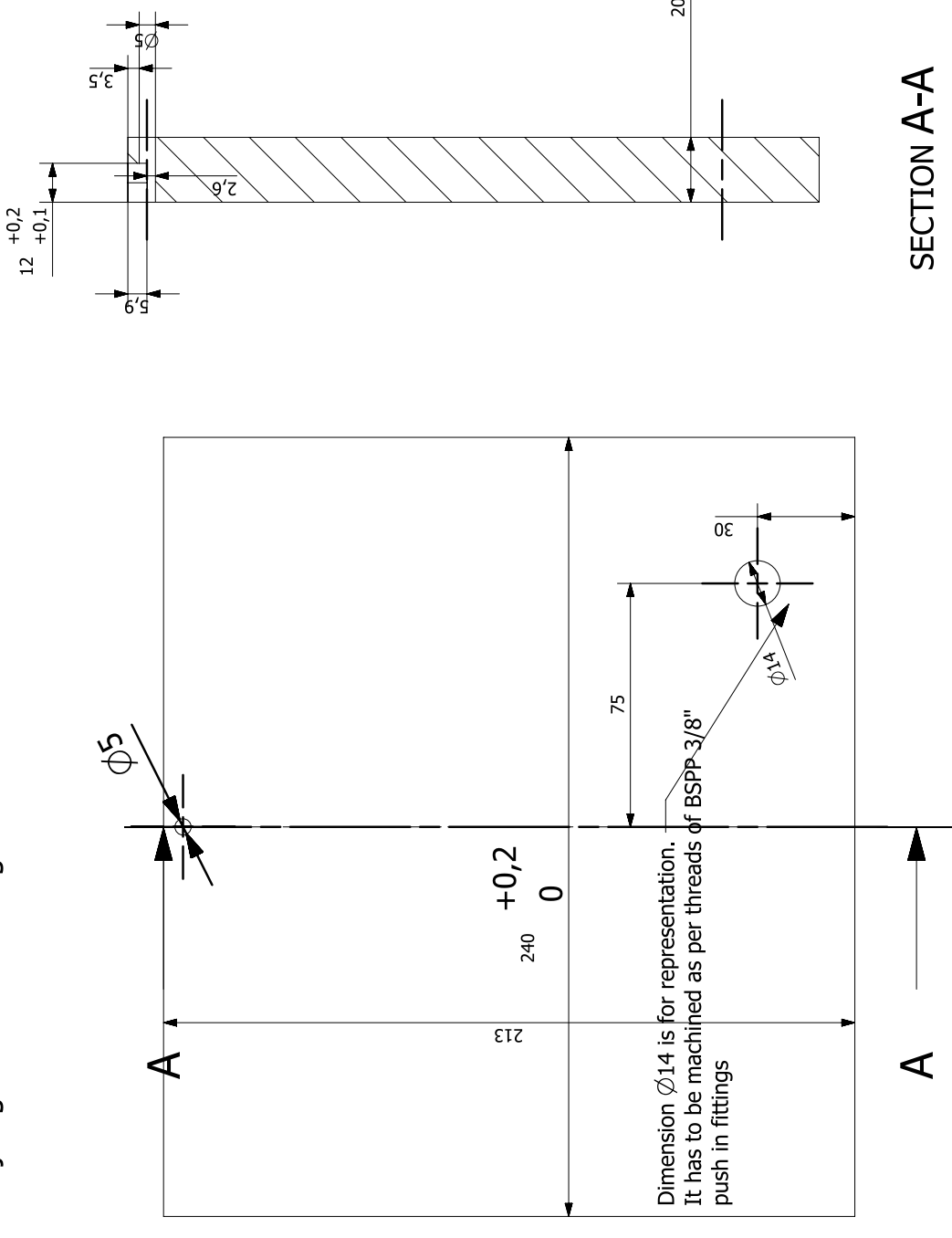
Quantity: 2

Sheet 1 of 3

SECTION A-A



joining corners for o-ring need to be decided

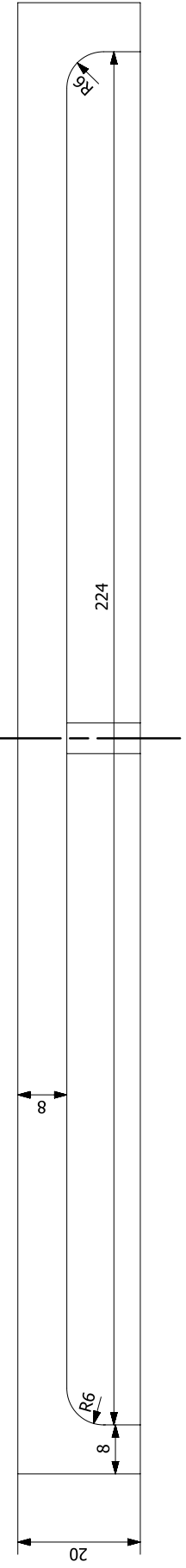


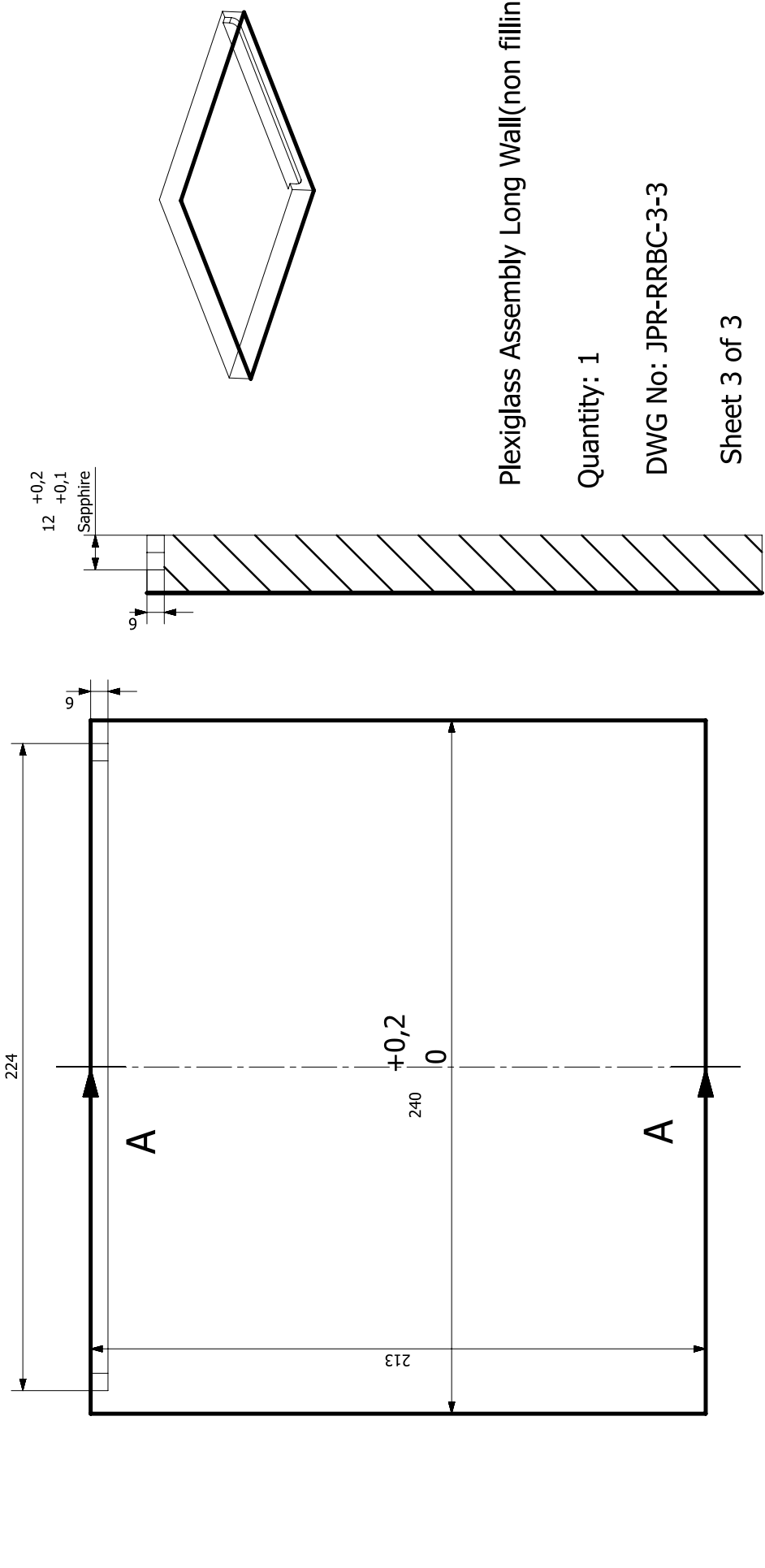
Plexiglass Assembly (Inlet)

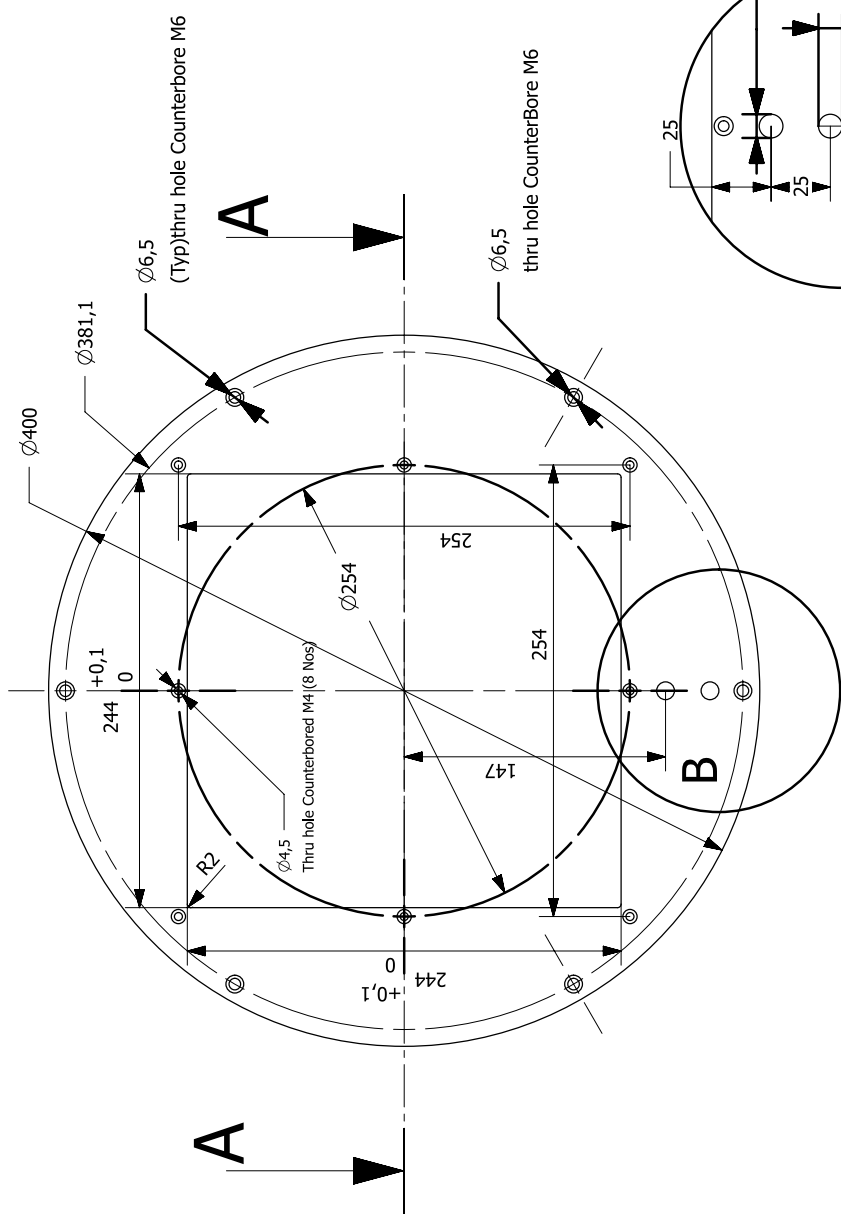
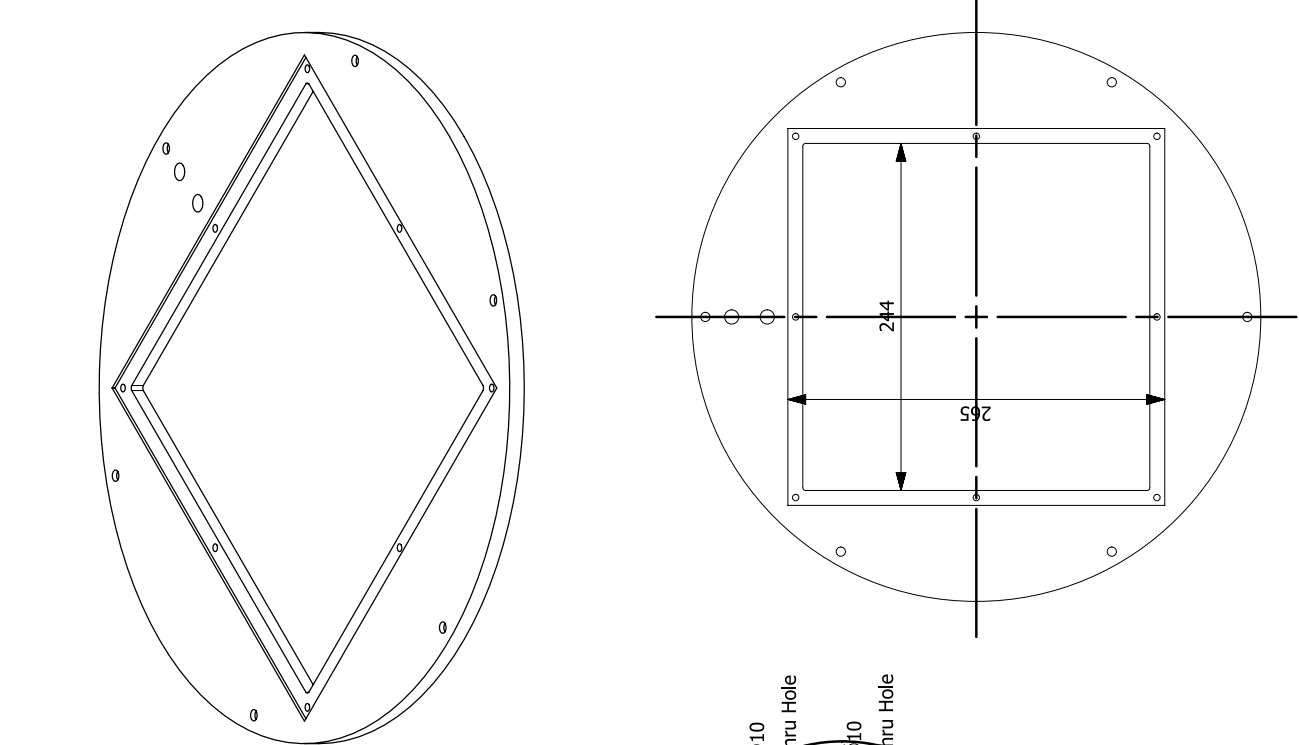
DWG No: JPR-RRBC-3-2

Sheet 2 of 3

SECTION A-A



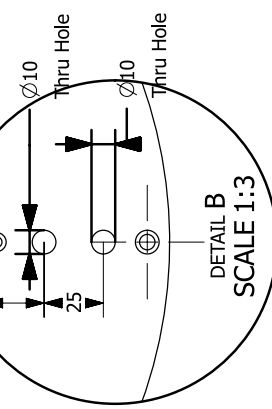




Aluminium Top Cover

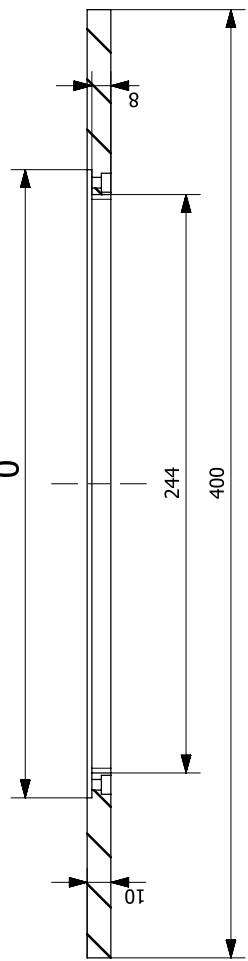
DWG No: JPR-RRBC-Cell-4-0

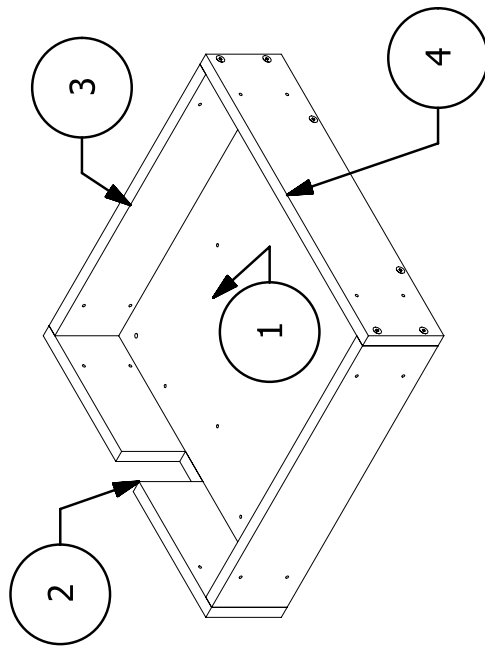
All Dimensions are in mm



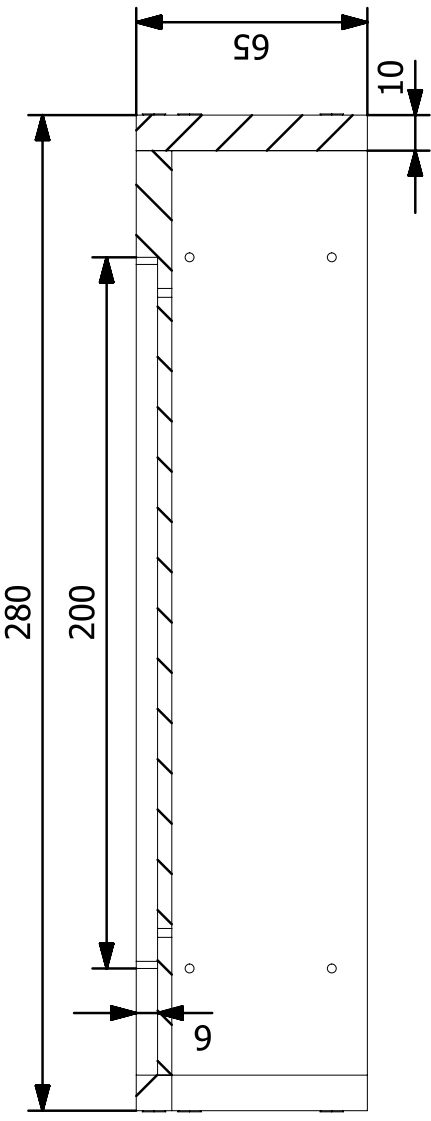
DETAIL B  
SCALE 1:3

This Dimension has to sit over  
265x265 Cooling Manifold(JPR-RREC-Cell-10) So tolerances provided accordingly





PC NO	PART NAME	QTY
6	M3X16	12
5	SECONDARY HEATER	1
4	ALUMINIUM CASING LONGER EDGE	1
3	ALUMINIUM CASING SHORTER EDGE	2
2	ALUMINIUM CASING LONGER EDGE WIRE OUTLET	1
1	ALUMINIUM CASING BASE	1

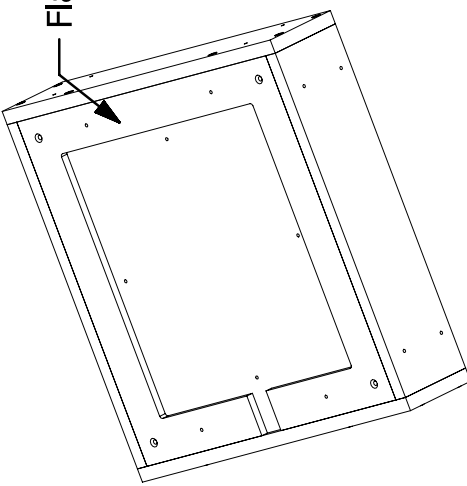


### Aluminium Casing Assembly

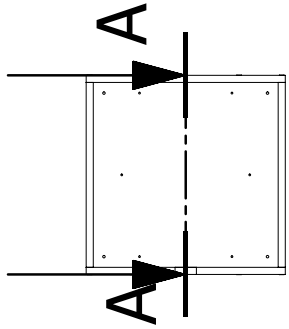
DWG No :JPR-RRBC-Cell-5-0

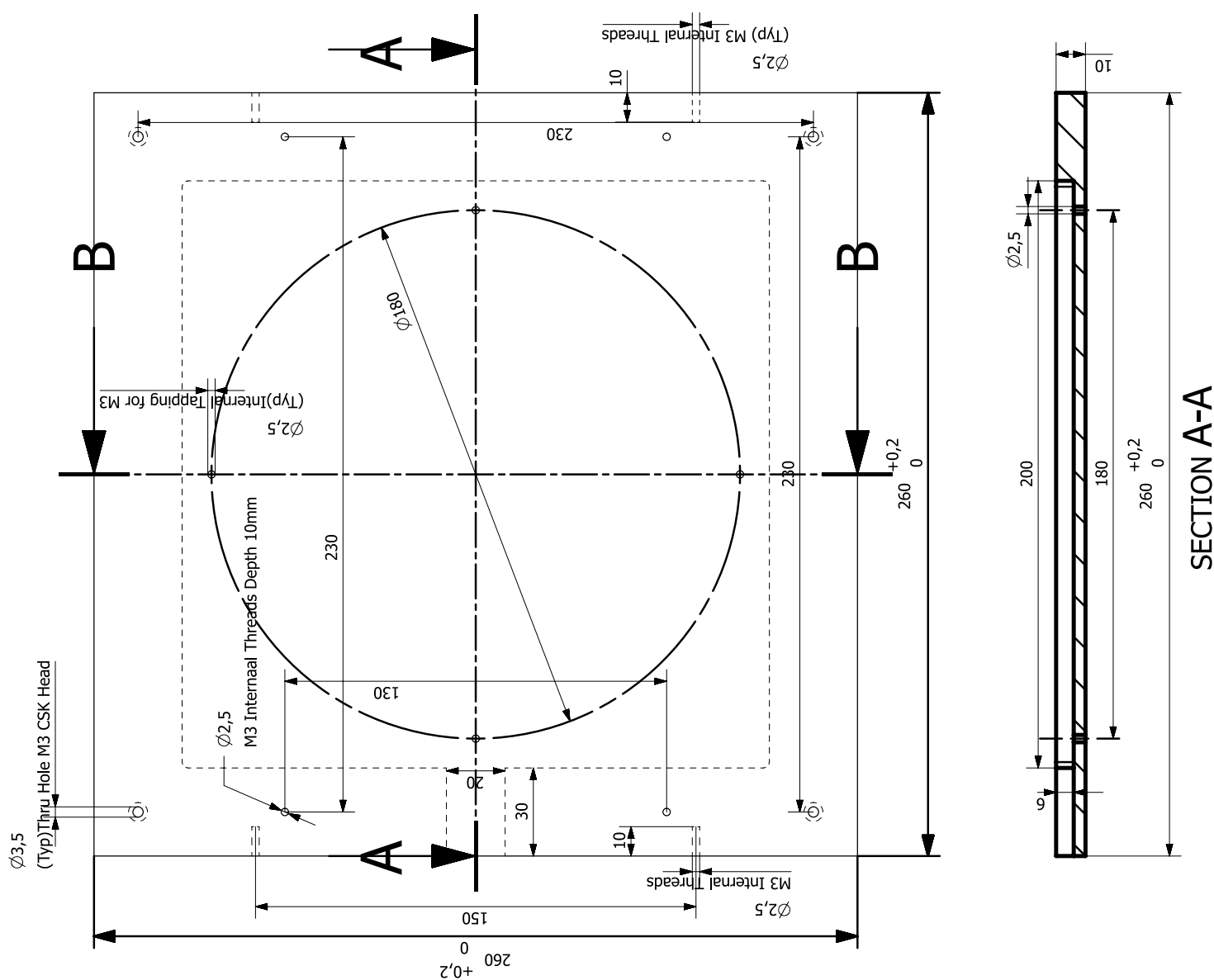
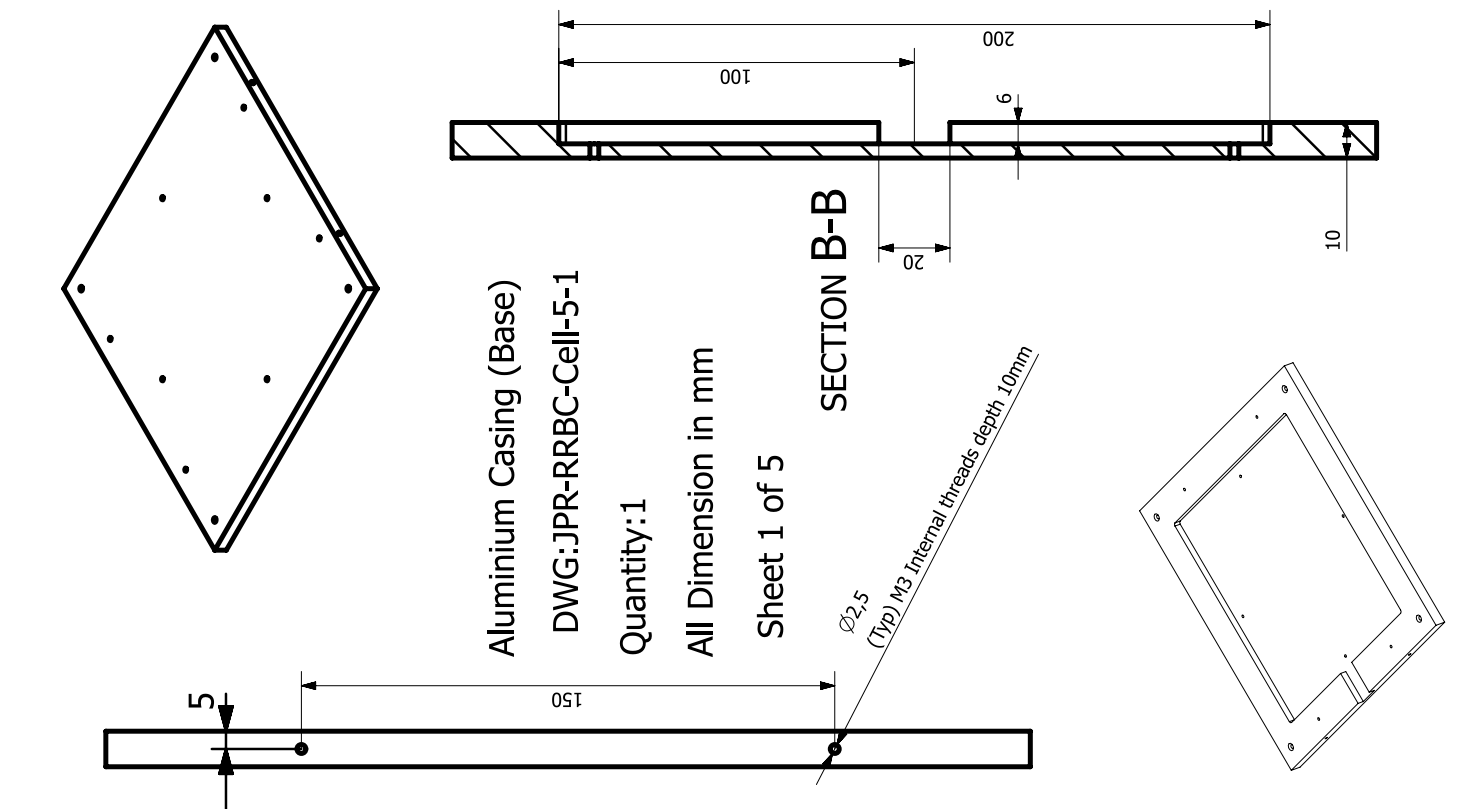
Sub Assembly Parts	Drawing No
Aluminium Casing Base	JPR-RRBC-Cell-5-1
Longer Edge Wire Outlet	JPR-RRBC-Cell-5-2
Aluminium Casing Shorter Edge	JPR-RRBC-Cell-5-3
Longer Edge	JPR-RRBC-Cell-5-4

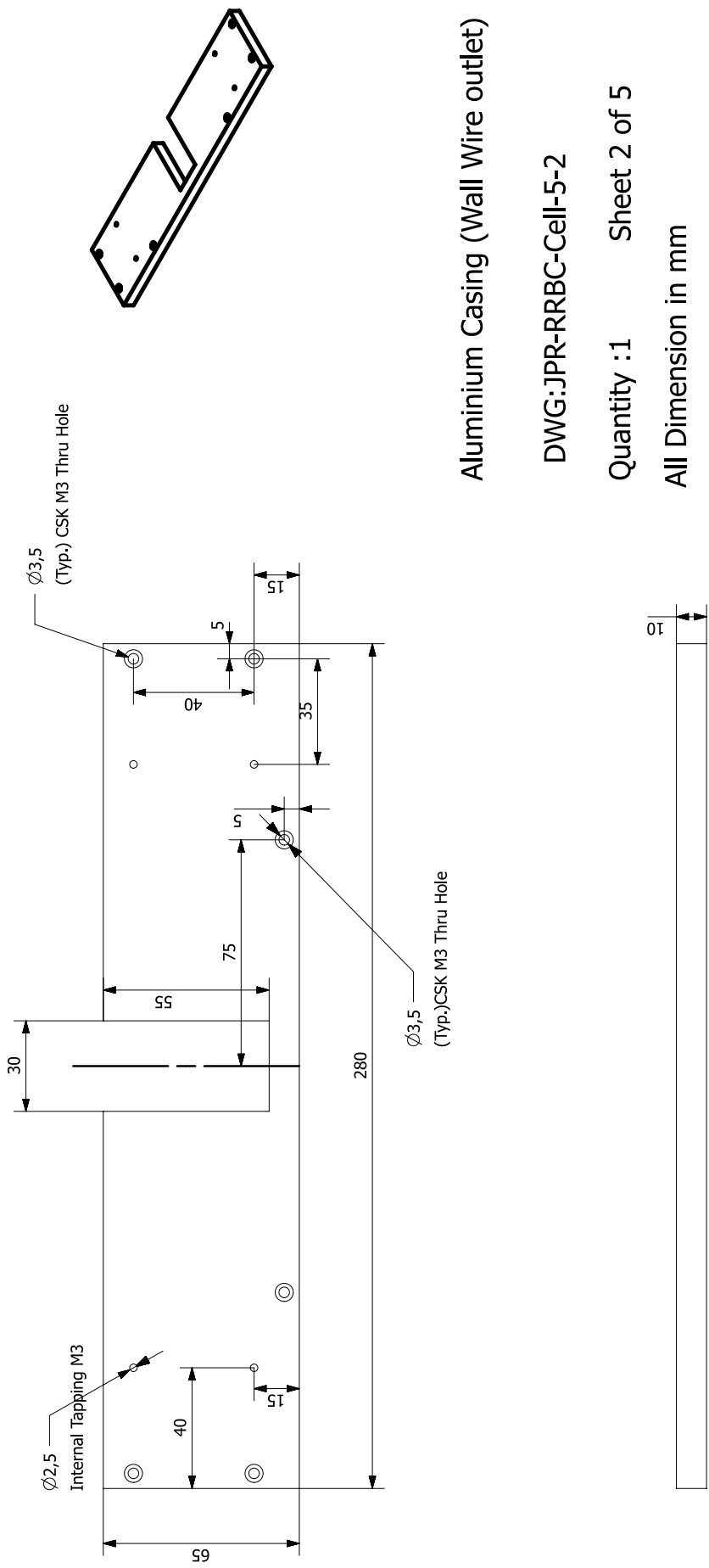
Approved By:	Dr. Pranav Joshi
Prepared By:	Abhilash Ojha

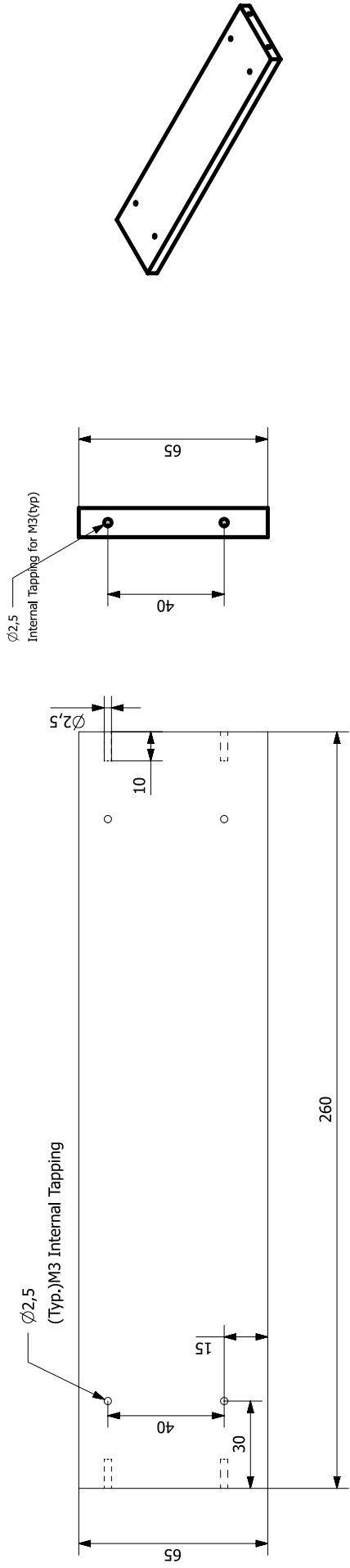


Flatness to be maintained







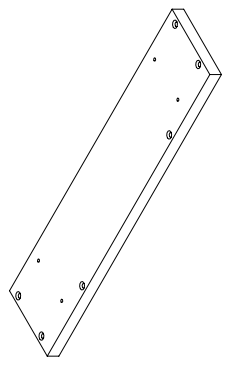


Aluminium Casing (Shorter Edge Edge)

DWG:JPR-RRBC-Cell-5-3

Quantity:2 → Sheet 3 of 5

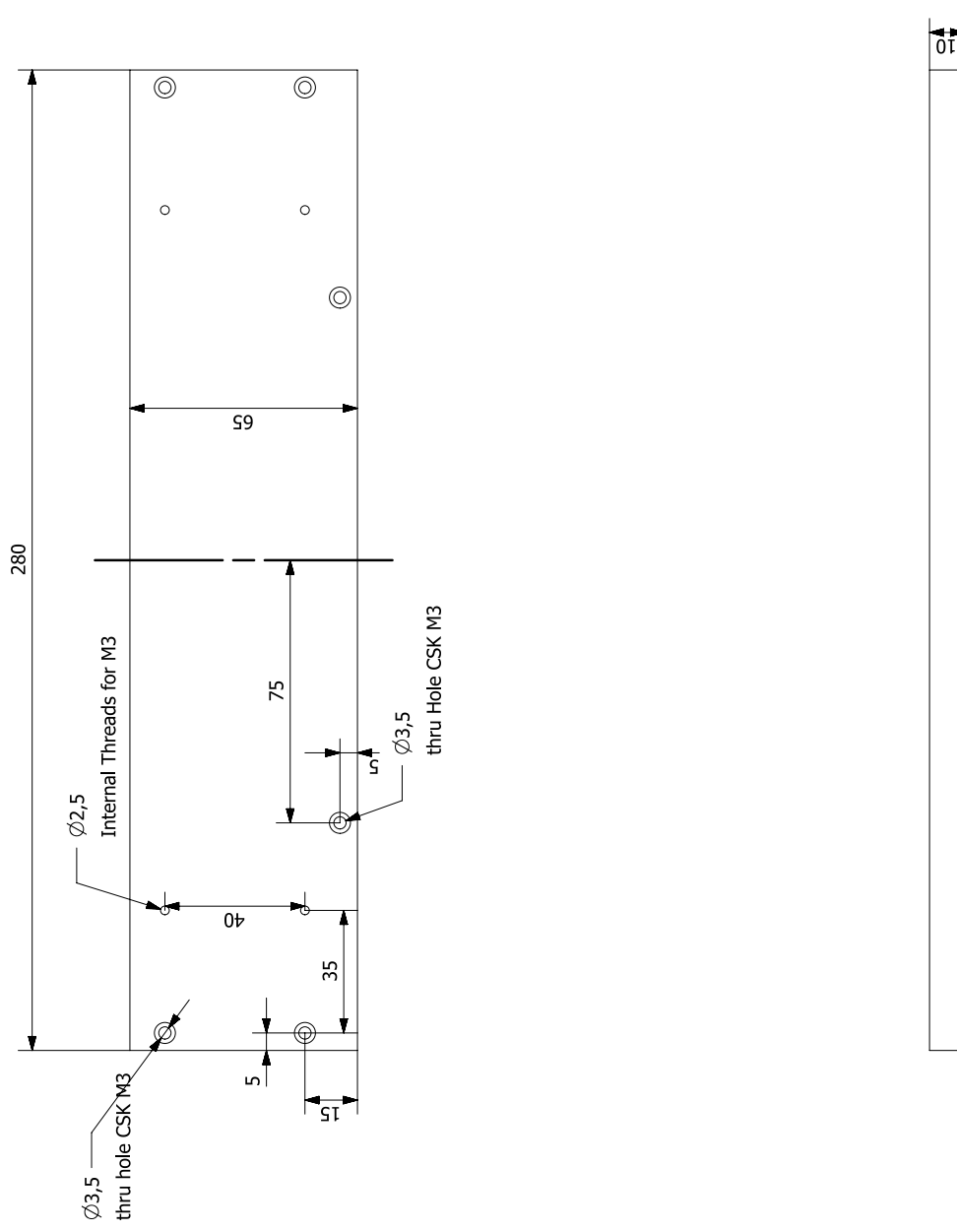


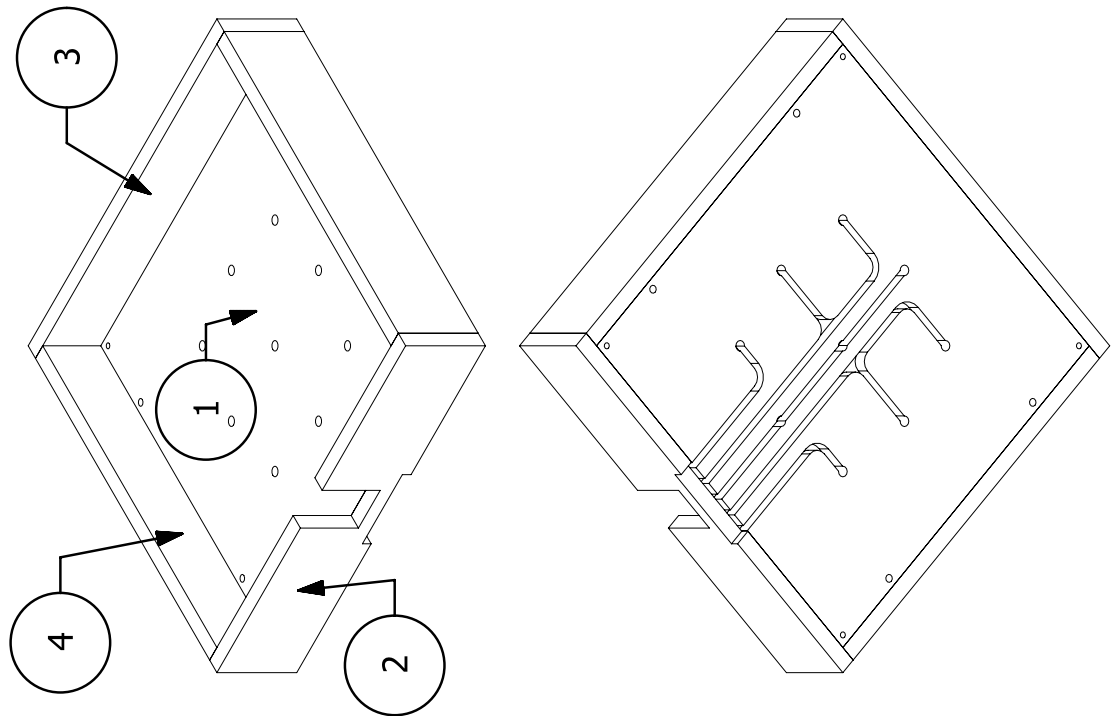


All Dimension in mm  
Aluminium Casing (Long Edge)

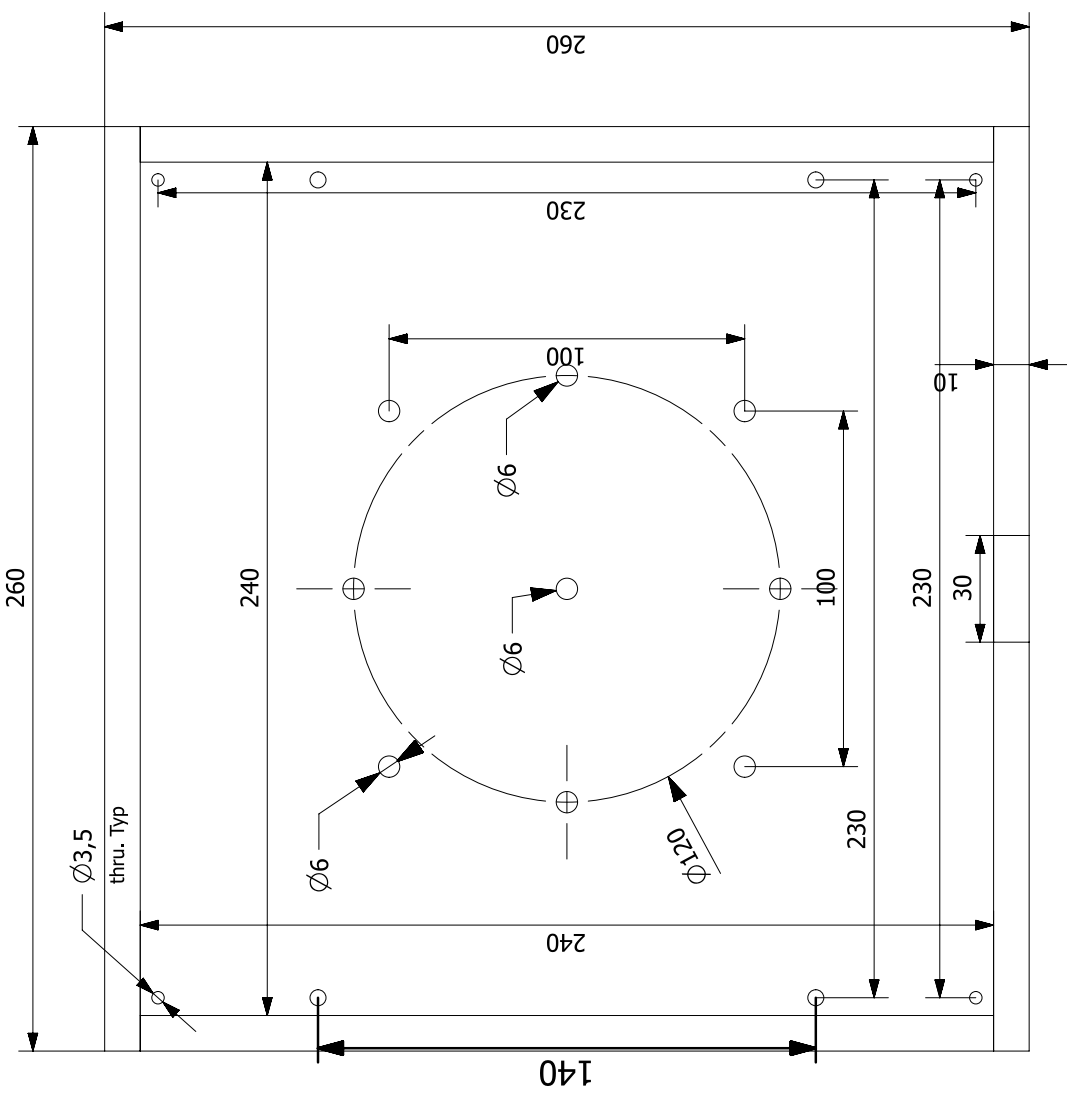
DWG:JPR-RRBC-Cell-5-4

Quantity: 1      Sheet 4 of 5





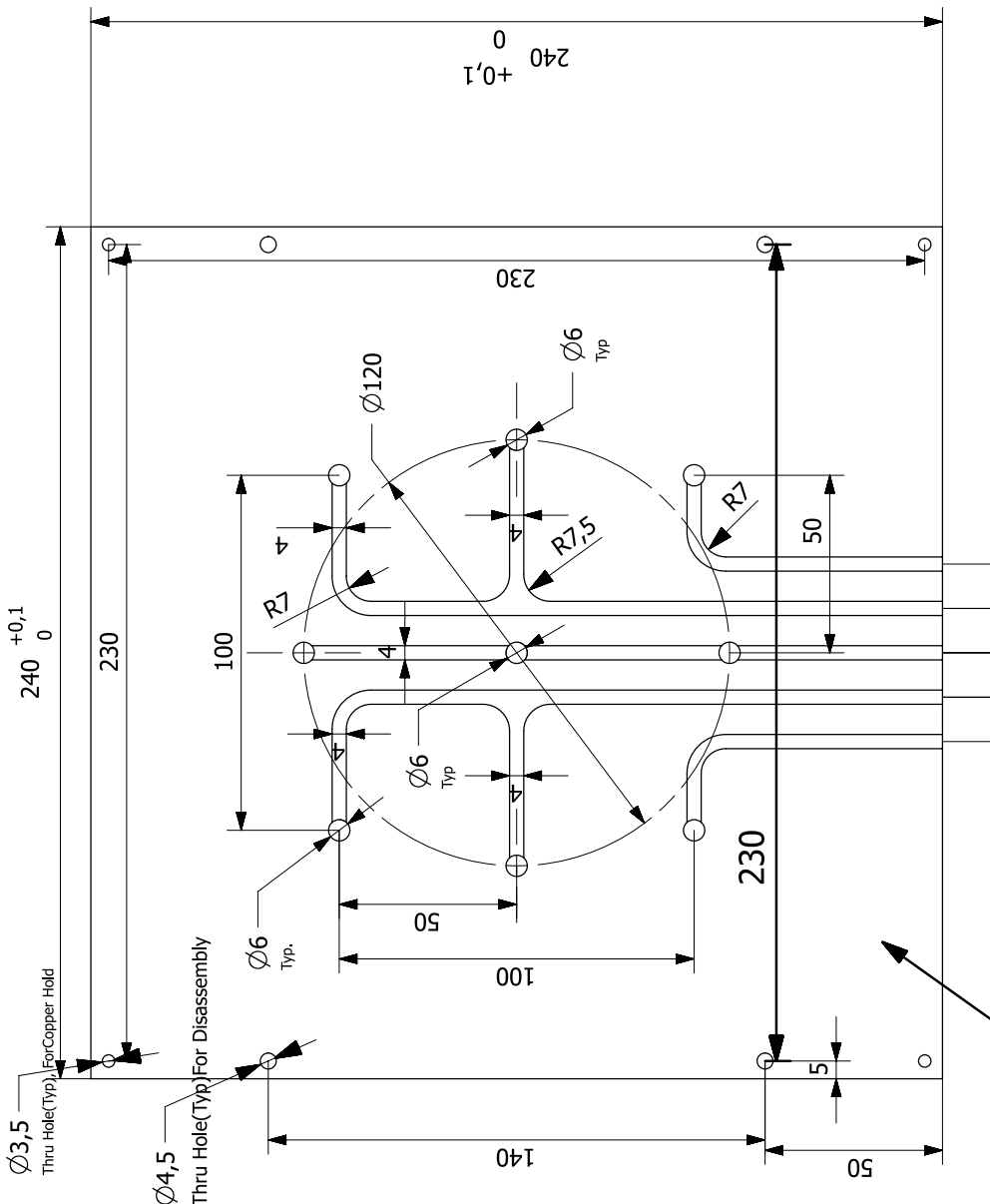
Sub Assembly Parts	Dwg No
Bottom Hylam Facesheet 15mm thick	JPR-RRBC-Cell-6-1
Side Long Insulation1	JPR-RRBC-Cell-6-2
Side Long Insulation2	JPR-RRBC-Cell-6-3
Hylam Facesheet/Side Short Insulation	JPR-RRBC-Cell-6-4



All Dimensions are in mm      Material: Hylam  
Inner Insulation Assembly      Quantity: 1  
  
DWG No:JPR-RRBC-Cell-6-0  
Material Provided by project

PC NO	PART NAME	QTY
4	HYLAM FACESHEET	2
3	HYLAM FACESHEET SIDE LONG INSULATION2	1
2	SIDE LONG INSULATION1 HYLAM OUTER	1
1	BOTTOM HYLAM FACESHEET10MM	1

Approved By:	Dr. Pranav Joshi
Prepared By:	Abhilash Ojha



VIEW A

Sheet 1 of 6

Inne Insulation (Base)

Quantity: 1

Material: Hylam

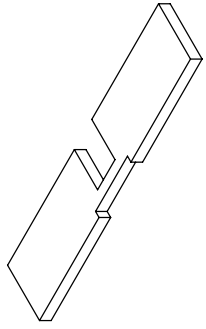
DWG No: JPR-RRBC-Cell-6-1

All Dimensions are in mm

Material Provided by project

A

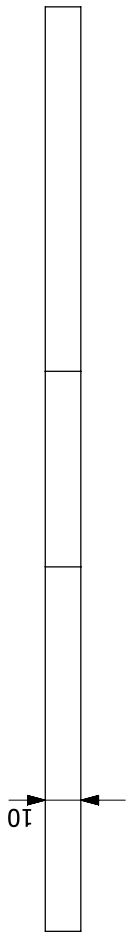
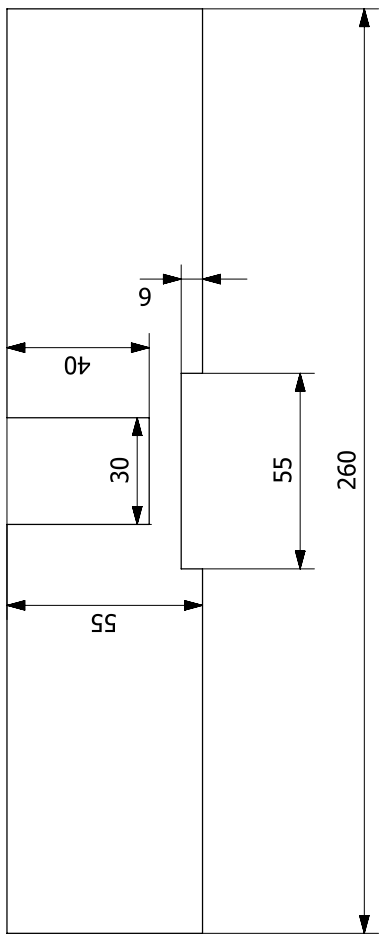
Flatness to be maintained

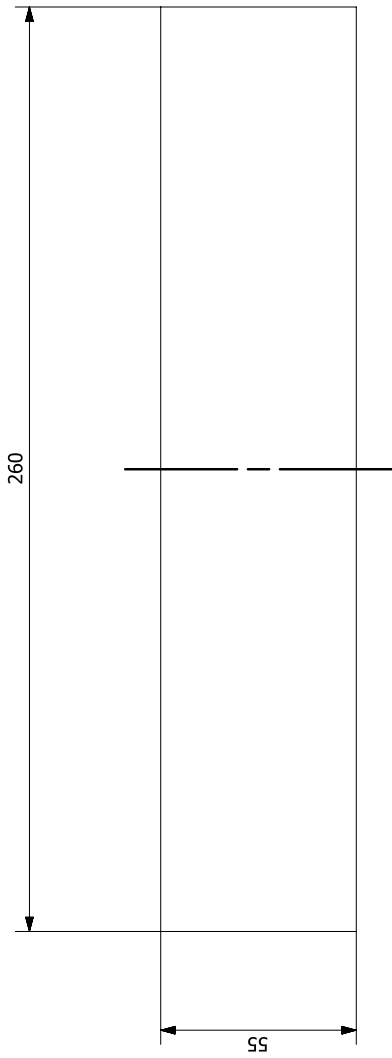


Inner Insulation Side Wall (Wire Outlet)

DWG No: JPR-RRBC-Cell-6-2

Quantity:1      Sheet 2 of 6



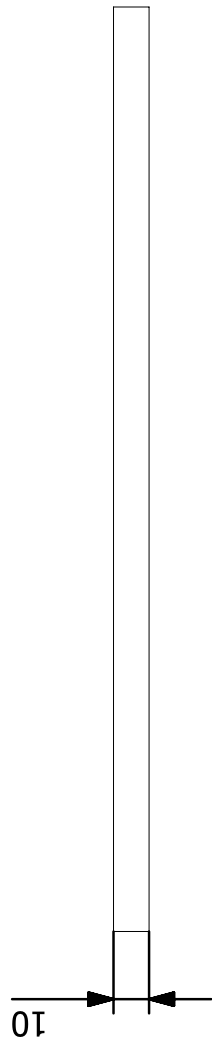


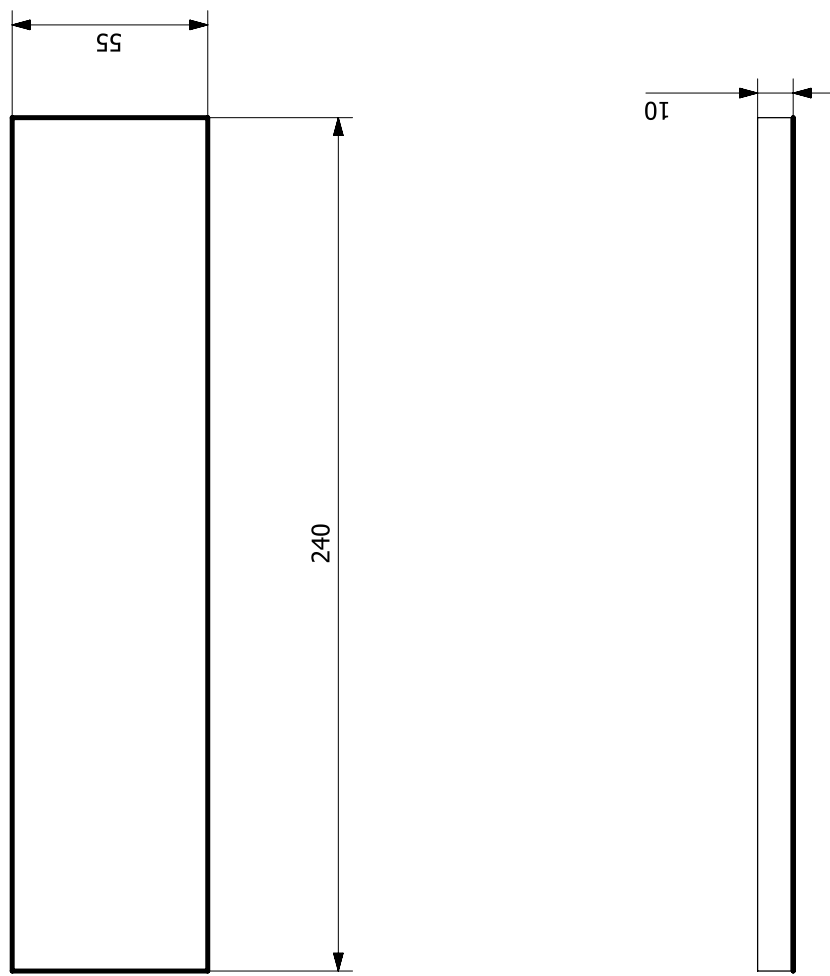
Inner Insulation Side wall 2( Longer Side)

Material: Hylam

DWG No.: JPR-RRBC-Cell-6-3  
Quantity: 1

Sheet 3 of 6





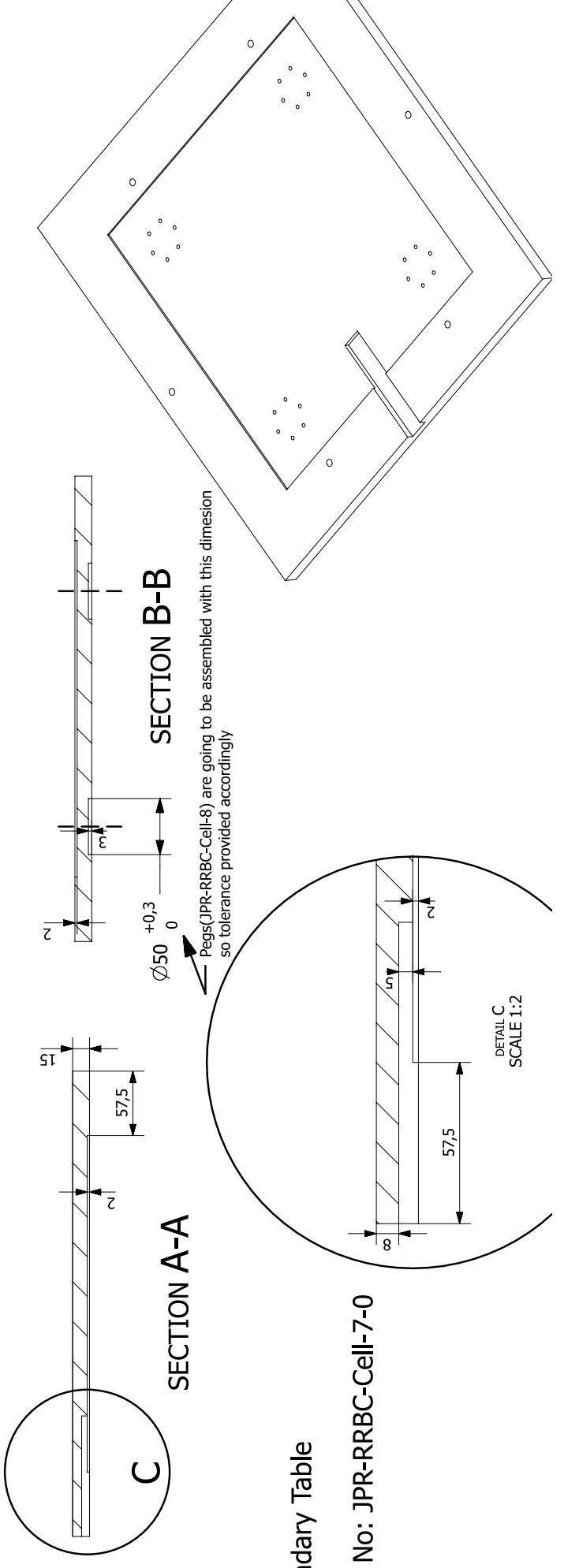
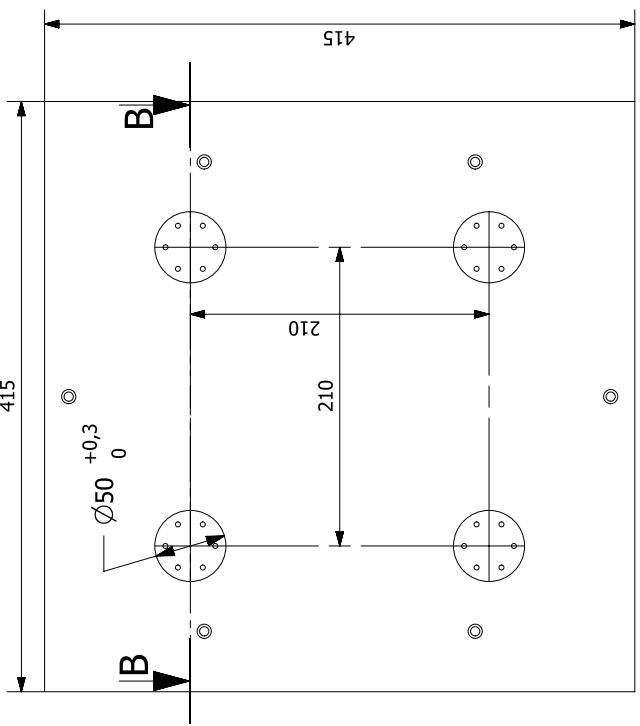
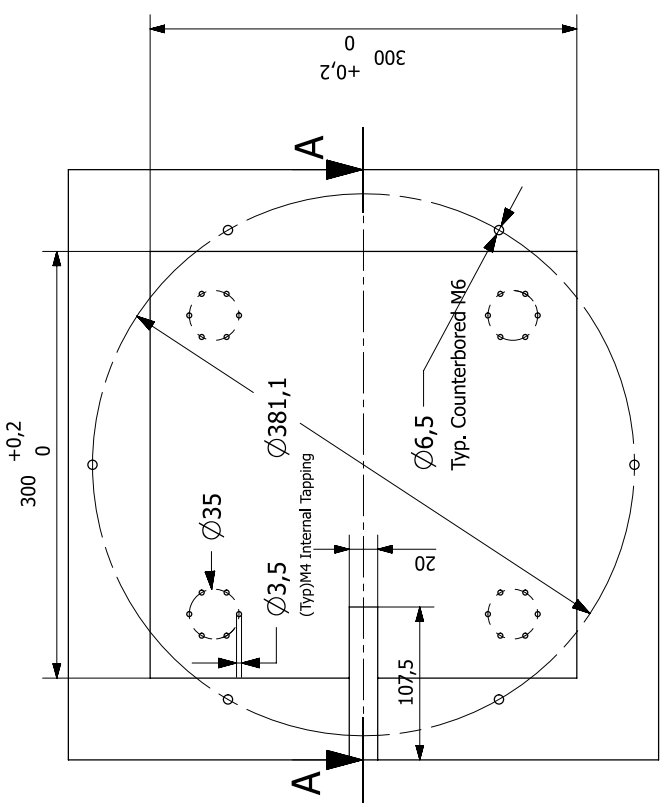
Inner Insulation (Side)

Material: Hylam

DWG No: JPR-RRBC-Cell-6-4

Quantity:2   Sheet 4 of 6

All Dimensions are in mm



Secondary Table

DWG No: JPR-RRBC-Cell-7-0

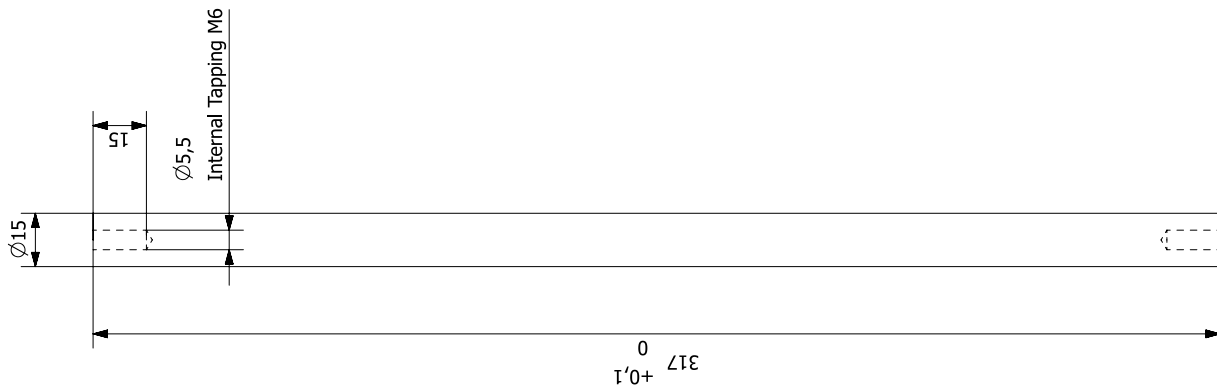
All Dimensions are in mm

Tie Rods

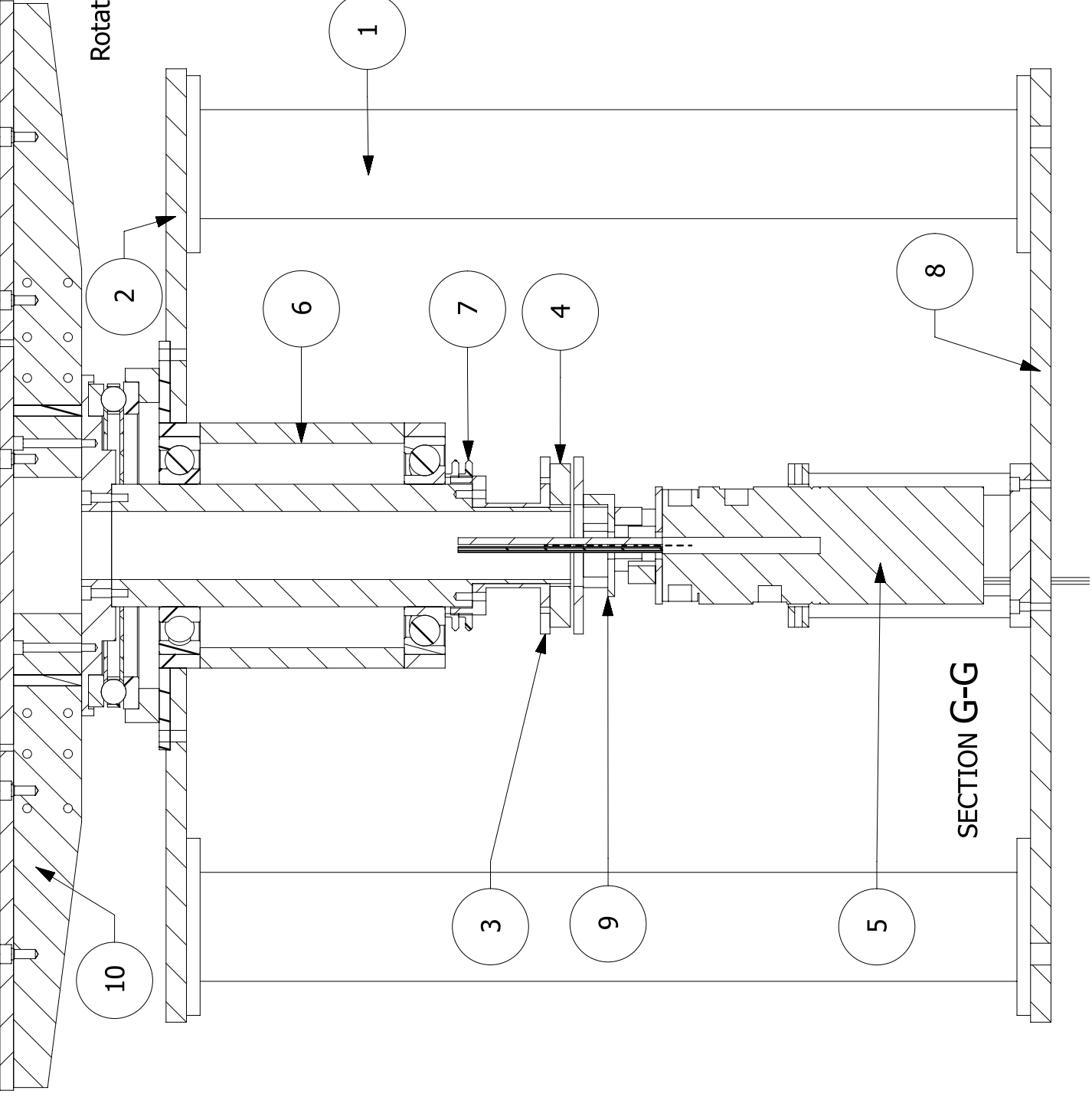
Material: Aluminium-T6061

DWG No: JPR-RRBC-Cell-8-0

Quantity = 6



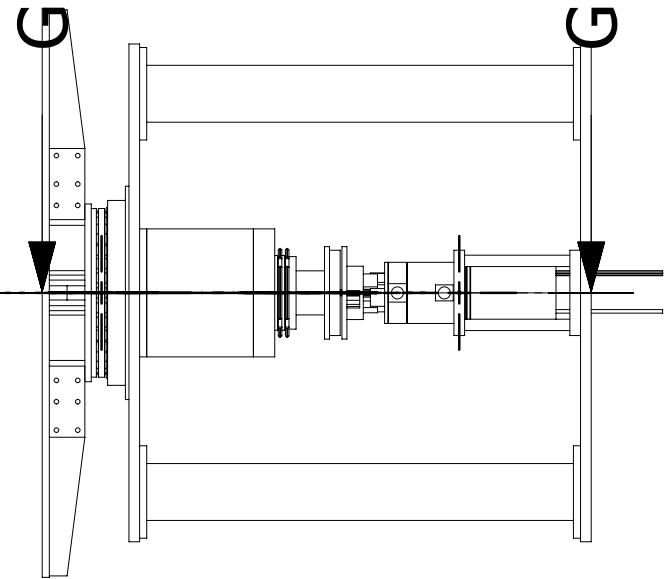


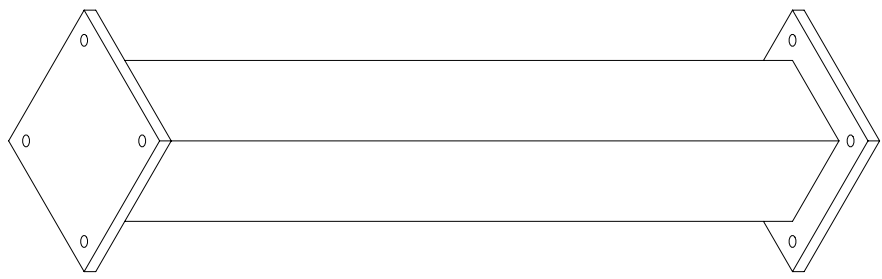


JPR-RRBC-0

Rotating Table for Rayleigh Benard experiment

PC NO	PART NAME	QTY
10	ROTATING TABLE ASSEMBLY	1
9	FLEXIBLE COUPLING	1
8	DATUM	1
7	LOCKNUT	2
6	HOUSING ASSEMBLY	1
5	ROTARY UNION MOUNTING	1
4	PULLEY	1
3	PULLEY FLANGE	1
2	NON ROTATING TABLE	1
1	PILLARS	4





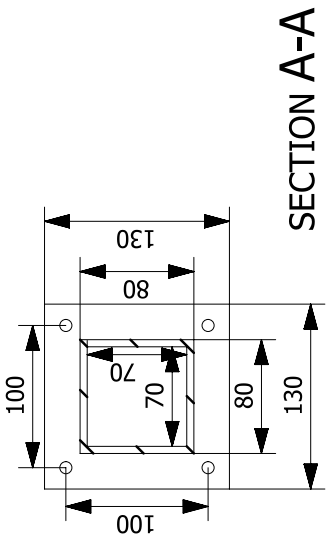
All dimensions are in mm

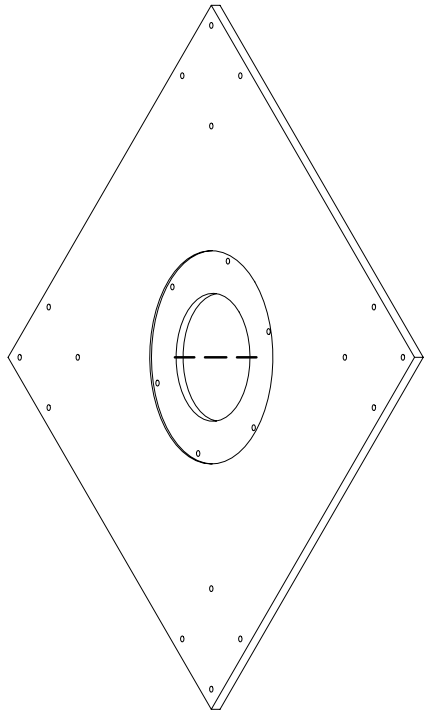
A  
A

620

Part Name: Pillars

Material: Mild Steel DWG No: JPR-RRBC-1-0



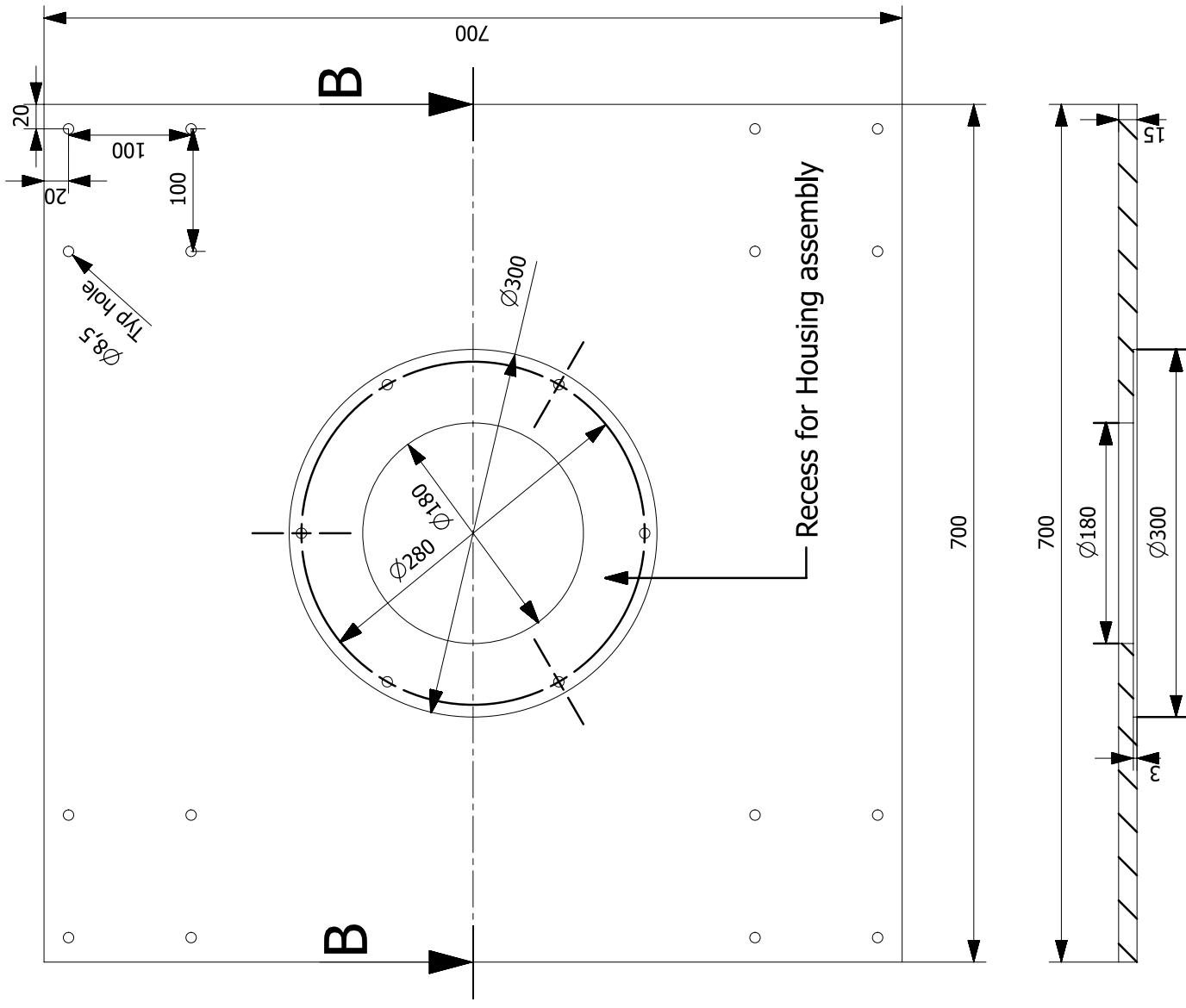


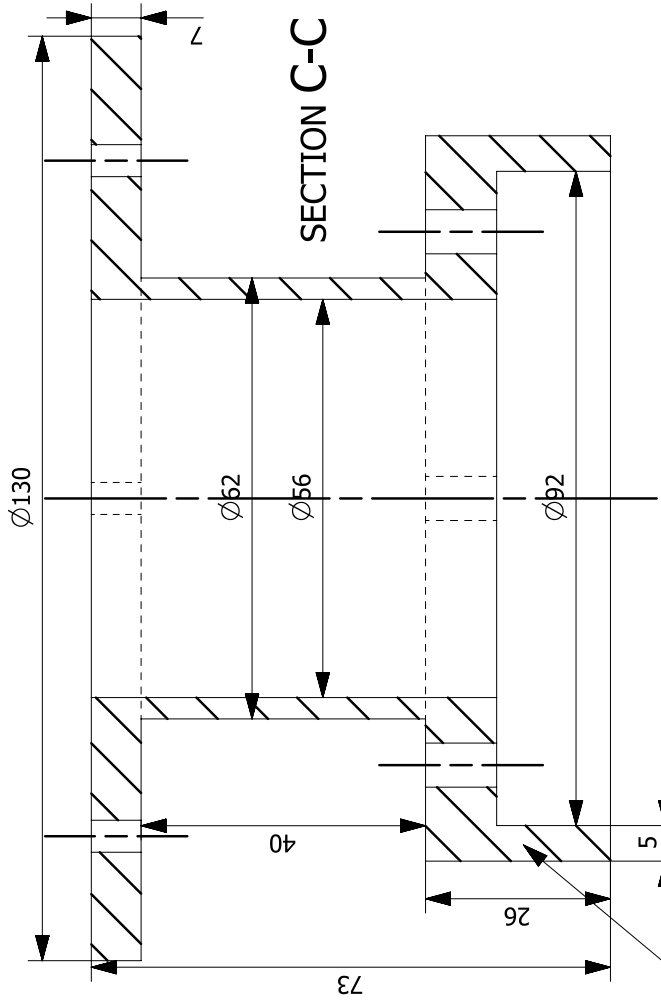
All Sharp edges and Corners should be Rounded off

All dimensions are in mm

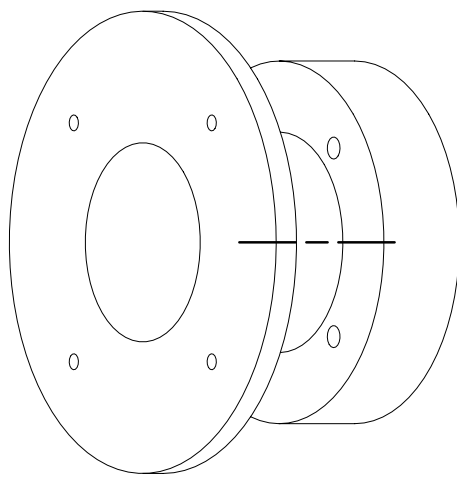
Part Name : Non Rotating Table

Material: Mild Steel DWG No: JPR-RRBC-2-0

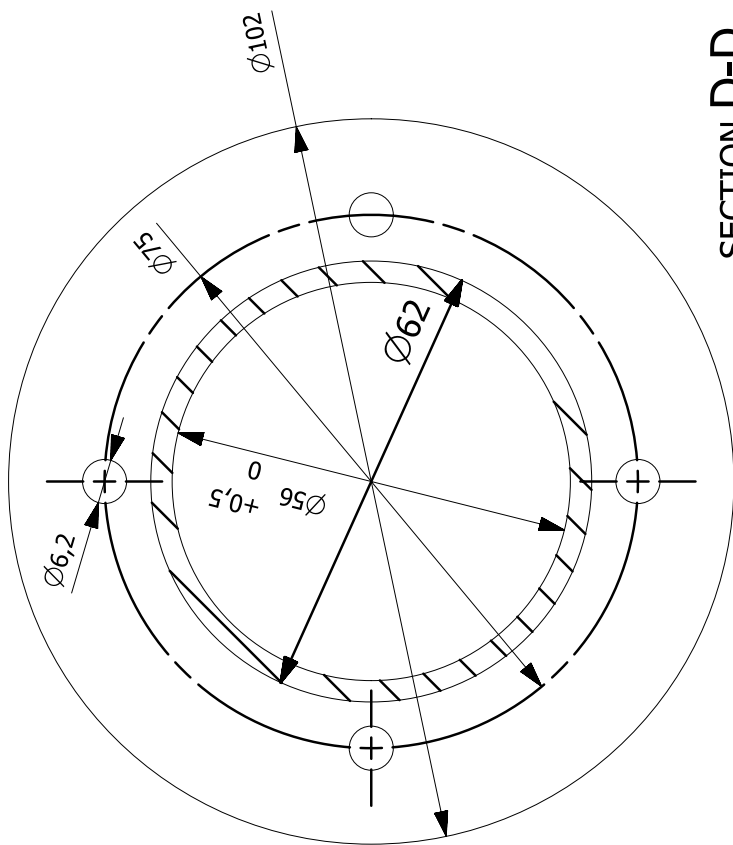
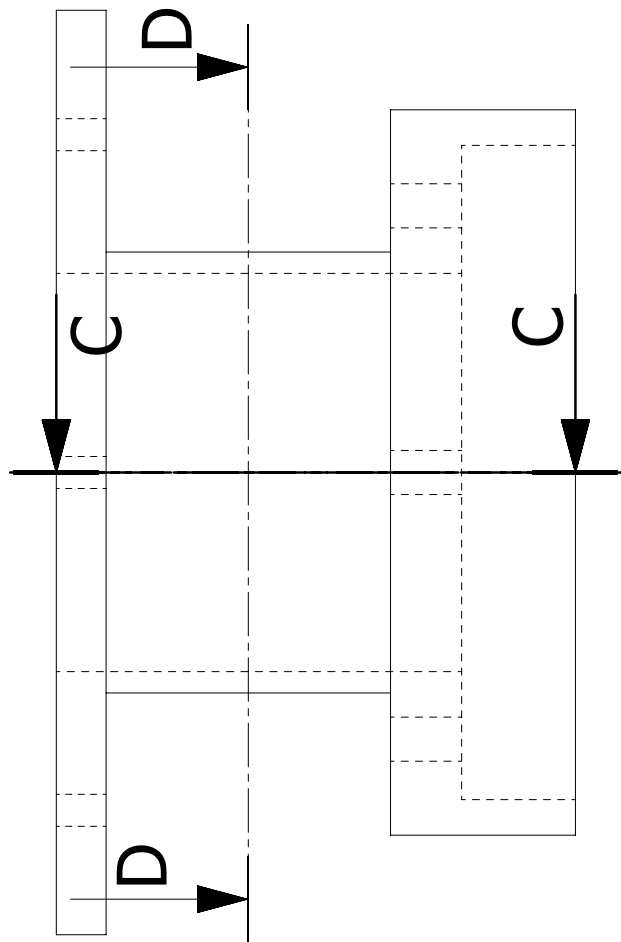




All Sharp Edges and corners should be rounded off



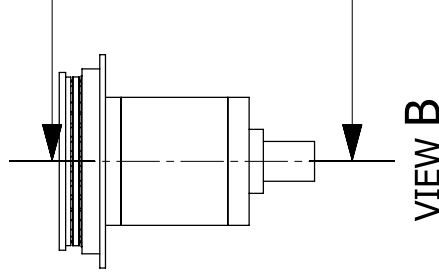
Part Name: Pulley Flange  
DWG No: JPR-RRBC-3  
Material: Mild Steel



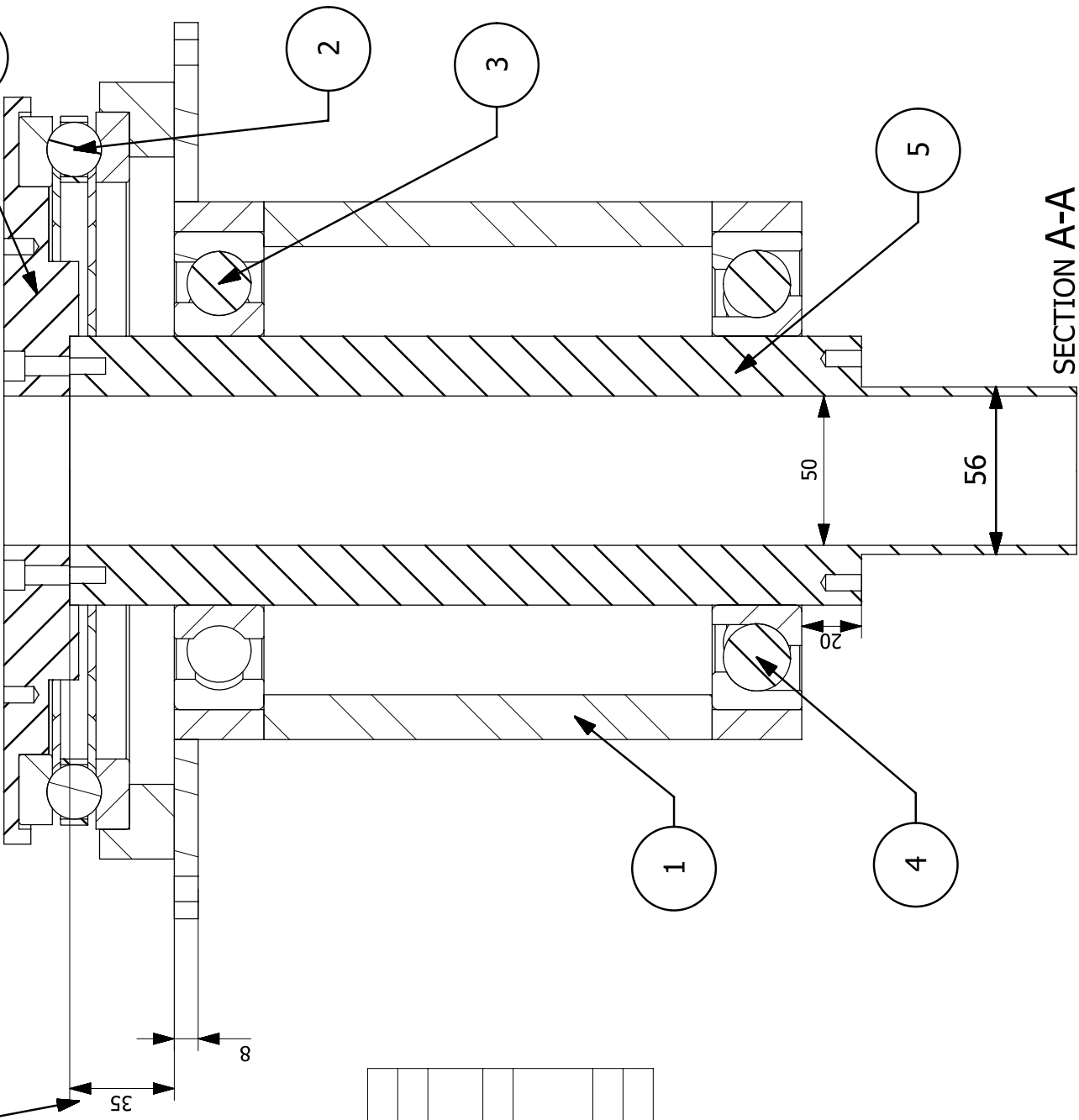
**SECTION D-D**

Distance of Shaft surface from housing flange,  
This is Important parameter and should be maintained as specified

A



A



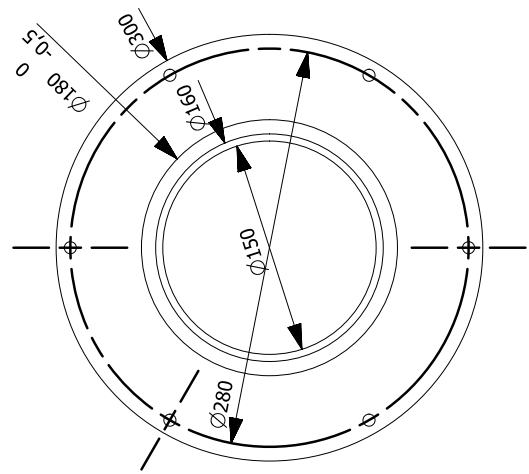
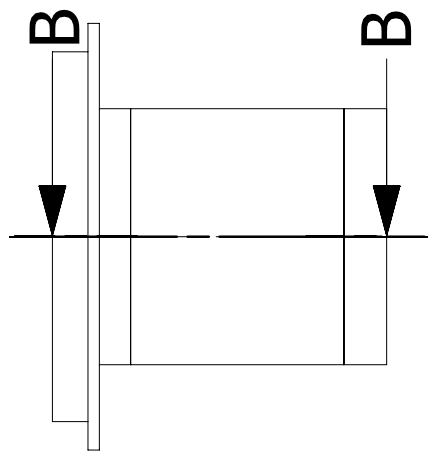
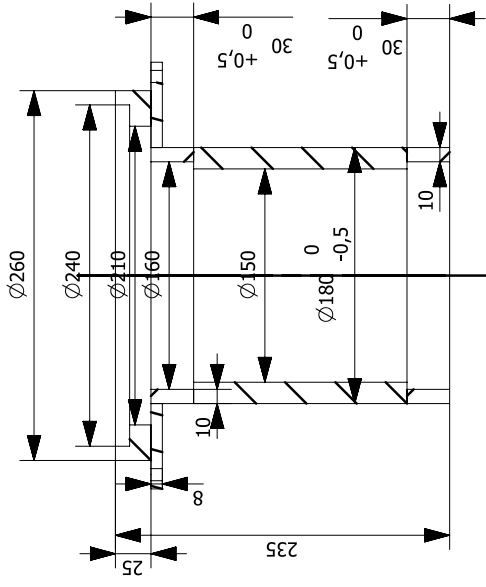
6	FLANGE	1
5	SHAFT	1
4	ANGULARCONTACT_BEARING 7218_BEGAM	1
3	BALL BEARINGS_6218	1
2	THRUST BALL BEARING_51138_MID1900 D240	1
1	HOUSING	1
PC NO	PART NAME	QTY

Part Name : Housing Assembly

Sheet No: 6 of 0

DWG No: JPR-RRBC-6-0

SECTION A-A

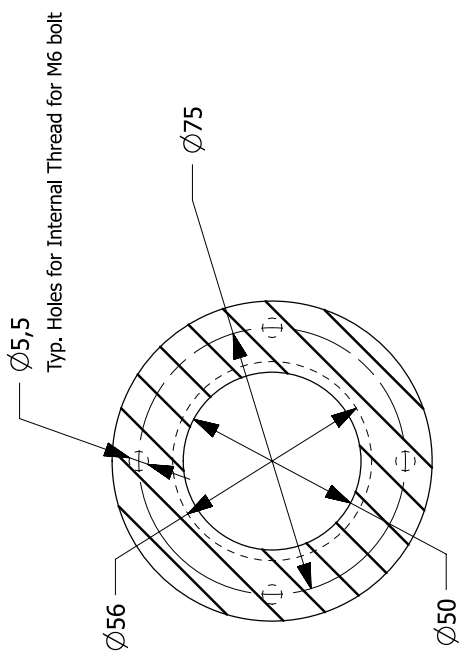
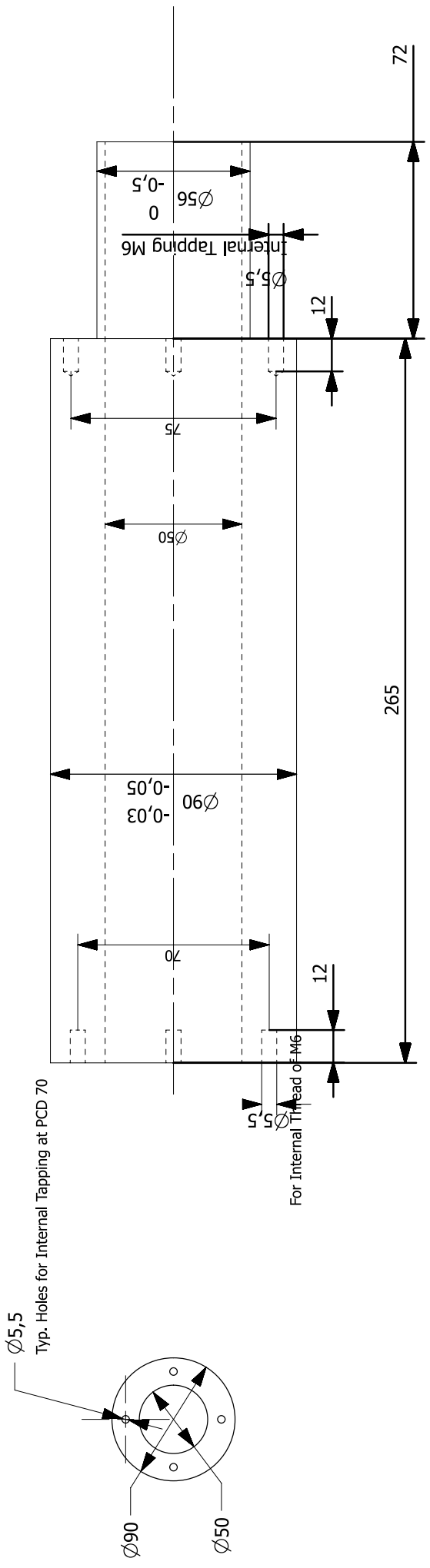


All Sharp Edges and corners should be rounded off with R1

All Dimension are in mm

Part Name: Housing      Material: Mild Steel

Sheet: 1 of 6      DWG No: JPR-RRBC-9-1



All Dimension are in mm

**DETAIL B**

All Dimensions are in mm

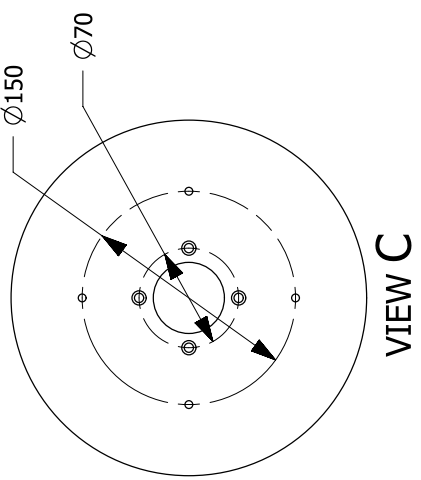
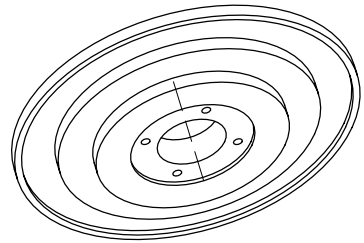
## Material: Mild steel

Part Name: Flange

Sheet 6 of 6 DWG No: JPR-RRBC-6-6

Tolerance Should be maintained as per supplied bearing

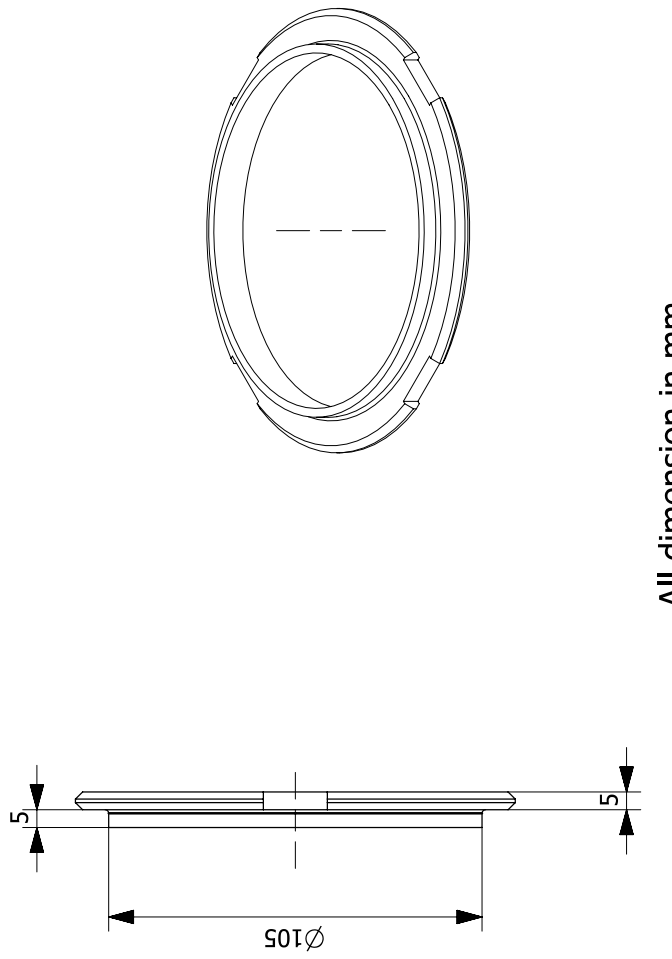
VIEW D



VIEW C

## SECTION A-A

The diagram illustrates a technical drawing with two views labeled A-A and B-B. View A-A shows a cross-sectional view of a rectangular part with a central vertical slot. View B-B shows a top-down view of the same part, highlighting a circular feature. Two arrows point from the labels A and B to their respective views.



All Sharp Edges and corners should be rounded off

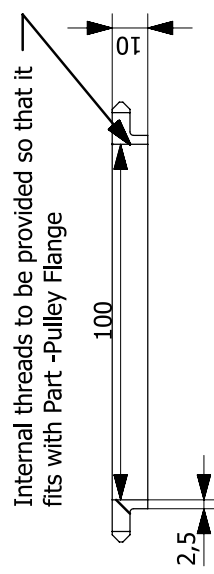
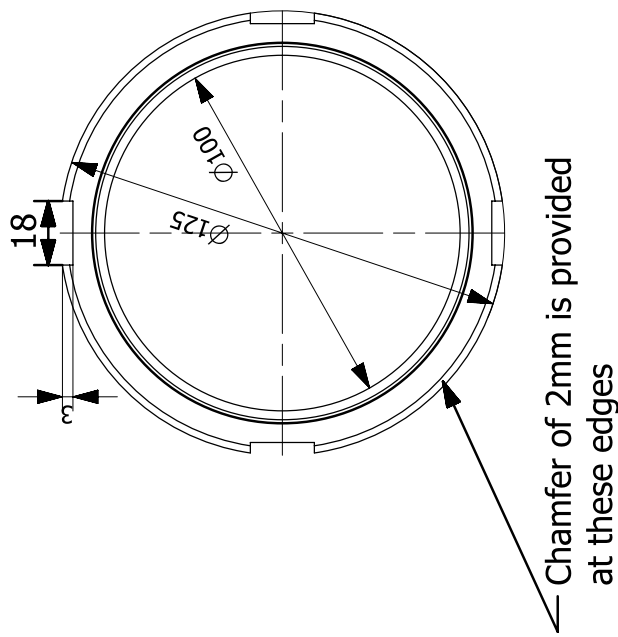
Part Name: LockNut

Quantity: 2

Material: Mild steel

Sheet 10 of 0

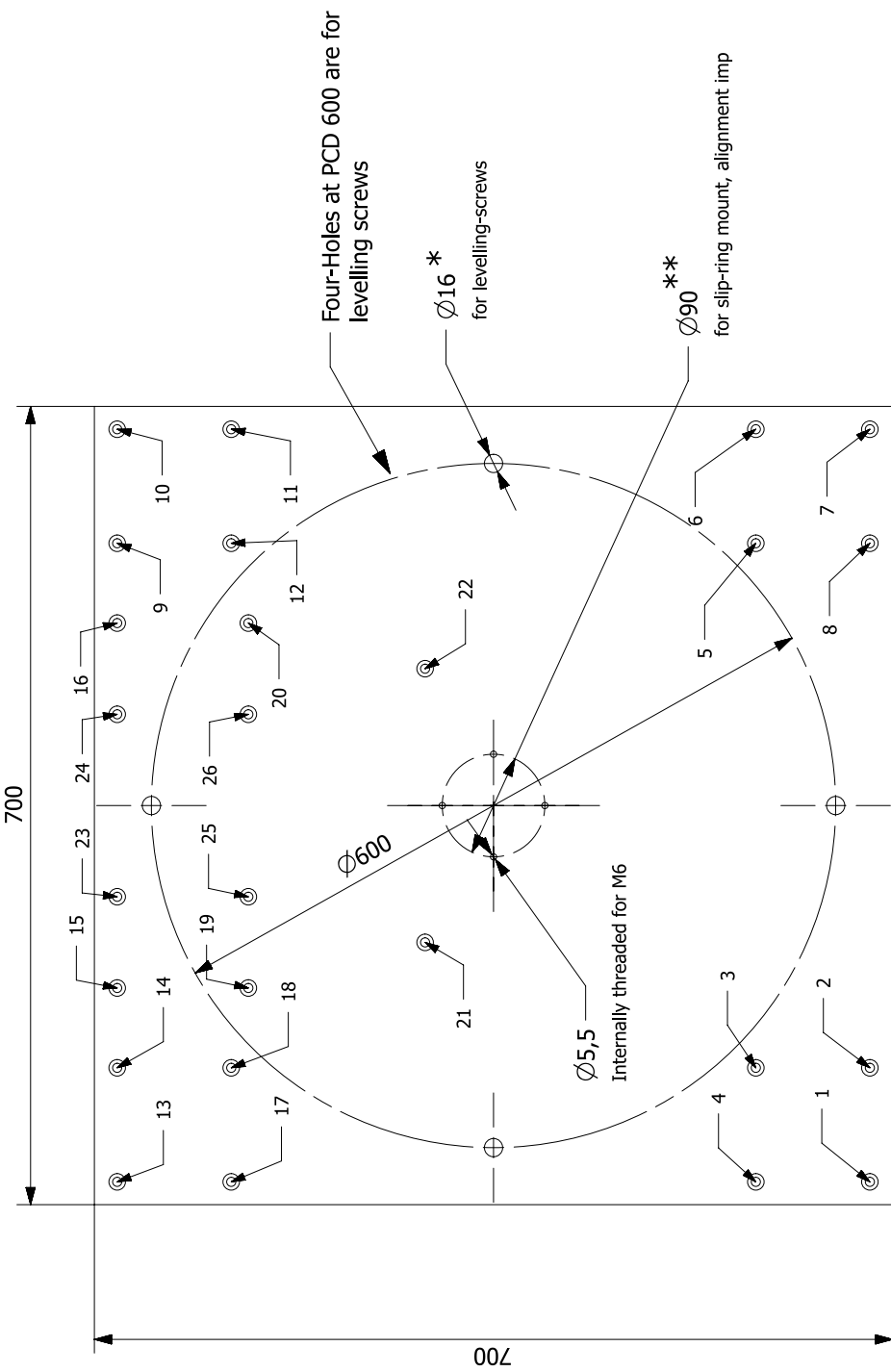
DWG No: JPR-RRBC-10



DETAIL B

HOLE TABLE: Bottom@5

HOLE No.	X	Y	Z
Part : Base_datum - Body : 1			
Counterbore $\varnothing 8.00$ / $\varnothing 14.50$ T8.00			
1	20.00	20.00	8.00
2	120.00	20.00	8.00
3	120.00	120.00	8.00
4	20.00	120.00	8.00
5	580.00	120.00	8.00
6	680.00	120.00	8.00
7	680.00	20.00	8.00
8	580.00	20.00	8.00
9	580.00	680.00	8.00
10	680.00	680.00	8.00
11	680.00	580.00	8.00
12	580.00	580.00	8.00
13	20.00	680.00	8.00
14	120.00	680.00	8.00
15	190.00	680.00	8.00
16	510.00	680.00	8.00
17	20.00	580.00	8.00
18	120.00	580.00	8.00
19	190.00	565.00	8.00
20	510.00	565.00	8.00
21	230.00	410.00	8.00
22	470.00	410.00	8.00
23	270.00	680.00	8.00
24	430.00	680.00	8.00
25	270.00	565.00	8.00
26	430.00	565.00	8.00



→ This Corner Point is Origin Reference for Hole Table

Note:

\* Levelling Screw holes are already drilled, only resting metal pockets left.

\*\*Slip ring mount to be centrally aligned. So they can be drilled on-site during assembly

Part Name: Datum

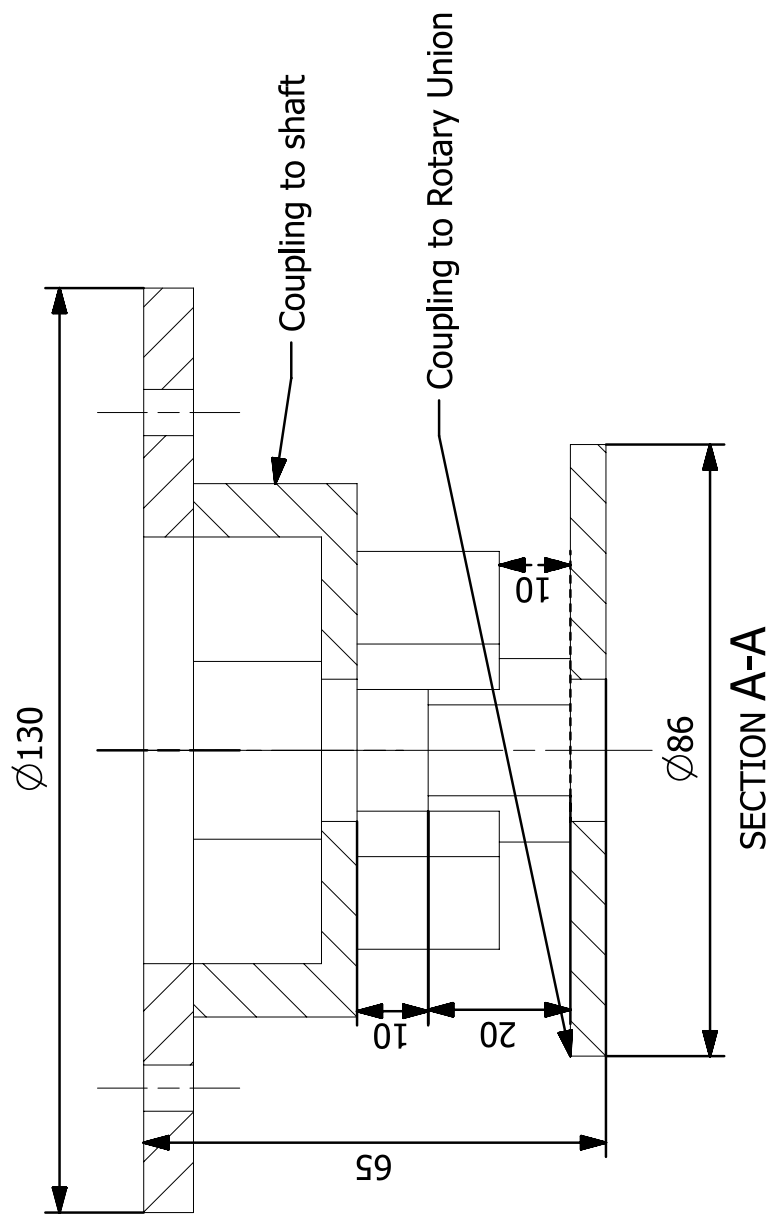
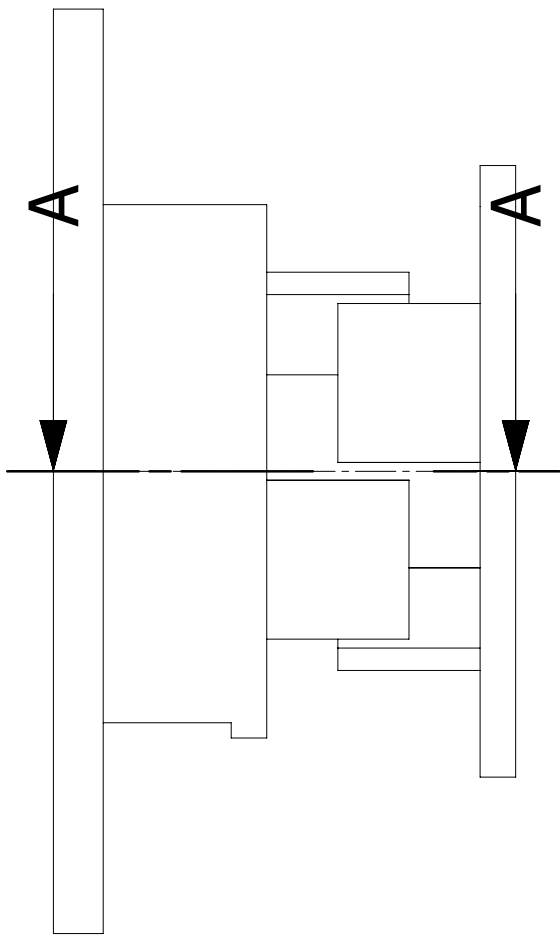
DWG No: JPR-RRBC-8-0

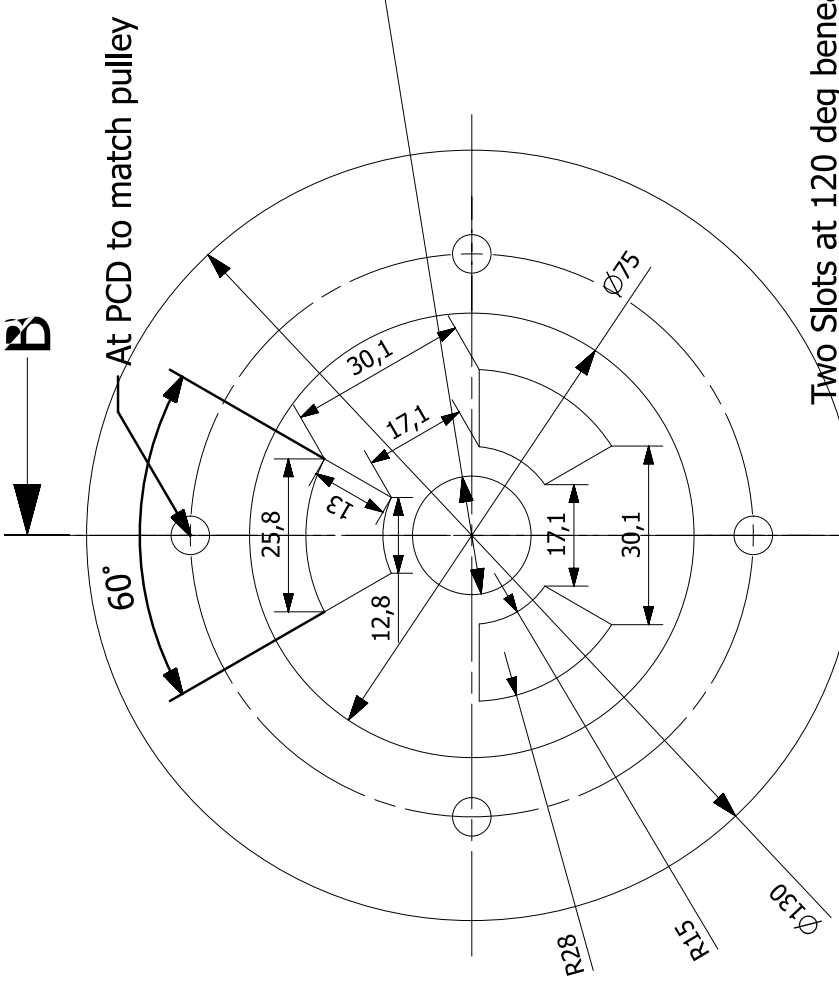
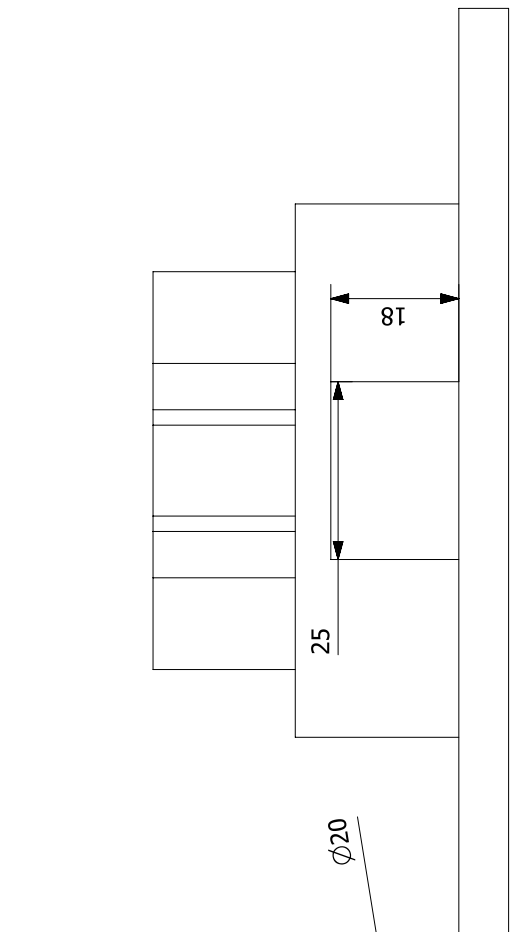
Part Name: Datum

Part Name: Coupling  
Quantity: 1

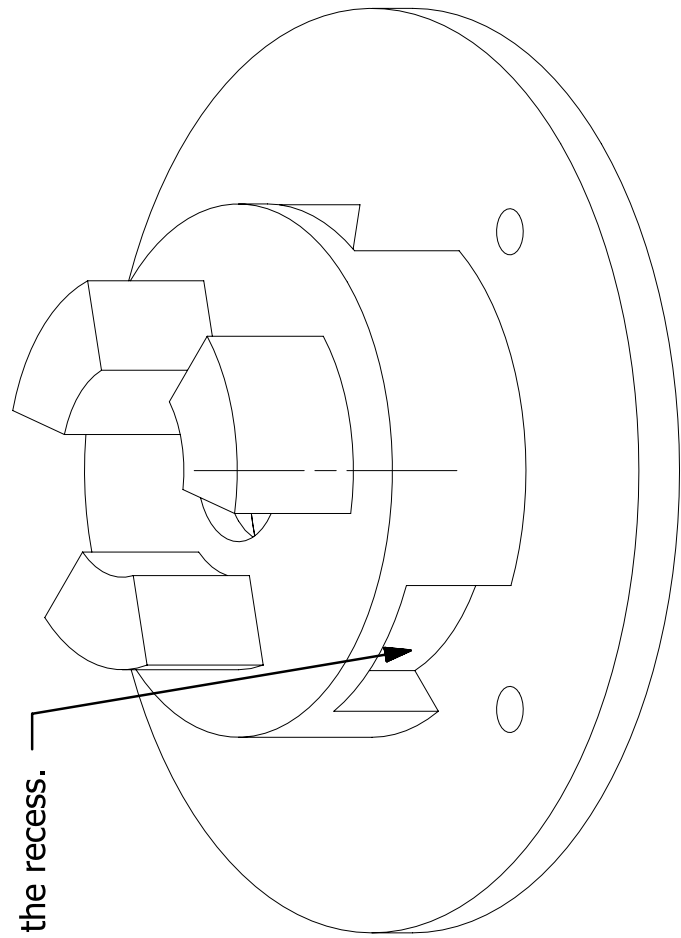
Material: Mild steel

DWG No: JPR-RRBC-9-0



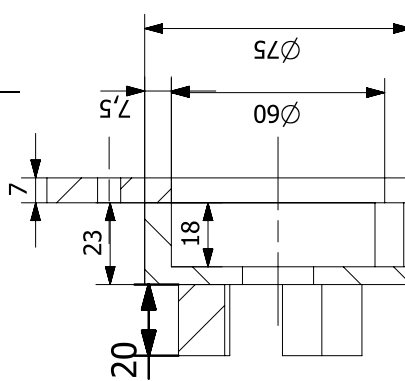


DWG No: JPR-RRBC-9-1

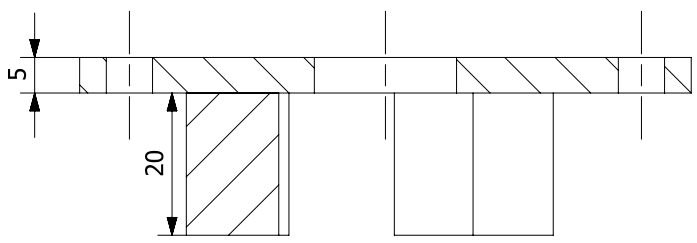
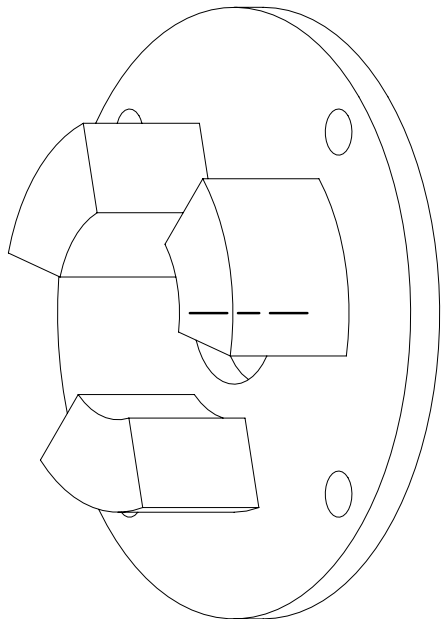


Two Slots at 120 deg beneath the recess.

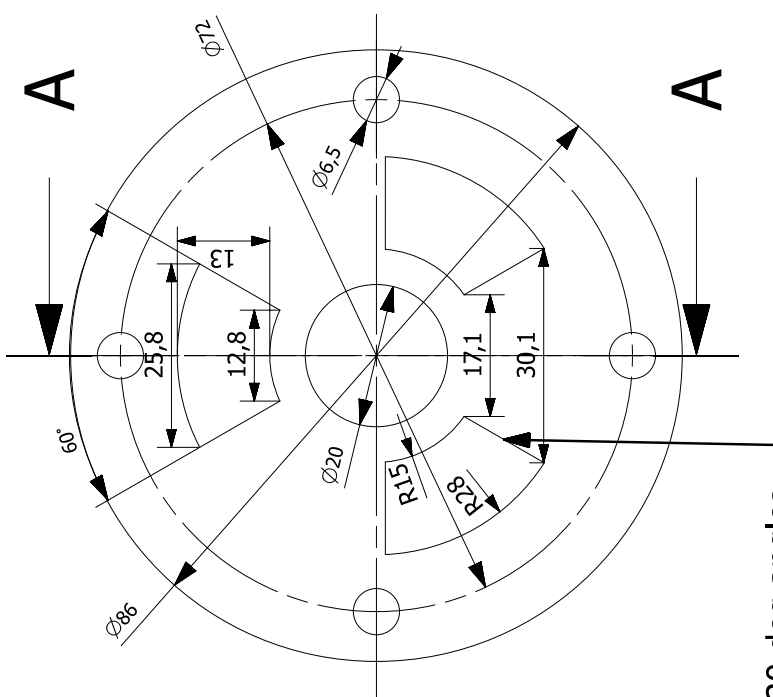
B



SECTION B-B



SECTION A-A

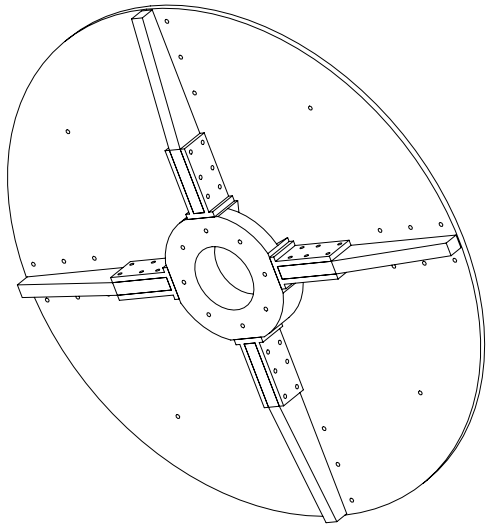


Teeths at 120 deg angles—

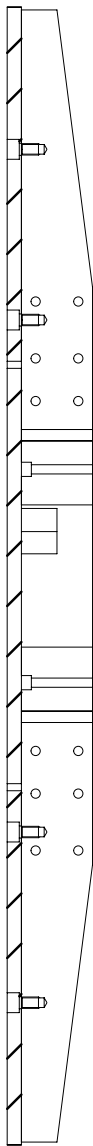
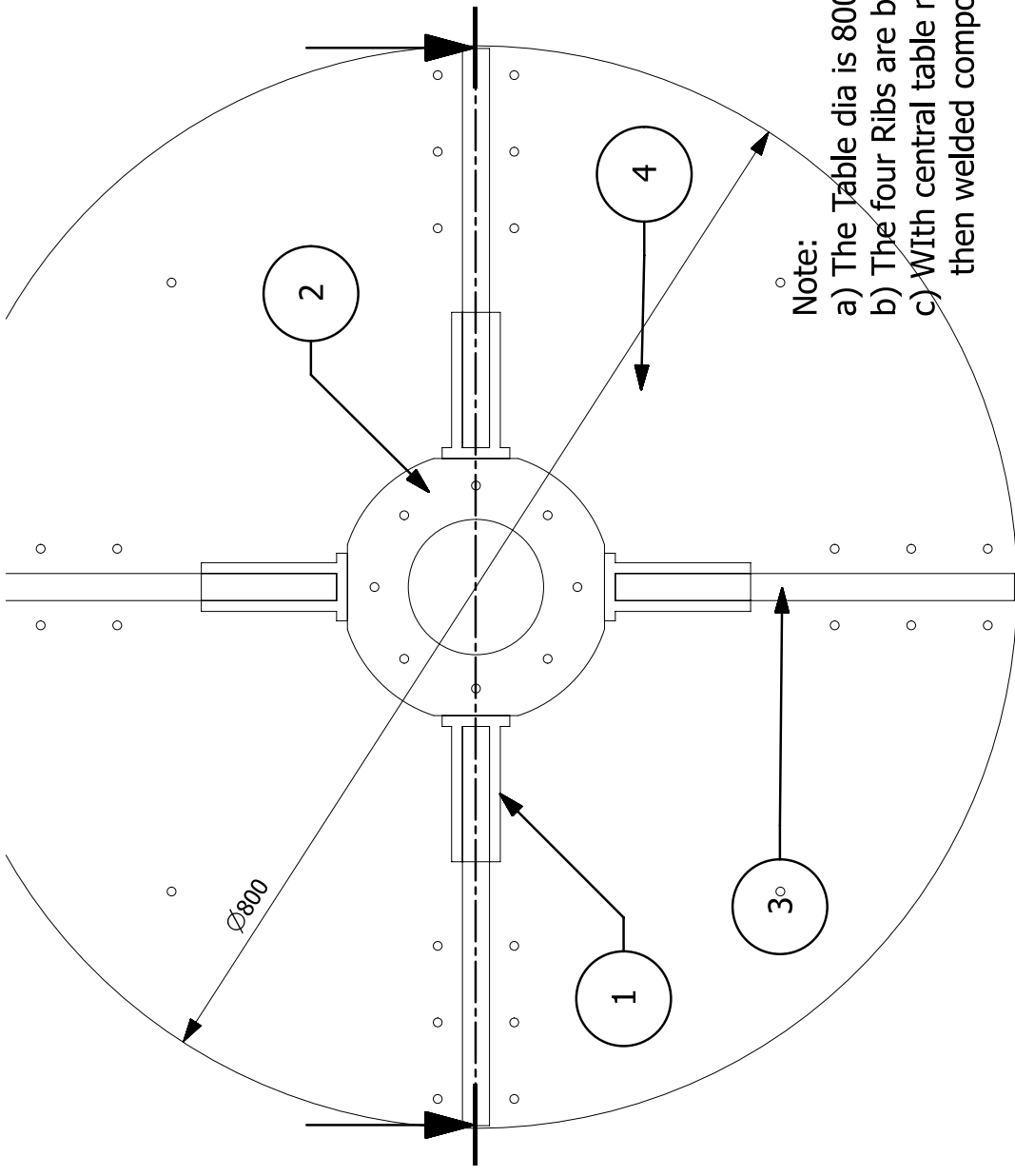
Name: Coupling to RU  
Material: MS (EN8)  
All dimensions in mm

DWG No: JPR-RRBC-9-2

Sheet: 2 of 9



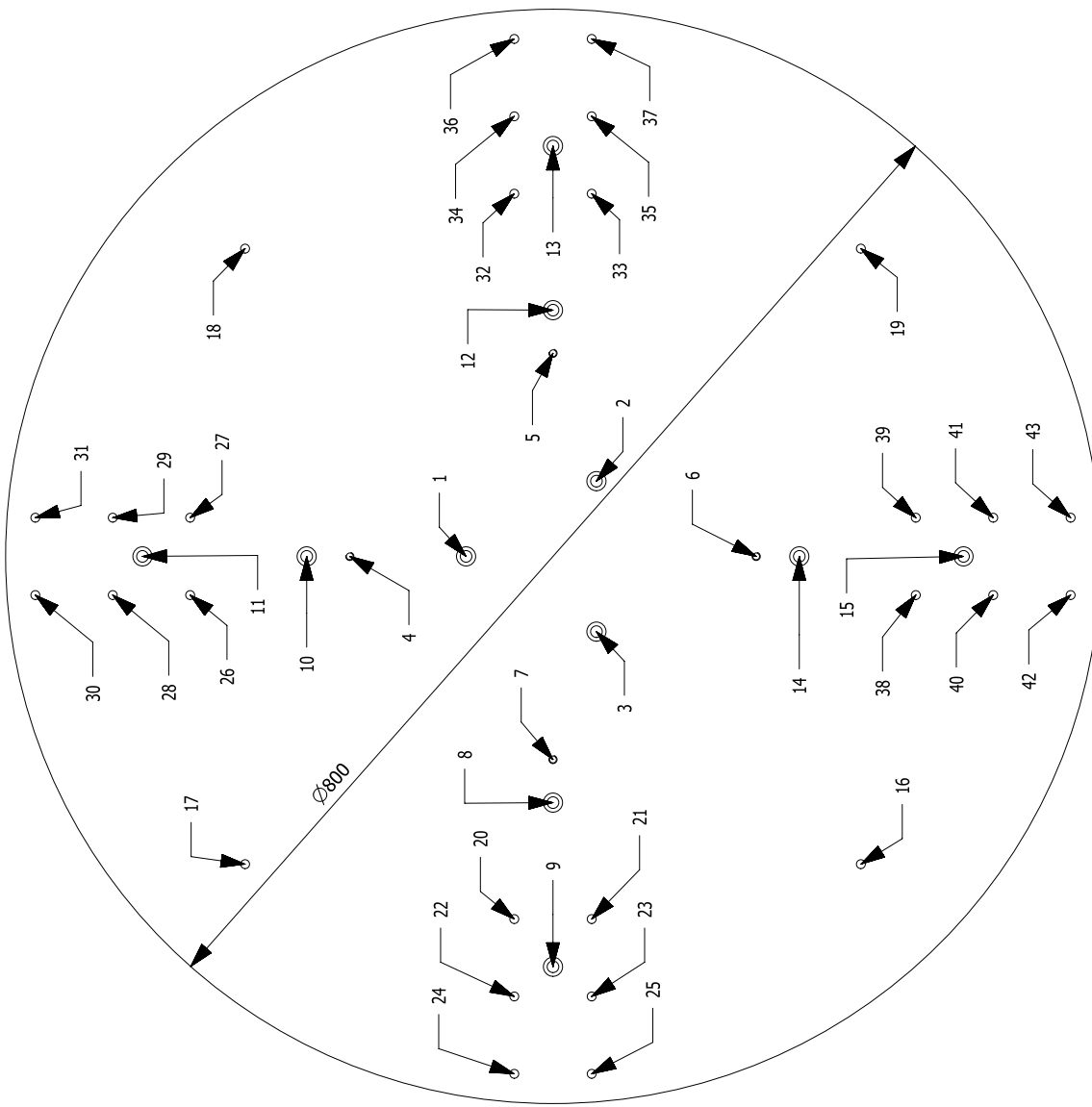
Part No	Name	Material
4	Rotating Table	Aluminium
3	Ribs	Aluminium
2	Table Neck(Spyder)	Mild Steel
1	Holder(Tongs)	Mild Steel



Part Name: Rotating Table Assembly

DWG No: JPR-RRBC-10-0

HOLE No.		X	Y	Z
Part : Rotating Table - Body : 1 Thread Hole M6_x_1.0 Thread_L10.00				
4	-	148.49	148.49	-
5	148.49	-	148.49	-
6	-	148.49	-	-
7	148.49	-	-	-
Through Hole Ø6.50				
16	225.00	225.00	-	-
17	225.00	225.00	-	-
18	225.00	225.00	-	-
19	225.00	225.00	-	-
20	265.15	28.28	-	-
21	265.15	28.28	-	-
22	321.72	28.28	-	-
23	321.72	28.28	-	-
24	378.28	28.28	-	-
25	378.28	28.28	-	-
26	28.28	265.15	-	-
27	28.28	265.15	-	-
28	28.28	321.72	-	-
29	28.28	321.72	-	-
30	28.28	378.28	-	-
31	28.28	378.28	-	-
32	265.15	28.28	-	-
33	265.15	28.28	-	-
34	321.72	28.28	-	-
35	321.72	28.28	-	-
36	378.28	28.28	-	-
37	378.28	28.28	-	-
38	28.28	265.15	-	-
39	28.28	265.15	-	-
40	28.28	321.72	-	-
41	28.28	321.72	-	-
42	28.28	378.28	-	-
43	28.28	378.28	-	-
Counterbore Ø8.50 / Ø14.00 18.50				
1	-	63.51	-8.50	-
2	55.00	31.75	-8.50	-
3	55.00	31.75	-8.50	-
8	180.00	-	-8.50	-
9	300.00	-	-8.50	-
10	-	180.00	-8.50	-
11	-	300.00	-8.50	-
12	180.00	-	-8.50	-
13	300.00	-	-8.50	-
14	-	180.00	-8.50	-
15	-	300.00	-8.50	-

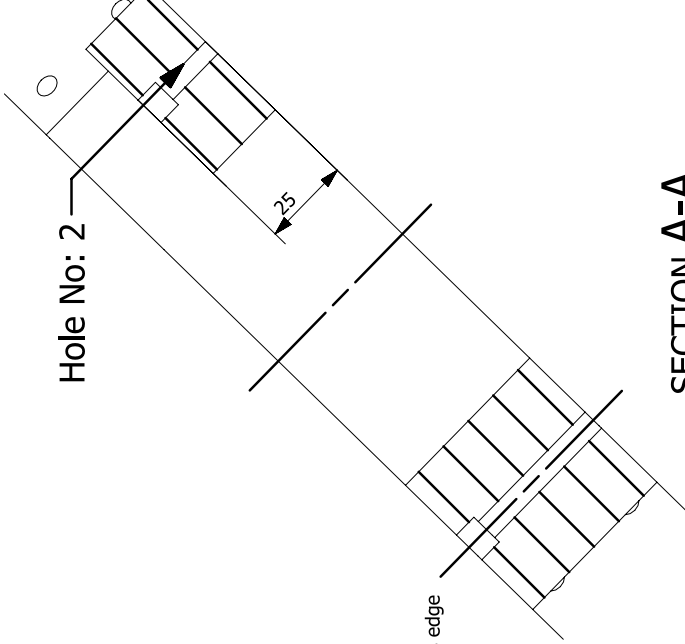


Part Name: Rotating Table

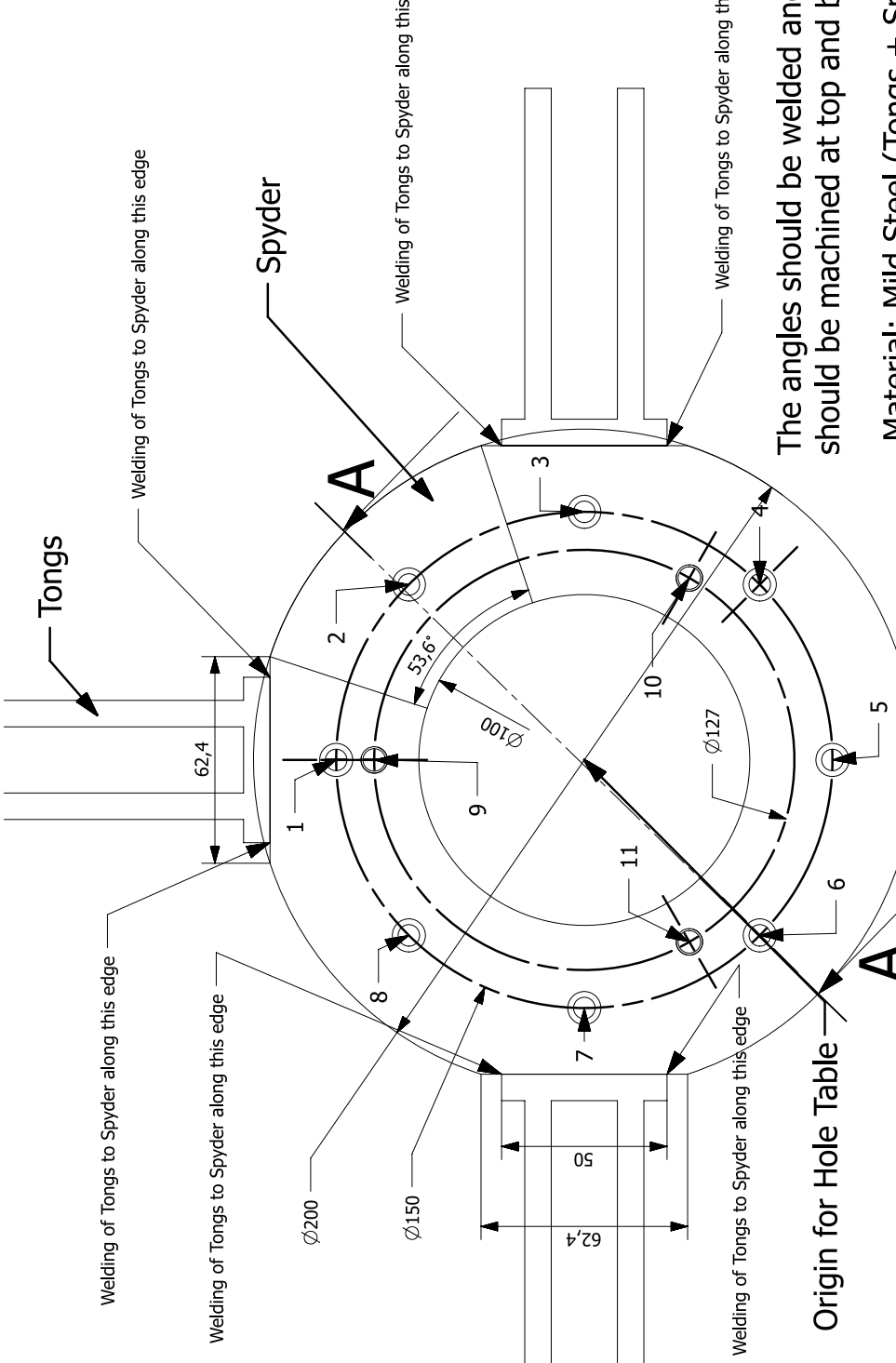
DWG No: JPR-RRBC-10-4

Material: Aluminium 6061-T6

Both Sides of Table should have flatness within  
200 microns



**SECTION A-A**



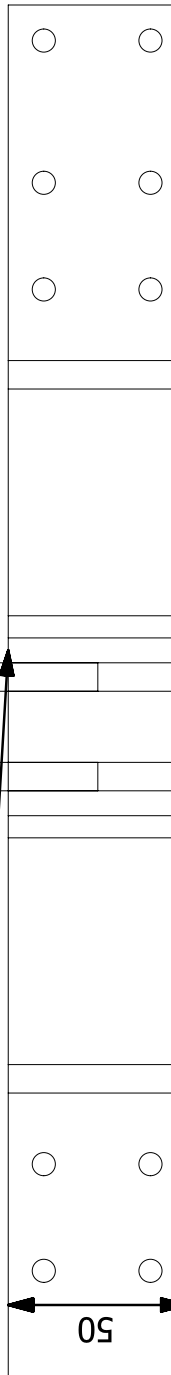
The angles should be welded and then component  
should be machined at top and bottom surface to get planarity.

Origin for Hole Table

Material: Mild Steel (Tongs + Spyder)  
Part Name: Spyder( Table Neck)

DWG No: JPR-RRBC-10-2

—This surface planarity to be maintained, should be machined after welding.



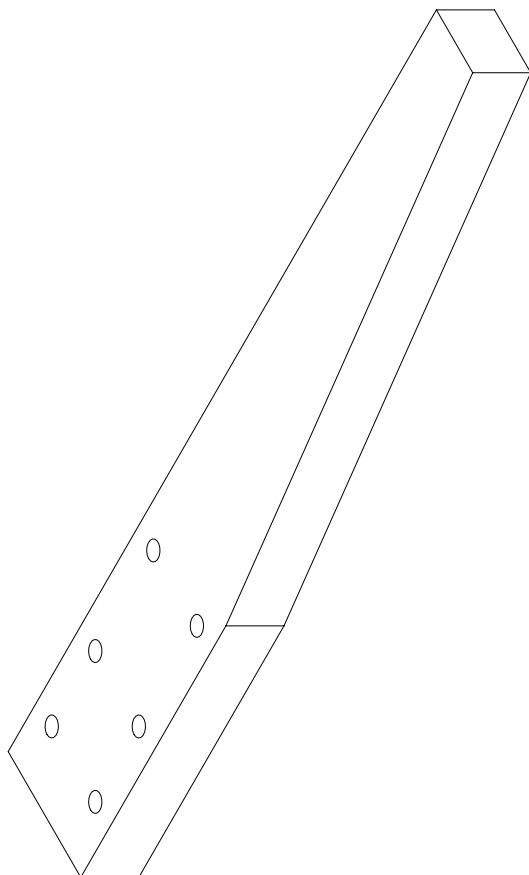
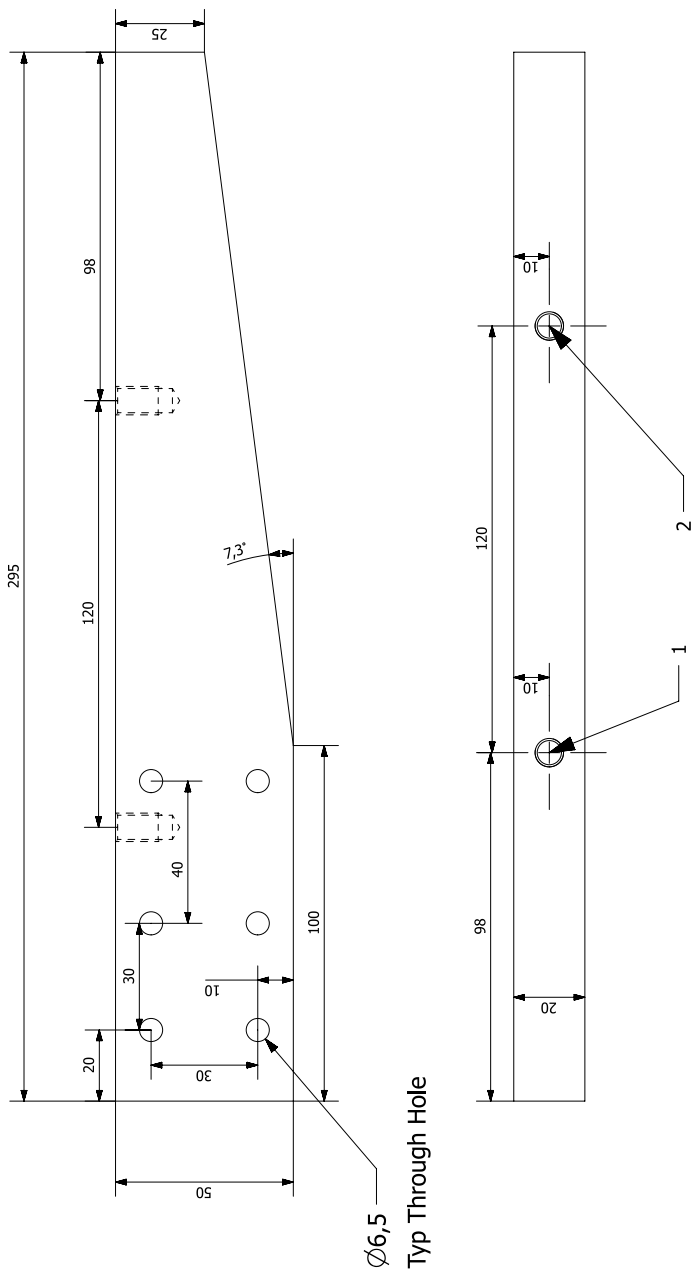
—This surface planarity to be maintained, should be machined after welding.

Part Name: Ribs

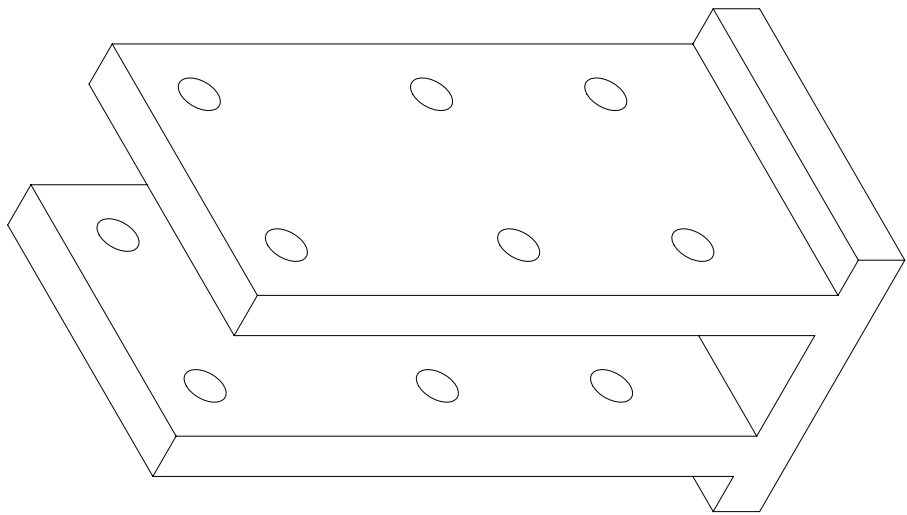
DWG No: JPR-RRBC-10-3

Qty: 4

Material: Aluminium 6061-T6



HOLE TABLE: Back@4			
HOLE No.	X	Y	Z
Part : Ribs - Body : 1			
Thread Hole M8_X_1.25 Thread_L12.60 / Ø8.00 T0.60			
1	98.00	-	-0.60
2	218.00	-	-0.60

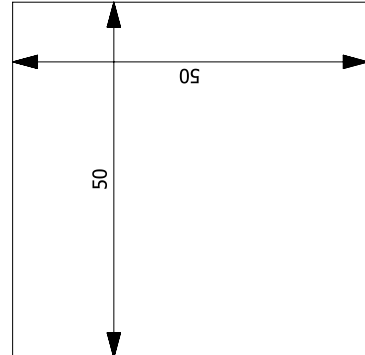
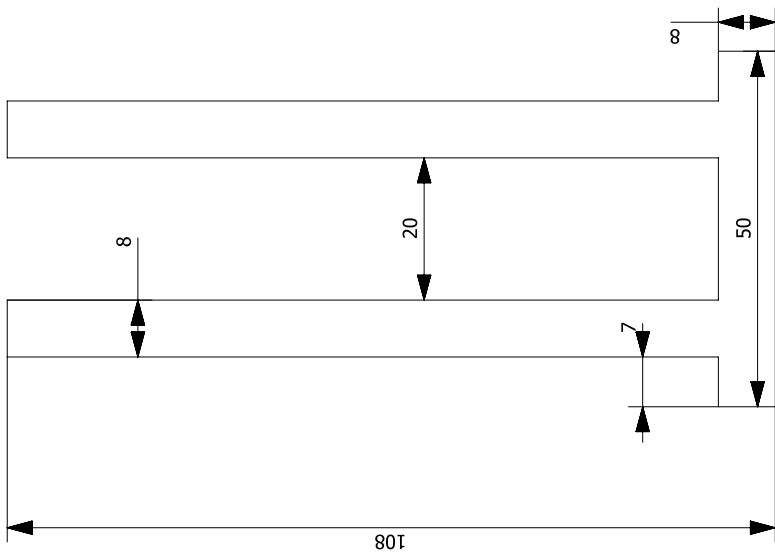
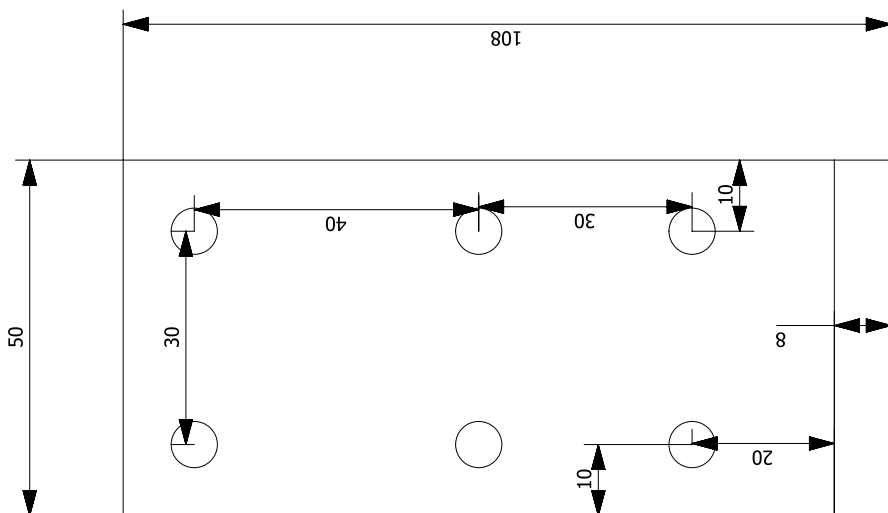


Part Name: Ribs Holder( Tongs)

DWG No: JPRRRBC-10-1

Material: Mild Steel

To be welded to spyder JPR-RRBC-10-2



## Appendix B

# Numerical simulations

### B.1 Free Slip Boundary Condition

For comparison, we also include the results for free-slip boundary conditions. We impose free-slip boundary condition on the walls at  $x = 0$  and  $x = 1$  while retaining no-slip boundary condition on the other walls. Moreover, we use the same parameters as in RC2. Figure B.1 shows there is negligible helicity generation for free-slip BCs. To explain it, we present Fig. B.2. Due to the absence of Ekman pumping in free-slip BC,  $V_x$ ,  $\omega_y$ , and  $\omega_z$  are not generated, and hence all the constituents of helicity become zero.

### B.2 Grid Independence

To ensure that our results are independent of grid size, we have also performed simulations using  $N = 256$  grid points for the same parameters. In Fig B.3, continuous ( $N = 128$ ) and the corresponding dot-dashed ( $N = 256$ ) lines are overlapping each other, showing that all the spatial scales present in our simulations are fully resolved for the grid  $N = 128$ .

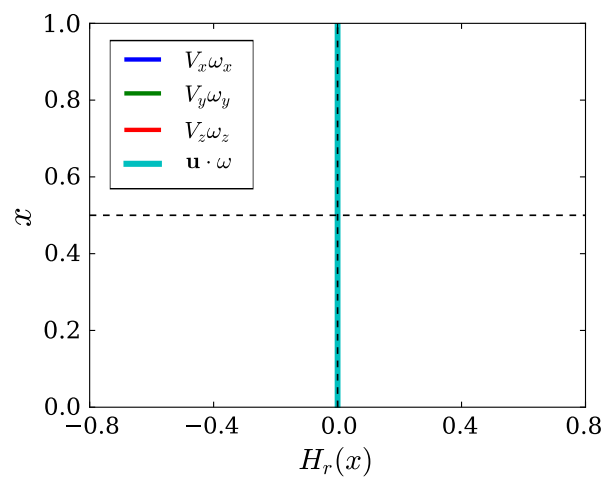


Figure B.1: Variation of the constituents of helicity normalized by maximum possible helicity  $|\mathbf{u}||\boldsymbol{\omega}|$  and averaged in  $yz$ -plane ( $H_r$ ) with  $x$  for free-slip boundary conditions on the walls perpendicular to the rotation vector.

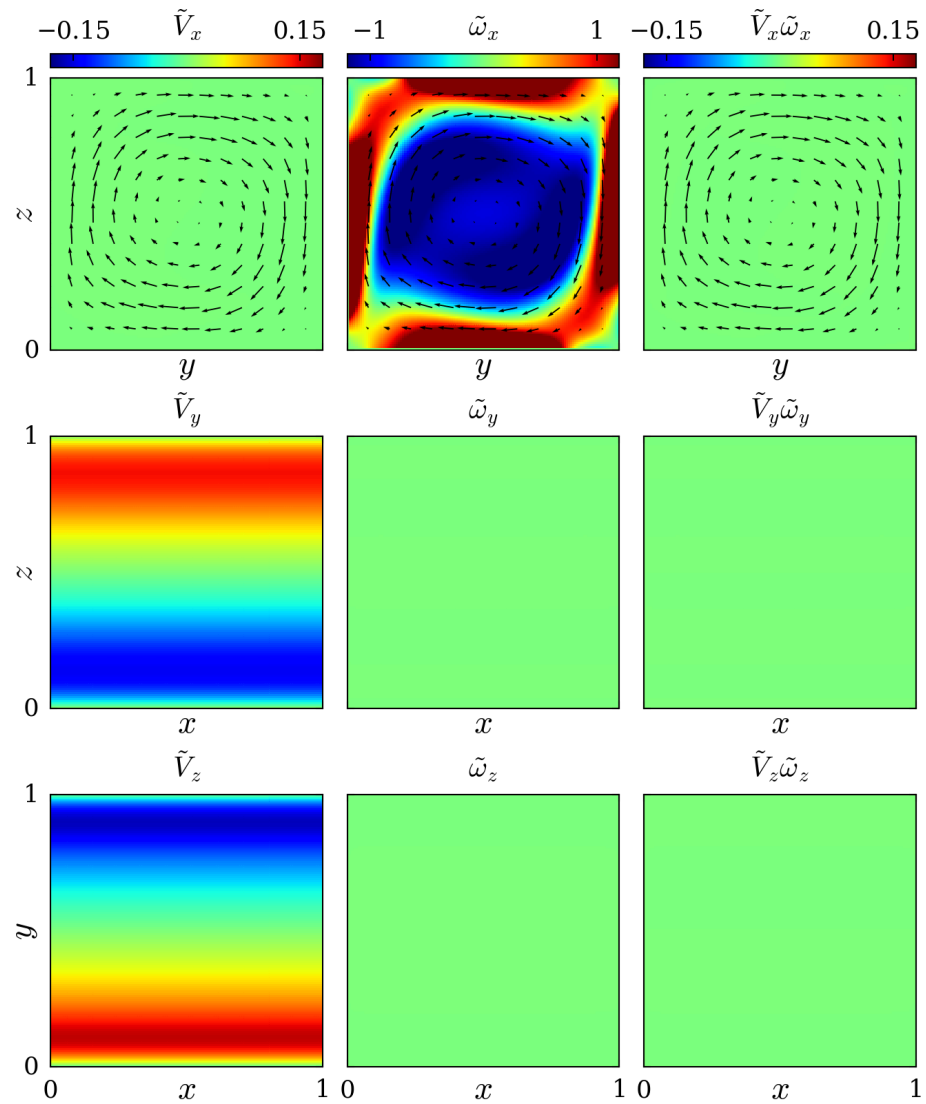


Figure B.2: Contour plots of normalized (by their rms values)  $V_x$ ,  $\omega_x$ , and  $V_x\omega_x$  in  $yz$ -plane at  $x = 0.05$  (first row),  $V_y$ ,  $\omega_y$ , and  $V_y\omega_y$  in  $xz$ -plane at  $y = 0.5$  (second row), and  $V_z$ ,  $\omega_z$ , and  $V_z\omega_z$  in  $xy$ -plane at  $z = 0.5$  (third row) for free-slip BCs on walls perpendicular to the rotation vector ( $x$  direction).

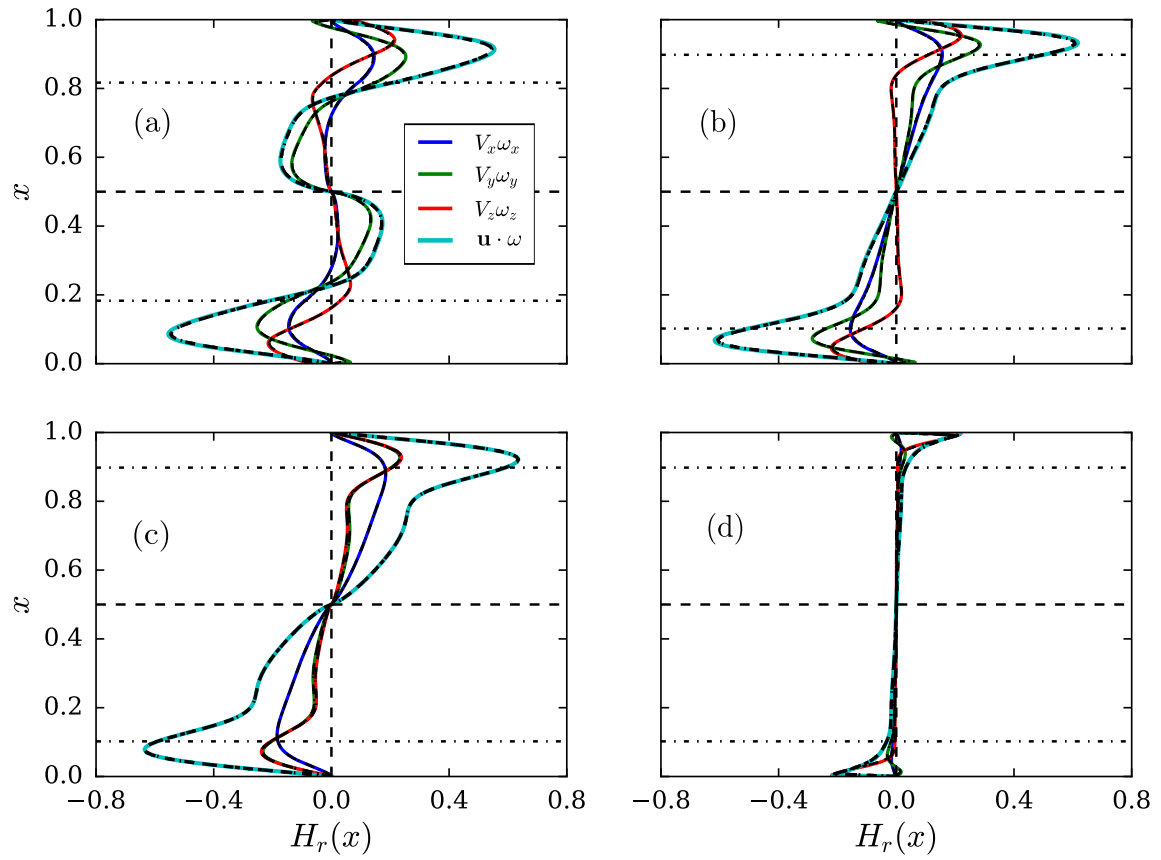


Figure B.3: Variation of the constituents of helicity normalized by maximum possible helicity  $|\mathbf{u}||\boldsymbol{\omega}|$  and averaged in  $yz$ -plane ( $H_r$ ) with  $x$  for (a) RC1, (b) RC2, (c) RH, and (d) RCS. Continuous and dot-dashed lines represent results with  $N = 128$  and  $N = 256$ , respectively.

# References

- [1] Giovanni Zocchi, Elisha Moses, and Albert Libchaber. Coherent structures in turbulent convection, an experimental study. *Physica A: Statistical Mechanics and its Applications*, 166(3):387–407, 1990.
- [2] Y-B Du and Penger Tong. Turbulent thermal convection in a cell with ordered rough boundaries. *Journal of Fluid Mechanics*, 407:57–84, 2000.
- [3] Richard Stevens, Herman Clercx, and D. Lohse. Heat transport and flow structure in rotating rayleigh-bénard convection. *European Journal of Mechanics - B/Fluids*, 40, 07 2013. doi: 10.1016/j.euromechflu.2013.01.004.
- [4] Yuanming Liu and Robert E Ecke. Heat transport measurements in turbulent rotating rayleigh-bénard convection. *Physical Review E*, 80(3):036314, 2009.
- [5] Jonathan S Cheng, Stephan Stellmach, Adolfo Ribeiro, Alexander Grannan, Eric M King, and Jonathan M Aurnou. Laboratory-numerical models of rapidly rotating convection in planetary cores. *Geophysical Journal International*, 201(1):1–17, 2015.
- [6] Richard JAM Stevens, Herman JH Clercx, and Detlef Lohse. Optimal prandtl number for heat transfer in rotating rayleigh–bénard convection. *New journal of physics*, 12(7): 075005, 2010.
- [7] Jin-Qiang Zhong, Richard JAM Stevens, Herman JH Clercx, Roberto Verzicco, Detlef Lohse, and Guenter Ahlers. Prandtl-, rayleigh-, and rossby-number dependence of heat transport in turbulent rotating rayleigh-bénard convection. *Physical review letters*, 102(4):044502, 2009.

- [8] Pranav Joshi, Hadi Rajaei, Rudie PJ Kunnen, and Herman JH Clercx. Heat transfer in rotating rayleigh–bénard convection with rough plates. *Journal of Fluid Mechanics*, 830, 2017.
- [9] N. Schaeffer, D. Jault, Henri-Claude Nataf, and A. Fournier. Turbulent geodynamo simulations: a leap towards Earth’s core. *Geophys. J. Int.*, 211:1–29, 2017.
- [10] A Ranjan, P A Davidson, U R Christensen, and J Wicht. On the generation and segregation of helicity in geodynamo simulations. *Geophysical Journal International*, 221:741–757, May 2020.
- [11] Hadi Rajaei, Pranav Joshi, Kim M. J. Alards, Rudie P. J. Kunnen, Federico Toschi, and Herman J. H. Clercx. Transitions in turbulent rotating convection: A lagrangian perspective. *Phys. Rev. E*, 93:043129, April 2016.
- [12] Mahendra K. Verma. *Physics of Buoyant Flows: From Instabilities to Turbulence*. World Scientific, Singapore, 2018.
- [13] Leo P Kadanoff. Turbulent heat flow: structures and scaling. *Physics today*, 54(8):34–39, 2001.
- [14] Marcello Lappa. *Thermal convection: Patterns, Evolution and Stability*. Wiley, Chichester, 2010.
- [15] Quan Zhou, Chao Sun, and Ke-Qing Xia. Morphological evolution of thermal plumes in turbulent rayleigh–bénard convection. *Physical review letters*, 98(7):074501, 2007.
- [16] Heng-Dong Xi, Siu Lam, and Ke-Qing Xia. From laminar plumes to organized flows: the onset of large-scale circulation in turbulent thermal convection. *Journal of Fluid Mechanics*, 503:47–56, 2004.
- [17] JJ Niemela, L Skrbek, KR Sreenivasan, and RJ Donnelly. Turbulent convection at very high rayleigh numbers. *Nature*, 404(6780):837–840, 2000.
- [18] J-C Tisserand, Mathieu Creysse, Yoann Gasteuil, Hervé Pabiou, Mathieu Gibert, Bernard Castaing, and Francesca Chillà. Comparison between rough and smooth plates within the same rayleigh–bénard cell. *Physics of Fluids*, 23(1):015105, 2011.

- [19] Sebastian Wagner and Olga Shishkina. Heat flux enhancement by regular surface roughness in turbulent thermal convection. *Journal of Fluid Mechanics*, 763:109–135, 2015.
- [20] Julien Salort, Olivier Liot, Eleonore Rusaouen, Fanny Seychelles, J-C Tisserand, Mathieu Creyssels, Bernard Castaing, and Francesca Chillà. Thermal boundary layer near roughnesses in turbulent rayleigh-bénard convection: Flow structure and multistability. *Physics of Fluids*, 26(1):015112, 2014.
- [21] Ping Wei, Tak Shing Chan, Rui Ni, Xiao Zheng Zhao, and Ke Qing Xia. Heat transport properties of plates with smooth and rough surfaces in turbulent thermal convection. *Journal of Fluid Mechanics*, 740:28–46, 2014.
- [22] Y Shen, Penger Tong, and K-Q Xia. Turbulent convection over rough surfaces. *Physical review letters*, 76(6):908, 1996.
- [23] TY Chu and Richard J Goldstein. Turbulent convection in a horizontal layer of water. *Journal of Fluid Mechanics*, 60(1):141–159, 1973.
- [24] X-L Qiu, K-Q Xia, and P Tong. Experimental study of velocity boundary layer near a rough conducting surface in turbulent natural convection. *Journal of Turbulence*, (6):N30, 2005.
- [25] G Stringano, G Pascazio, and R Verzicco. Turbulent thermal convection over grooved plates. *Journal of Fluid Mechanics*, 557:307–336, 2006.
- [26] Y-B Du and P Tong. Enhanced heat transport in turbulent convection over a rough surface. *Physical review letters*, 81(5):987, 1998.
- [27] Emmanuel Villermaux. Transfer at rough sheared interfaces. *Physical review letters*, 81(22):4859, 1998.
- [28] Chao Sun, Yin-Har Cheung, and Ke-Qing Xia. Experimental studies of the viscous boundary layer properties in turbulent rayleigh–bénard convection. *Journal of Fluid Mechanics*, 605:79–113, 2008.

- [29] Francesca Chilla and Joerg Schumacher. New perspectives in turbulent rayleigh-bénard convection. *The European Physical Journal E*, 35(7):58, 2012.
- [30] Andrew Belmonte, Andreas Tilgner, and Albert Libchaber. Temperature and velocity boundary layers in turbulent convection. *Physical Review E*, 50(1):269, 1994.
- [31] Subrahmanyam Chandrasekhar. *Hydrodynamic and Hydromagnetic Stability*. Oxford University Press, Oxford, 2013.
- [32] H. T. Rossby. A study of Bénard convection with and without rotation. *J. Fluid Mech.*, 36:309–335, January 1969.
- [33] Jin-Qiang Zhong and Guenter Ahlers. Heat transport and the large-scale circulation in rotating turbulent rayleigh–bénard convection. *Journal of fluid mechanics*, 665:300–333, 2010.
- [34] Richard JAM Stevens, Jin-Qiang Zhong, Herman JH Clercx, Guenter Ahlers, and Detlef Lohse. Transitions between turbulent states in rotating rayleigh-bénard convection. *Physical review letters*, 103(2):024503, 2009.
- [35] RPJ Kunnen, HJH Clercx, and Bernardus J Geurts. Breakdown of large-scale circulation in turbulent rotating convection. *EPL (Europhysics Letters)*, 84(2):24001, 2008.
- [36] Hadi Rajaei, Pranav Joshi, Kim MJ Alards, Rudie PJ Kunnen, Federico Toschi, and Herman JH Clercx. Transitions in turbulent rotating convection: A lagrangian perspective. *Physical Review E*, 93(4):043129, 2016.
- [37] Hadi Rajaei, Rudie PJ Kunnen, and Herman JH Clercx. Exploring the geostrophic regime of rapidly rotating convection with experiments. *Physics of Fluids*, 29(4):045105, 2017.
- [38] Stephan Weiss and Guenter Ahlers. The large-scale flow structure in turbulent rotating rayleigh-bénard convection. *Journal of fluid mechanics*, 688:461, 2011.
- [39] Richard JAM Stevens, Herman JH Clercx, and Detlef Lohse. Breakdown of the large-scale circulation in  $\gamma = 1/2$  rotating rayleigh-bénard flow. *Physical Review E*, 86(5):056311, 2012.

- [40] Eric M King, Stephan Stellmach, Jerome Noir, Ulrich Hansen, and Jonathan M Aurnou. Boundary layer control of rotating convection systems. *Nature*, 457(7227):301–304, 2009.
- [41] Eric M King and Jonathan M Aurnou. Thermal evidence for taylor columns in turbulent rotating rayleigh-bénard convection. *Physical Review E*, 85(1):016313, 2012.
- [42] EM King, S Stellmach, and B Buffett. Scaling behaviour in rayleigh–bénard convection with and without rotation. *Journal of Fluid Mechanics*, 717:449–471, 2013.
- [43] Keith Julien, Antonio M Rubio, Ian Grooms, and Edgar Knobloch. Statistical and physical balances in low rossby number rayleigh–bénard convection. *Geophysical & Astrophysical Fluid Dynamics*, 106(4-5):392–428, 2012.
- [44] Rodolfo Ostilla-Mónico, Erwin P van der Poel, Rudie PJ Kunnen, Roberto Verzicco, and Detlef Lohse. Geostrophic convective turbulence: The effect of boundary layers. *Preprint*, 2014.
- [45] JJ Niemela, S Babuin, and KR Sreenivasan. Turbulent rotating convection at high rayleigh and taylor numbers. *Journal of fluid mechanics*, 649:509–522, 2010.
- [46] Bholanath Precision Engineering. Step servo motor 600w. <http://bholanath.in/certificates-files/step-servo-TDS/BHSS-600W-Step-Servo.pdf?200518>. Accessed on 30.11.2021.
- [47] John Essick. *Hands-on introduction to LabVIEW for scientists and engineers*. Oxford University Press, 2013.
- [48] Graham Clifford Goodwin, Stefan F Graebe, Mario E Salgado, et al. *Control system design*, volume 240. Prentice hall New Jersey, 2001.
- [49] National Instruments. Pid algorithms. [https://zone.ni.com/reference/en-XX/help/370401J-01/lvpidmain/pid\\_algs/](https://zone.ni.com/reference/en-XX/help/370401J-01/lvpidmain/pid_algs/). Accessed on 30.11.2021.
- [50] Henry Keith Moffatt. *Magnetic Field Generation in Electrically Conducting Fluids*. Cambridge University Press, Cambridge, 1978.

- [51] Andrew D. Gilbert, Uriel Frisch, and Annick Pouquet. Helicity is unnecessary for alpha effect dynamos, but it helps. *Geophysical and Astrophysical Fluid Dynamics*, 42:151–161, January 1988.
- [52] M. Yu. Reshetnyak. Evolution of helicities in dynamo problems. *Doklady Physics*, 60: 283–287, 2015.
- [53] Franck Plunian, Rodion Stepanov, and Peter Frick. Shell models of magnetohydrodynamic turbulence. *Phys. Rep.*, 523:1–60, 2012.
- [54] H. K. Moffatt and Arkady B. Tsinober. Helicity in laminar and turbulent flow. *Annu. Rev. Fluid Mech.*, 24(1):281–312, January 1992.
- [55] E. Parker. Hydromagnetic dynamo models. *Astrophys. J.*, 122:293–314, 1955.
- [56] Peter Olson, Ulrich Christensen, and Gary A. Glatzmaier. Numerical modeling of the geodynamo: Mechanisms of field generation and equilibration. *Journal of Geophysical Research: Solid Earth*, 104:10383–10404, May 1999.
- [57] P. A. Davidson. The Dynamics and Scaling Laws of Planetary Dynamos Driven by Inertial Waves. *Geophys. J. Int.*, 198(3):1832–1847, February 2014.
- [58] M. Yu. Reshetnyak. Hydrodynamic helicity in boussinesq-type models of the geodynamo. *Izvestiya Physics of the Solid Earth*, 42:449–459, 2006.
- [59] Binod Sreenivasan and Chris A. Jones. Helicity generation and subcritical behaviour in rapidly rotating dynamos. *J. Fluid Mech.*, 688:5–30, August 2011.
- [60] Binod Sreenivasan and Subhajit Kar. Scale dependence of kinetic helicity and selection of the axial dipole in rapidly rotating dynamos. *Physical Rev. Fluids*, 3(9):093801, 2018.
- [61] F. H Busse. Generation of planetary magnetism by convection. *Physics of Earth and Planetary Interiors*, 12:350–358, September 1976.
- [62] F. H Busse. A model of the geodynamo. *Geophysical Journal International*, 42:437–459, August 1975.

- [63] H. Kitauchi, K. Araki, and S. Kida. Flow structure of thermal convection in a rotating spherical shell. *Nonlinearity*, 10(4):885–904, 1997.
- [64] A. Kageyama, K. Watanabe, and T. Sato. Simulation study of a magnetohydrodynamic dynamo: Convection in a rotating spherical shell. *Physics of Fluids B*, 5:2793–2805, April 1993.
- [65] A. Kageyama and Tetsuya Sato. Generation mechanism of a dipole field by a magnetohydrodynamic dynamo. *Phys. Rev. E*, 55:4617–4626, April 1997.
- [66] Friedrich H. Busse. Convective flows in rapidly rotating spheres and their dynamo action. *Phy. Fluids*, 14:1301—1314, 2002.
- [67] Peter Olson. *Core Dynamics: Treatise on Geophysics*. Elsevier, 2007.
- [68] N. Schaeffer and P. Cardin. Quasi-geostrophic kinematic dynamos at low magnetic Prandtl number. *Earth Planet. Sci. Lett.*, 245:595–604, 2006.
- [69] P. A. Davidson and Avishek Ranjan. Planetary dynamos driven by helical waves - II. *Geophys. J. Int.*, 202(3):1646–1662, September 2015.
- [70] P. A. Davidson and A. Ranjan. On the spatial segregation of helicity by inertial waves in dynamo simulations and planetary cores. *J. Fluid Mech.*, 851:268–287, July 2018.
- [71] Ulrich R. Christensen, Peter L. Olson, and Gary A. Glatzmaier. Numerical modelling of the geodynamo: a systematic parameter study. *Geophys. J. Int.*, 138(2):393–409, January 1999.
- [72] Rakesh K Yadav, Thomas Gastine, and Ulrich R. Christensen. Scaling laws in spherical shell dynamos with free-slip boundaries. *Icarus*, 225:185–193, April 2013.
- [73] Laura K Currie, Adrian J Barker, Yoram Lithwick, and Matthew K Browning. Convection with misaligned gravity and rotation: simulations and rotating mixing length theory. *Monthly Notices of the Royal Astronomical Society*, 493:5233–5256, February 2020.

- [74] Adrian J Barker, Adam M Dempsey, and Yoram Lithwick. Theory and simulations of rotating convection. *The Astrophysical Journal*, 791:13, August 2014.
- [75] Mahendra K. Verma, Roshan Samuel, Soumyadeep Chatterjee, Shashwat Bhattacharya, and Ali Asad. Challenges in Fluid Flow Simulations Using Exascale Computing. *SN Computer Science*, 1:2661–8907, May 2020.
- [76] R Samuel, S Bhattacharya, A Asad, S Chatterjee, M K Verma, R Samtaney, and S F Answer. A general-purpose pde solver for fluid dynamics. *Journal of Open Source Software*, 6:2095, 2021.
- [77] Sebastian Wagner and Olga Shishkina. Aspect-ratio dependency of rayleigh-bénard convection in box-shaped containers. *Phys. Fluids*, 25(8):085110, 2013.
- [78] Shashwat Bhattacharya, Mahendra K. Verma, and Ravi Samtaney. Prandtl number dependence of the small-scale properties in turbulent rayleigh-bénard convection. *Phys. Rev. Fluids*, 6:063501, Jun 2021.
- [79] Emmanuel Dormy and Andrew M. Soward. *Mathematical Aspects of Natural Dynamos*. Chapman & Hall/CRC, Boca Raton, FL, first edition, 2007.
- [80] Mani Chandra and Mahendra K. Verma. Flow Reversals in Turbulent Convection via Vortex Reconstructions. *Phys. Rev. Lett.*, 110(11):114503, March 2013.
- [81] Mani Chandra and Mahendra K. Verma. Dynamics and symmetries of flow reversals in turbulent convection. *Phys. Rev. E*, 83:067303, 2011.
- [82] E Deusebio and E Lindborg. Helicity in the Ekman boundary layer. *J. Fluid Mech.*, 755:654–671, 2014.
- [83] L Duarte, J Wicht, M K Browning, and T Gastine. Helicity inversion in spherical convection as a means for equatorward dynamo wave propagation. *Monthly Notices of the Royal Astronomical Society*, 456(2):1708–1722, 2016.
- [84] W Agoua, B Favier, A Delache, A Briard, and J.T.B. Wouter. Spontaneous generation and reversal of helicity in anisotropic turbulence. *Phys. Rev. E*, 103(6):L061101, 2021.

# Publications

- [0] Abhilash Ojha, Mohammad Anas, Avishek Ranjan, Pranav Joshi, and Mahendra K. Verma, ”Helicity segregation by Ekman pumping in rotating flows with gravity orthogonal to rotation”, **(Under Review)**.